The University of Southern Mississippi
The Aquila Digital Community

Master's Theses

Spring 5-2021

Structural Re-orientation of Magmatic Fabrics and Layering in the Lower Oceanic Crust: Hole GT1, Wadi Tayin Massif, Samail Ophiolite

Justin Guillot

Follow this and additional works at: https://aquila.usm.edu/masters_theses

 Part of the Geology Commons

Recommended Citation

Guillot, Justin, "Structural Re-orientation of Magmatic Fabrics and Layering in the Lower Oceanic Crust: Hole GT1, Wadi Tayin Massif, Samail Ophiolite" (2021). *Master's Theses*. 802.
https://aquila.usm.edu/masters_theses/802

This Masters Thesis is brought to you for free and open access by The Aquila Digital Community. It has been accepted for inclusion in Master's Theses by an authorized administrator of The Aquila Digital Community. For more information, please contact Joshua.Cromwell@usm.edu.

STRUCTURAL RE-ORIENTATION OF MAGMATIC FABRICS AND LAYERING IN THE LOWER OCEANIC CRUST: HOLE GT1, WADI TAYIN MASSIF, SAMAIL OPHIOLITE

by

Justin Guillot

A Thesis
Submitted to the Graduate School,
the College of Arts and Sciences
and the School of Biological, Environmental, and Earth Sciences
at The University of Southern Mississippi
in Partial Fulfillment of the Requirements
for the Degree of Master of Science

Approved by:

Dr. Jeremy Deans, Committee Chair
Dr. Mark Puckett
Dr. Franklin Heitmuller

May 2021

COPYRIGHT BY

Justin Guillot

2021

Published by the Graduate School

ABSTRACT

This thesis aims to re-orient borehole images of layered gabbros sampled beneath Hole GT1 in the Wadi Tayin massif of the Oman ophiolite by the Oman Drilling Project to better constrain models of crustal accretion. The gabbro glacier model proposes that crystallized basalt flows down and away from the crystallization site to form the lower crust while the sheeted sill model proposes that basaltic melt crystallizes at multiple levels in the crust through sills. Hole GT1 provides an unprecedented 400 m, 100% recovery, look at the lower oceanic crust. Cores lose their geographic orientation when drilled, requiring use of the programs like Techlog to match core observations with borehole images oriented relative to north to re-orient the core. Layering is more common throughout the borehole overall but becomes sparse past 250 meters below surface (mbs) whereas magmatic fabrics become more frequent past 300 mbs. Most magmatic fabrics share an average strike of 060 while layering measurements strike close to 355. Both undergo an orientation shift from NE to SW past 300 mbs. The non-systematic distribution of MFs and layering observed below Hole GT1 matches more closely with the sheeted sill model and the idea of melt intruding an upper crystal mush reservoir as a mixing bowl that develops layering and fabrics if enough melt is present for further intrusion. The variance in dip azimuth downhole implies that these features formed through local processes, which supports geochemical evidence that the lower crust forms in an open system through multiple re-intrusions.

ACKNOWLEDGMENTS

I hereby express my deepest gratitude to my Committee Chair Dr. Jeremy Deans for their support, advice, and patience throughout the past few years. It is through the help of their written comments, experience, and sincere words of encouragement that I was able to complete this thesis. I would also like to thank Dr. Franklin Heitmuller and Dr. Mark Puckett for taking the time to be members of my committee in addition to being great teachers who have contributed to my overall growth as a geologist.

TABLE OF CONTENTS

LIST OF TABLES

LIST OF ILLUSTRATIONS

LIST OF ABBREVIATIONS

CRF	Coordinate Reference Frame
Mbs	Meters below surface
SPO	Shape-Preferred Orientation

CHAPTER I - INTRODUCTION

1.1 Purpose

The purpose of this study is to investigate a section of lower oceanic crust beneath the Oman ophiolite and determine the structural orientation of magmatic fabrics and layering. This can be done by using core data analysis to identify the directional orientation of gabbro samples retrieved beneath the Wadi Tayin massif of the Oman ophiolite. These samples were cored from three borehole well sites designated GT1, GT2, and GT3 (Koepke et al., 2015). The focus of this study will be Hole GT1, where the deepest core was extracted from layered gabbros above the mantle. Downhole logging of the GT1 borehole took place during the OmanDP drilling project in two open-hole operations between 2017 and 2018 (Kelemen et al., 2020).

Rapid spreading mid-ocean ridges such as the East Pacific Rise create the majority of new oceanic crust on Earth (Fowler, 2012; Morgan and Chen, 1993) and are useful for understanding interactions between lower oceanic crust and the mantle. However, oceanic crust generated from fast-spreading ridges is difficult to observe in situ and link together structures and processes because it often occurs under complex magmatic conditions at extreme depths. Ophiolites are thus useful for observing sections of oceanic crust as they are obducted and exposed on the surface. Yet on the other hand, ophiolites may not always present an unaltered and accurate representation of the lower crust as they are thought to form in supra-subduction zones and have been overprinted by obduction (Cox and Searle, 1999; Tominaga, 2013). This further complicates efforts to make accurate observations on the lower crust and promotes the need for samples that are as undisturbed and extensive as possible. Because key geological features can be

obscured by frequent overprinting and alteration in ophiolites, exposures that are large, intact, and consistent are necessary for studying the lower crust despite their rarity. The Oman ophiolite satisfies these criteria as it is one of the largest known and complete segments of exposed basaltic crust and mantle (Ben and Allard, 1989; Pallister and Hopson, 1981). The southern massifs of the Oman ophiolite are especially favorable for observing the oceanic crust because they have an intrusive contact to the underlying Moho transition zone and mantle along with having recognized paleo-spreading centers (Amri et al., 1996). The central and northern stretches of the Oman ophiolite contrast this by containing steeply dipping segments of the Moho that rarely align with the overriding crust. The evenly stacked crustal sections beneath the Wadi Tayin and southern massifs allow for the extracted core to contain the lower crust and mantle transition zone parallel to one another, providing a vertical view of all strata present with less obduction-related displacement between the ophiolite sections.

The general purpose of a downhole log is to describe the physical and chemical properties of strata by taking measurements within short intervals of depth that repeat throughout the formation in question. The information detailed in these logs can be an effective supplement to core data, even if a majority of the core was not recovered successfully during drilling (Kelemen et al., 2020). Since the core recovery of Hole GT1 is nearly 100%, the log, namely borehole imagers like the Optical Borehole Imager, and core data, namely fractures and veins that are more easily correlated between core and borehole images, are a close enough match for the structural orientation of the core to be calculated with as little error as possible. Identifying magmatic fabric orientation for this

section of oceanic crust can yield structural data for the Oman ophiolite that may be used to help assess how the lower oceanic crust is formed.

It is clear that determining the orientation of magmatic fabrics and layering is imperative to placing constraints and testing models of lower crustal accretion as they provide details on the timing of deformational processes and magmatic flow direction within a magma chamber during crustal accretion. Magmatic fabrics can be imprinted inside a magma chamber through a wide range of processes that including flow panes, in situ expansion, thermal convection, mechanical flow, and regional deformation (Paterson et al., 1998), making these fabrics an effective record for different features of a magma chamber at the cost of being difficult to interpret. Furthermore, magmatic fabrics and layering often track multiple processes in the lower crust simultaneously and may derive from different structural features or styles of accretion. For example, a single pluton may house multiple magmatic fabrics that are aligned sub-parallel with respect to one another as a result of vertical compaction caused by regional deformation (i.e., extension) while another set of fabrics are instead oriented parallel to flow planes within the melt lens (Van Tongeren and Kelemen, 2015; Paterson et al, 1998). Therefore, structural observations and the orientation of microstructures must be carefully assessed when applied to models of crustal accretion (Paterson et al., 1998). The methods of this study include the use of logging software combined with optical borehole images of Hole GT1 to ensure that all MF and layering features are precisely identified and reoriented with respect to true geographic north.

The models that are typically invoked to describe how the lower crust forms are called the sheeted sills, gabbro glacier, and hybrid models (Boudier et al., 1996; Kelemen

et al., 1997; Morgan and Chen, 1993; Ben and Allard, 1989 VanTogeren et al., 2015). The sheeted sills and gabbro glacier models differ primarily on the site of crystallization of basaltic magma and the degree of kinematic strain involved in forming crustal fabrics from a magma chamber while the hybrid model combines elements from both. These models were not developed with structural data but may be tested with structural arguments.

1.1.1 Geological Background

The original Penrose Field Conference of 1972 defined the structure of ophiolites as upper mantle peridotites at the bottom followed by layered ultramafic and mafic rocks, foliated and layered to isotropic gabbros, sheeted dikes, extrusive rocks, and then a sedimentary cover at the top (Anonymous, 1972; Dilek and Furnes, 2014). The second Penrose conference assessed this definition and found it to still be effective in comparing ophiolites to oceanic crust while also reaffirming that the definition needs to be expanded in regard to individual complexes in the crust stratigraphy, for example, crust formed at slow-spreading ridges (Dilek et al., 2000). The mafic and ultramafic rocks listed here also make up a crust-mantle transition that underlies the layered gabbros.

Current models for oceanic crust stratigraphy are based on findings from the second Penrose Field Conference held in 1998 (Dilek et al., 2000) to discuss oceanic spreading dynamics and the role of ophiolites in crustal generation. One major focus was examining how crust could be generated at a mid-ocean ridge and then rise up to the surface as an ophiolite. Although ophiolites had been previously acknowledged for exposing segments of lower crust that matched with structural data found in mid-ocean ridges, newly acquired geochemical data from ophiolites implied that some ophiolites

formed as part of subduction zones (Dilek et al., 2000). The potential for ophiolites to form in environments other than mid-ocean ridges opened up discussion for how oceanic crust is preserved in different geological settings. Considering that layered gabbros have never been drilled in situ, this study treated the lower crust exposed in the Oman ophiolite as a direct analogue for the lower oceanic crust.

Current understanding of how lower oceanic crust forms has changed in recent decades as several different models have been proposed (Figure 1.1). The sheeted sills model predicts that the lower crust is generated from melts that intrude at all levels of the lower crust (Amri et al., 1996; Boudier et al., 1996; Kelemen et al., 1997; Korenaga and Kelemen, 1997; Henstock et al, 1993). According to this model, local basaltic melt is carried upwards to a site of emplacement and undergoes in situ crystallization. This encourages modal layering to form in the fabric as compositional variations between segregated crystals of plagioclase, clinopyroxene, and olivine (Korenaga and Kelemen, 1998).

The gabbro glacier model was proposed in response to seismic analyses of the lower crust demonstrating that magma chambers lack a “big tank” and instead have a 100 m thick melt lens right below the sheeted dike complex (Dunn et al., 2000). New models based on thermal modeling to remove the latent heat of crystallization of basalt in the melt lens were proposed to match the seismic observations. This model suggests that basalt crystallizes only at the sheeted dike-gabbro transition before flowing down and away in a solid to semi-solid state generating the lower crust (Quick and Denlinger, 1993; MacLeod and Yaouancq, 2000; Morgan and Chen, 1993; Ben and Allard, 1989). The sinking motion of the mush (melt and crystals) into the layered gabbros below would

produce high levels of shear strain (VanTongeren and Kelemen, 2015), resulting in both lateral and vertical deformation as well as fabric rotation above the Moho boundary.

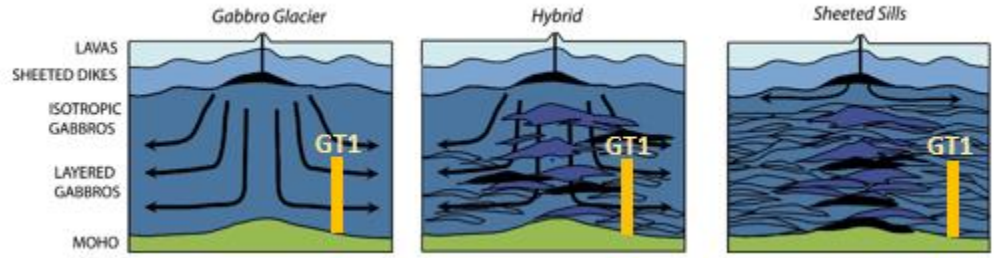

Figure 1.1 . *Illustration of models for crustal accretion at fast spreading mid-ocean ridges.*

Modified after VanTongeren and Kelemen (2015).

The magmatic origin of the Oman ophiolite may closely follow one of these models or instead possess characteristics from both in the form of a hybrid model (Boudier et al., 1996; VanTongeren et al., 2015). In this model, the upper foliated gabbros formed through the sinking processes described by the gabbro glacier model whereas the layered gabbros formed by sill intrusions in a process similar to the sheeted sills model.

1.1.2 Oman Ophiolite.

The Oman or Samail ophiolite stretches over 600 km across the northern Arabic Peninsula and originally belonged to the Neothethys seafloor during the Cretaceous at 95 to 100 Ma (Nicolas and Boudier, 1995; Gray and Gregory, 2000; Rioux et al., 2016). The Oman ophiolite comprises the most extensive, best exposed, and continuous segment of oceanic crust from seafloor sediments to the mantle. Incorporation of the ophiolite into the Arabic Peninsula took place by 94 Ma through an obduction event that caused the oceanic crust present in the ophiolites to tilt and become tectonically fragmented into

several massifs that comprise 8-12 km of upper mantle peridotites and 4-7 km of oceanic crustal rocks (Cox and Seale, 1999). The dominant rock types are gabbros, peridotites, and dunites that include lesser lenses of wehrlite and clinopyroxenite (Nicolas and Boudier, 2000). One of the most prominent folding structures in the south Oman ophiolite is the Ibra Valley syncline, which acts as a window of exposed rocks from the Hawasina Complex (Gray and Gregory, 2000; Nicolas and Boudier, 2000). Located just above Ibra Valley syncline is the Wadi Tayin massif, which is proximal to multiple fault zones that intersect a series of layered gabbros belonging to the lower crust alongside alternating bands of graded metagabbros, anorthosites, and wehrlites (Boudier et al., 1996).

1.1.3 Wadi Tayin.

The cores extracted samples of foliated gabbros from the upper crust and layered gabbros from the lower crust of the Wadi Tayin (Figure 1.2). On the surface, primary igneous textures are apparent in the layered gabbros amid transitions to multi-textured, foliated gabbros the closer they are to the center of fault zones, where greenschist facies metamorphism persists along with a deep hydrothermal network of fractures and veins (France et al., 2009; Koepke et al., 2015). Core samples up to 400 meters in length were retrieved from three drilling sites located at the Wadi Gideah in the southward secion of Wadi tayin (Koepke et al., 2015). The sites represented the lower crust, middle crust, and upper crust of the Oman and were each named GT1, GT2, and GT3 respectively.

The upper crust attributed to GT3 contains sheeted dikes and basaltic structures similar to sills that gradually transition into multi-textured and eventually foliated gabbros at increasing structural depths. The dikes have a diabase composition and reside

within hornfels-type metamorphism, whereas the gabbros include poikilitic clinopyroxenes with phenocrysts of plagioclase feldspar (Kelemen et al., 1997).

This variety in texture becomes increasingly uniform in the middle crust below, where foliated gabbros from site GT2 appear approximately 2656 meters above the Moho zone (Koepke et al., 2015, Henstock et al., 1993; Boudier et al., 1985).

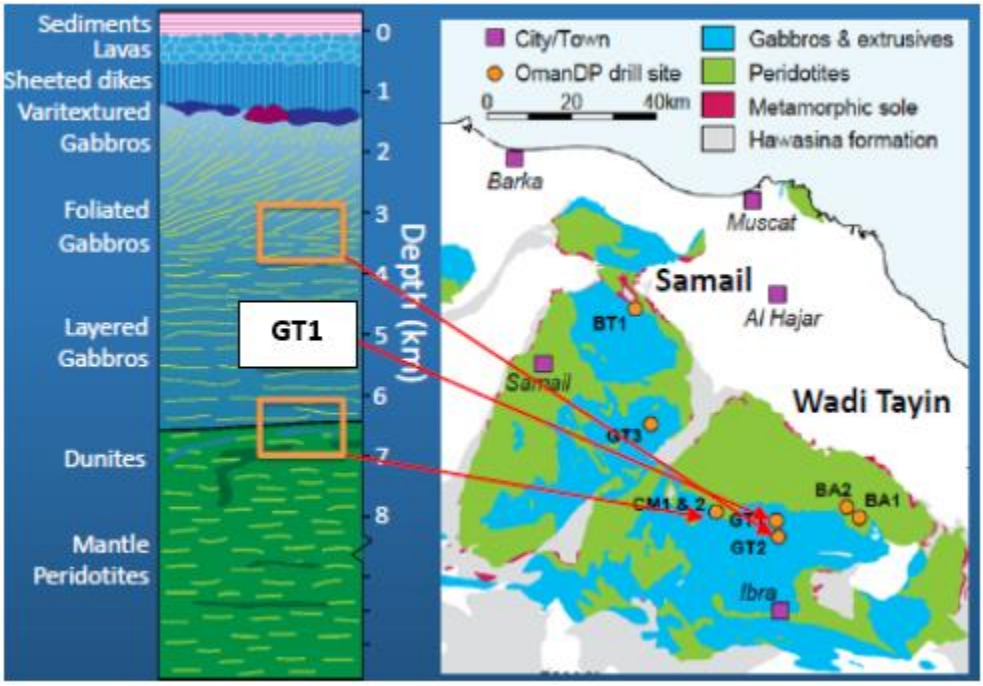

Figure 1.2 *Geological and structural map from the Wadi Tayin massif of the Oman Ophiolite*

The focus of this study is the layered gabbro section and Hole GT1, featured below the upper foliated grabbros (France et al., 2009)

The middle crustal section marks a distinct change from primarily fine grained isotropic gabbros and diorites to the coarser grained layered gabbros drilled in GT1. This transition becomes more apparent in the foliated gabbro fabric due to the loss of poikilitic orthopyroxenes and internally crystallized pargasites, both of which are either diminished or absent in the layered gabbros (France et al, 2009). The foliated upper gabbros have

steeper dips up to 60° to the south and southwest (Kelemen, et al., 1996; Nicolas et al., 2000) and exhibit no modal layering until reaching the lower gabbros closer to the Moho transitional zone and mantle below (Kelemen et al, 1996; Koepke et al., 2015).

The lowermost crust present in GT1 is the primary focus of this study and includes a sequence of layered gabbros located 1079 meters above the mantle. The lower crust of the Wadi Gideah exhibits fabrics and textures of melt interaction that differ from the foliated gabbros and dike systems in the middle and upper crust (Koepke et al., 2015). The cores extracted from the GT1 site intersect several fault zones that intrude sections of the lower crust, displacing the layered gabbros between the middle and upper crust fabrics. The current orientation has an average dip of 28° with occasional variations between the parallel layers and intruding sill structures. Deep within the Moho transition zone, the layered gabbros retain a mafic to ultramafic composition until bands of hazburgites, dunites, and peridotites from the mantle become dominant.

The metamorphic sole beneath the Wadi Tayin has an average thickness of 230 meters and contains isocline-folded layers of amphibolite, greenshist, clinopyroxene and hornblende-plagioclase gneiss, and quartzites (Gray and Gregory, 2000, Nicolas et al, 2000; Boudier et al, 1985) that have northeast trending lineations along the fold axis. The amphibolite sequence begins below the 150m thick greenshist facies, where contacts between amphibolite and peridotite sequences are accompanied by parallel lineations (Gray and Gregory, 2000). These lineations within the metamorphic sole follow the isoclinal fold axis, shifting from a north to northeast direction along the Wadi Tayin while being offset by east to west oriented normal faults.

–METHODS

1.1 Materials and Methods

An Optical Borehole Imager (OBITM40 GR) recorded images from Hole GT1 of the Wadi Tayin massif prior to this study. Developed by the Advanced Logic Technology Company, this imager was designed to specialize in both open and cased hole analysis while providing oriented structural information, fracture detection and evaluation, lithology and mineralogy characterization, and thin bed detection in addition to bedding dip. The OBI specifications include a diameter of 40 mm (1.6"), min/max length of 1.49/1.93 m, min/max weight of 11.7/16.6 lbs, max temperature of 70^{o}C (158^{o}F), and max pressure of 200 bars (2900 PSI). It comes equipped with high efficiency LED lights and a 1/3" high sensitivity CMOS digital image sensor with a 24 bit RGB color resolution, 5.48V/lux-second responsivity, and azimuthal resolutions at 120, 180, 360, 600, 900, and 1800 points. The vertical resolution is user defined in addition to being a function of depth encoding while the deviation sensor included an APS544-3 axis magnetometer – 3 axis accelerometer while the natural gamma sensor integrated an OBI40 GR 0.875" X 3 Nal (Ti) scintillation crystal. The 3-axis magnetometer allows for both the tool and borehole image to be oriented relative to true geographic north. The OBITM40 GR operating conditions consisted of Mono, coax, and multi-conductor cable types, a measurement range of up to 21", required centralisation, variable baud rate telemetry, and dry, clear water-filled borehole fluid. Other systems compatible with the OBITM40 GR include ALTlogger, Bbox, Matrix, OPAL, and SCOUT. The logging speed was a function of both image resolution and wireline electrical properties at 6m/minute with 900 pixels azimuthal resolution and a 2mm vertical sampling rate at 100

Kbps. For this study, an average caliper value was used in place of a caliper log because the 3-armed caliper tool utilized in Hole GT1 proved less effective in an asymmetric borehole (Kelemen et al., 2020). This resulted in some dips being over or underestimated where the borehole was smaller or larger than the average borehole diameter. Core descriptions were made by separating each core section into units based on the different rock types recorded by shipboard scientists (Kelemen et al., 2020). All magmatic fabrics and layering were identified and measured in the core reference frame by shipboard scientists (Kelemen et al., 2020) and used in this study. All observations and measurements for each section-unit were recorded in excel worksheets that could be readily compared with core and borehole images using logging software such as Techlog by Schlumberger.

Although the core had been collected from Hole GT1 with 100% recovery, individual pieces were free to break up and rotate during the extraction process. This resulted in the core images losing their original orientation relative to true north, making it necessary to digitally restore the dip and dip direction of each core piece by utilizing the Techlog program developed by Schlumberger. Prior to this study, Schlumberger processed the necessary files for use in Techlog since the logs were not able to be directly imported due to being in a proprietary file format from Advanced Logic Technology Company. Images acquired by the OBITM40 GR were uploaded into Techlog.

Depth and dip measurements from the shipboard core data were used to locate the same features in the borehole. All visible features then had to be rotated until both images matched one another as precisely as possible. By comparing dip angle measurements between the borehole and core images in this way, an angle of rotation was computed and

then applied to each core to rotate other structures in the core, for example, magmatic fabrics, back to their pre-drilled orientation.

A new project was created in Techlog and files containing the borehole imagery dataset were imported by navigating to the Home and then Import tab. XML, TIFF, and RGB files within the Oman data folder were then highlighted before core image variables including Top Depth, Bottom Depth, and Well Name were selected using the image import wizard. The selection of different parameters from the data allowed for specific details such as the top depth and bottom depth for the log or core section to be identified by Techlog. Meters were selected as the unit for expressing borehole depth. Upon selecting all necessary variables and checking in the Parameter Detection and Apply To All options, the GT1 data files were dragged and added to the Logview display area. Brittle features that are most apparent in the borehole image, like veins and fractures, are identified and drawn over. Techlog then calculates the dip azimuth of the sinusoid shape by correlating the image position with the direction of the lowest point on the sinusoid. Techlog calculates the dip by taking the borehole diameter and the depth interval of the sinusoid.

Upon displaying the Hole GT1 borehole images in Techlog, the vein log and MF log spreadsheets from OmanDP Phase 1 were opened in Microsoft Excel. These spreadsheets were used to locate notable features down the borehole by cycling back and forth between the borehole image in Techlog and the vein log and MF sheets in Excel. When a notable feature was identified in the borehole image, the corresponding depth of that feature was matched to an azimuth and dip angle in the vein log sheet. The vein log provided the dip azimuth value in the core reference frame while the MF log provided a

dip azimuth, also in the coordinate reference frame (CRF). Subtracting the measured dip azimuth in the CRF from the dip azimuth determined in the oriented borehole image yielded a rotation angle. This angle was then added to the measured dip azimuth in the CRF of other features in the core like magmatic fabrics and layering, to find the re-oriented dip azimuth. This process repeated for each feature identified in the borehole image and the results were entered into a separate data sheet that provided the re-oriented azimuth, dip, and depth values needed to construct depth plots and stereonets. In all, 395 veins, and therefore core pieces, were re-oriented in Hole GT1.

A level of confidence was given to each orientation based on accuracy, with 5 being the highest level of confidence and 1 describing the more uncertain measurements that did not match either the same depth or orientation angle recorded in the vein log spreadsheets. Additionally, features had to be identified in both the core and borehole images with no more than 5 m of difference in depth so as to mitigate potential error. For cases in which a common feature was identified but the borehole image depth greatly exceeded or fell below the depth recorded in the core image, a lower level of confidence was assigned to the calculated rotation angle. Depth differences are not uncommon and are typically due to differences in drilling depth, logging depth, and curated depth. The dip magnitude also has to be within 5° to be considered the same in the borehole image and measured on the core. However, due to the use of an average borehole diameter, the 5° standard was not always met. In this case, patterns of a single, or typically multiple veins, was used to match between the core image and the borehole image (Figure 2.1).

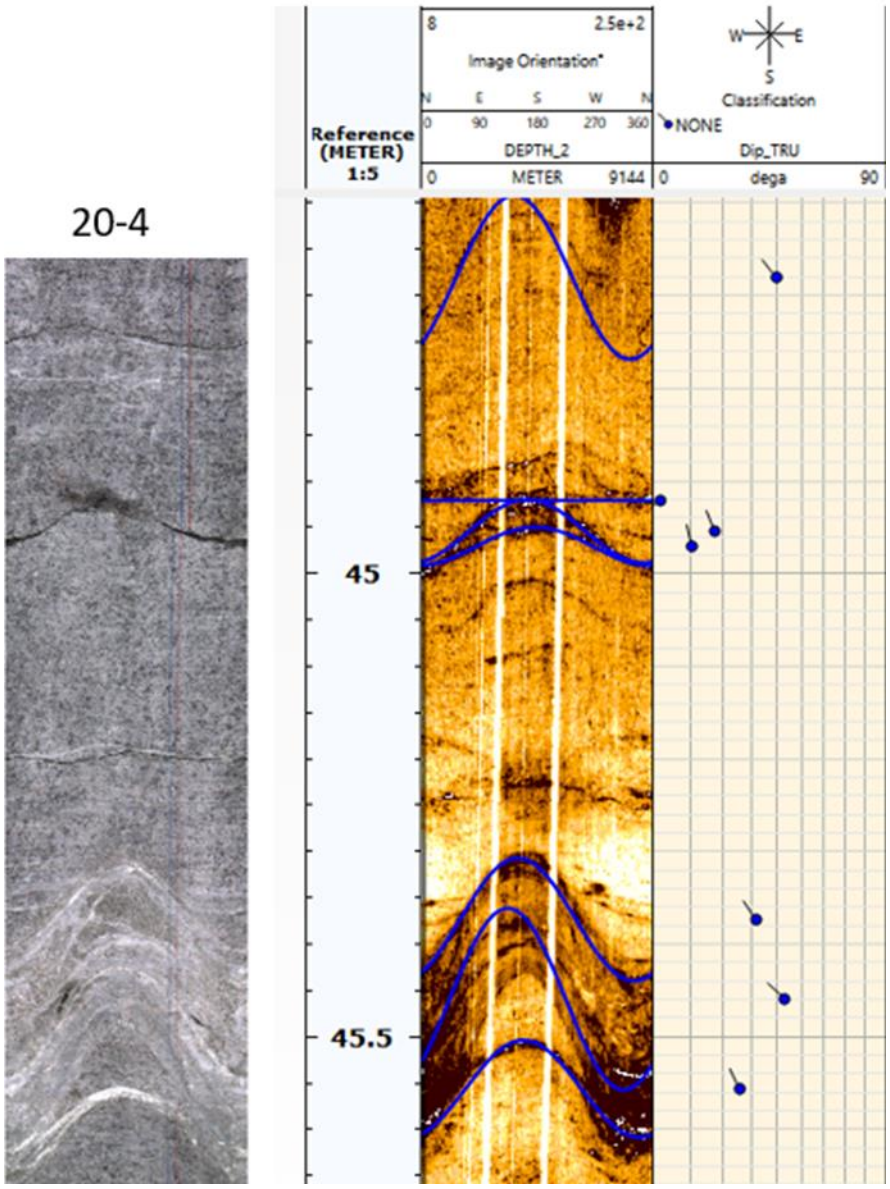

Figure 1.1 *Example comparison between a shipboard core image (unrolled whole core; left) and borehole image in Techlog (right).*

Both display the same layering features observed from core section 20-4 located 45.6 mbs in Hole GT1. The images are at slightly different scales, so the amplitudes and therefore the dips, look different

The reoriented dip and dip azimuth values were sorted by depth and entered into the Allmendinger program Stereonet (Allmendinger et al., 2012) to produce a series of stereonet plots. These plots differed based on the type of value used. For example, a plot

was made by inputting only the measurements with a confidence level of 5 while other plots would exclusively include measurements for layering or magmatic fabric measurements. A plot including every reoriented dip and azimuth measurement recorded in this study was made as well. Separating the data in this way allowed for the overall direction of structures within Hole GT1 to be viewed individually and compared in an orderly manner.

Depth plots accompanied each stereonet and visually expressed the distribution of orientation data versus depth as a series of scatter diagrams. Each plot derived from the dip and reoriented dip azimuth data that were picked and calculated in Techlog. The reoriented dip and dip azimuth values from each sheet corresponded to the x-axis while the depth column corresponded to the y-axis. This created a cross sectional view of data points representing the new orientation angle of structures according to their position along the borehole. These cross-sectional depth plots were required to detect structural patterns within several intervals of depth in Hole GT1 and then compare those patterns with plot patterns commonly used to describe the Gabbro Glacier, Sheeted Sill, and Hybrid models of lower crust formation. To this end, several new depth plots labeled as pattern plots were made in a new spreadsheet.

– RESULTS

Magmatic fabrics were defined by the intensity and occurrence of shape-preferred orientation (SPO) within magmatic phases whereas layering was defined as variations in mineral proportions and assemblages combined with variations grain size (Kelemen et al., 2020). Both types of features were identified from the borehole images in Techlog. This yielded 395 measurements in total, 183 of which were magmatic fabrics and 213 of which were layering intervals. This equates to one magmatic fabric every ~2 m and a layer every ~0.5 m.

2.1 Depth Plots and Histograms

Figure 3.1 displays the orientations of all magmatic fabrics in the geographic reference frame from Hole GT1. Beginning from the top of the hole at 30 mbs, the data points representing the magmatic fabric measurements initially show a pattern that of dip azimuths oriented NE between 45^{o} and 90^{o}. The data points situated between 0 and 100mbs are spaced closely together as the majority of measurements share a similar range in dip azimuth around 80^{o} with relatively little deviation. Past 100 mbs, most measurements begin to dip towards the south before retaining a SW orientation with dip azimuth values above 200^{o}. This pattern only lasts until 160 meters in depth, where the measurements shift away from 200^{o}. The data points then become more varied than previously with the introduction of more NE and NW oriented dip azimuths that range below 135^{o} and above 225^{o}. Between 220 and 250 mbs, the data points cluster together near the center of the plot and share a SE dip azimuth orientation just below 180^{o}. The pattern ends by 300 mbs, however, where the frequency of magmatic fabrics declines. A new pattern emerges past 320 mbs as north-oriented dip azimuths become more frequent

with little deviation present. Dip azimuths below 090^{o} and above 300^{o} begin to gradually shift towards the south, falling closer to 180^{o} as depth increases. Each new measurement is evenly spaced from the last during this south-bound trend, forming a “v”-shaped pattern of data points that converges near the middle of the graph by 360 mbs. Northwest-oriented data points are present around the same depth with dip azimuths between 309^{o} and 345^{o}. The final magmatic fabric data points transition back to a northeast/southeast pattern as measurements below 390 mbs fall between 060^{o} and 150^{o}.

The general distribution and frequency of magmatic fabrics can be observed in the following histogram (Figure 3.2). Similar to the azimuth vs. depth plot, magmatic fabrics are initially very rare above 50mbs before beginning to densely populate Hole GT1 by 150 mbs. Magmatic fabrics continue to densely populate the data set until they become relatively sparser below 300 mbs. A significant boost in the frequency of magmatic fabrics then occurs in the 400 mbs depth bin. This sudden boost is then followed by an even quicker decline however, as the frequency of magmatic fabrics drops to its lowest value by 450 mbs.

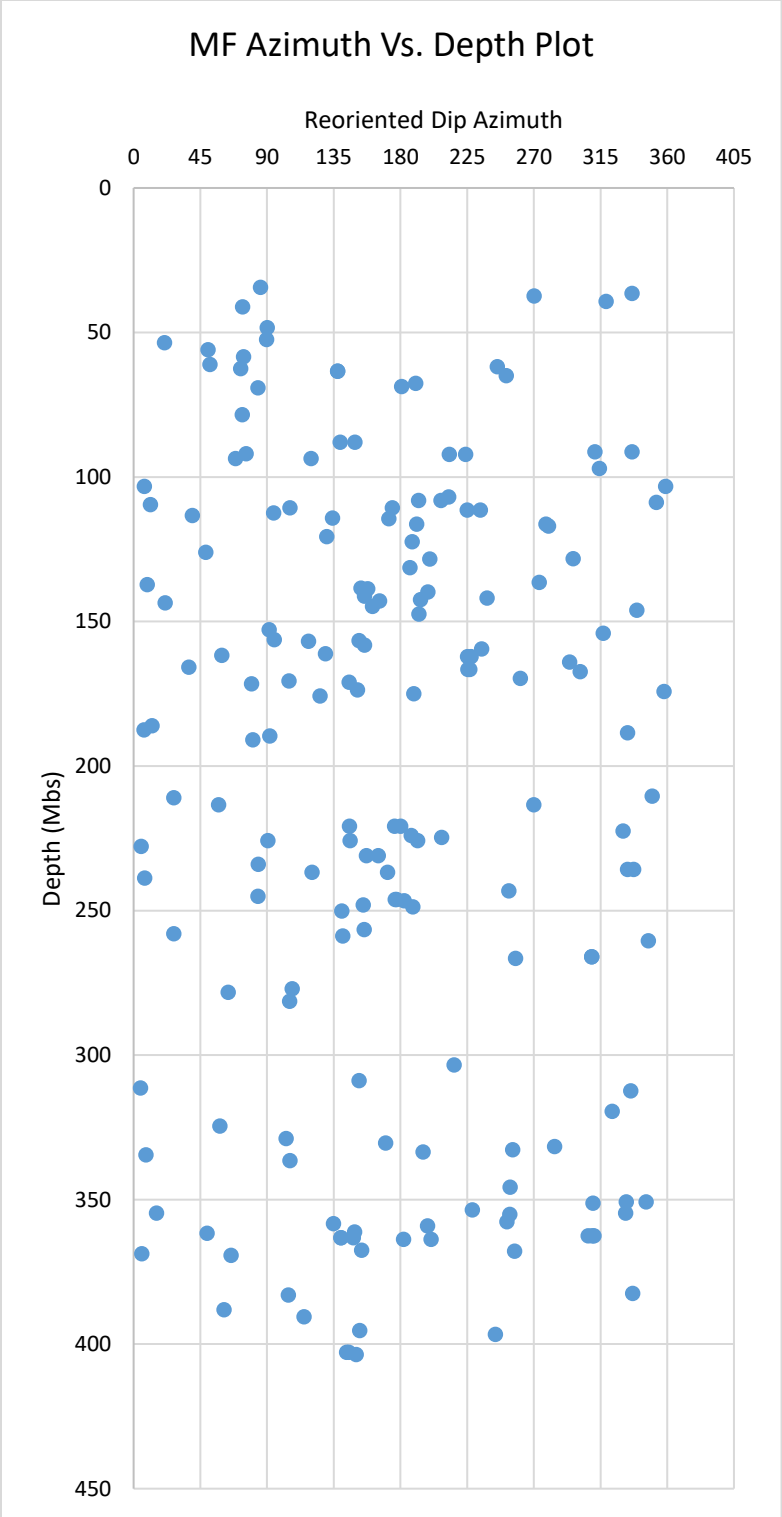

Figure 2.1 *Reoriented Dip Azimuth vs. depth plot for all magmatic fabrics observed in this study.*

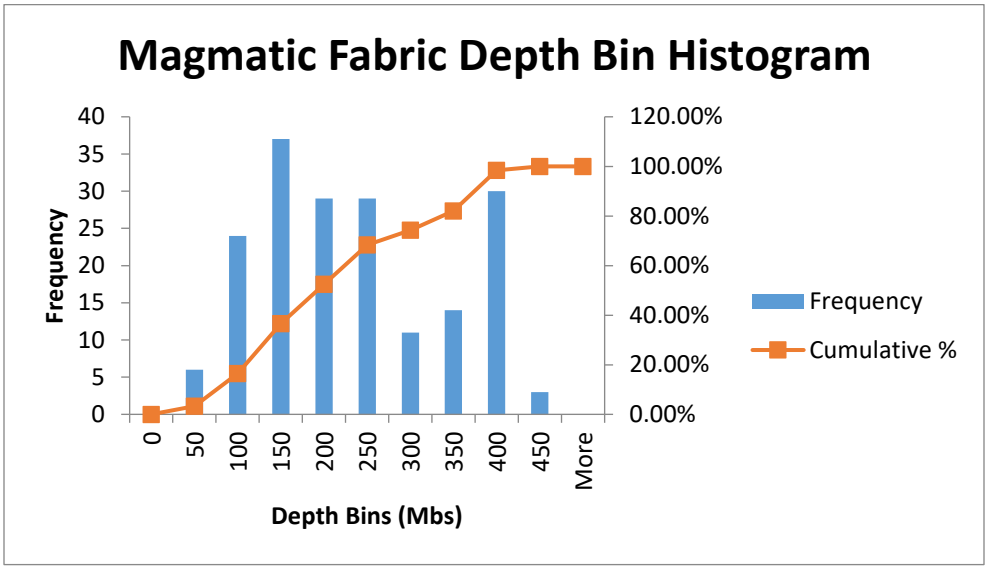

Figure 2.2 *Histogram depicting frequency and cumulative percentages for all magmatic fabrics identified in this study.*

2.1.2 Dip Azimuth vs. Depth Plot: Layering

Figure 3.3 displays a depth plot that includes the orientations of features attributed to layering exclusively. Most layering features initially have dip azimuths oriented NE and SW at 55^{o} and past 180^{o} a relatively wide range in dip azimuth values. A pattern emerges below 40 mbs in which dip azimuths shift from 13^{o} to over 100^{o} at 60 mbs and then shift back closer to 45^{o} between 65 mbs and 95 mbs. The data points become less varied past 100 mbs, where the majority of dip azimuths are oriented SW at 207^{o}.

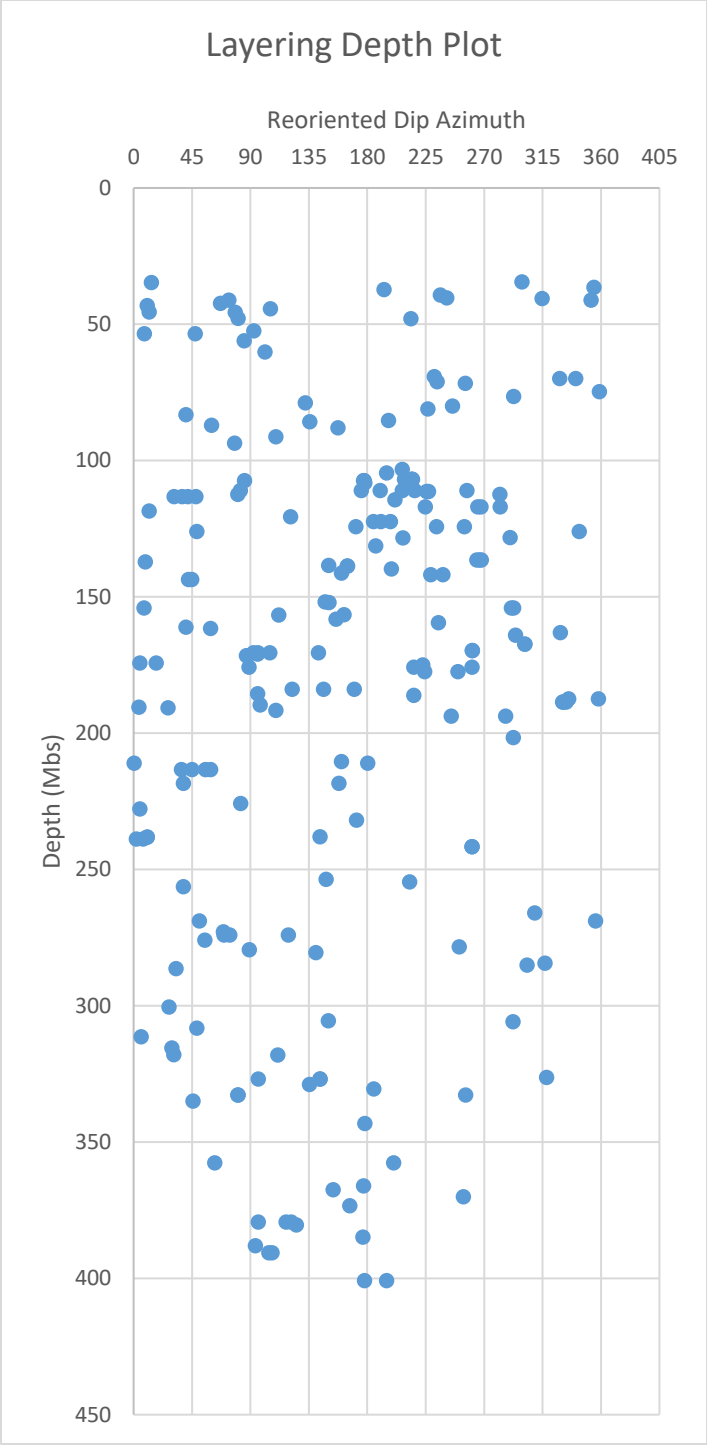

Figure 2.3 *Reoriented Dip Azimuth vs. Depth Plot for all layering structures observed in this study.*

The overall variance in orientation between points increases significantly by 150 mbs. Many layering measurements have SE and NW oriented dip azimuths and before becoming slightly less frequent. The number of layering measurements increases again shortly thereafter at 260 mbs where dip azimuths less than 90^{o} and greater than 300^{o} occur with an E and NW orientation respectively. Measurements past 300 mbs gradually transition from a SE to SW as dip azimuth values rise above 90^{o} up to 190^{o} near 400mbs.

A histogram illustrating the frequency of layering throughout ranges of depth below Hole GT1 (Figure 3.4) provides a more detailed view of where layering is absent to most prevalent. The highest number of layering structures occur near 150mbs before sharply declining past 200 mbs. A slight resurgence in layering frequency occurs by 400 mbs but this quickly changes following a significant decline that continues past 450 mbs.

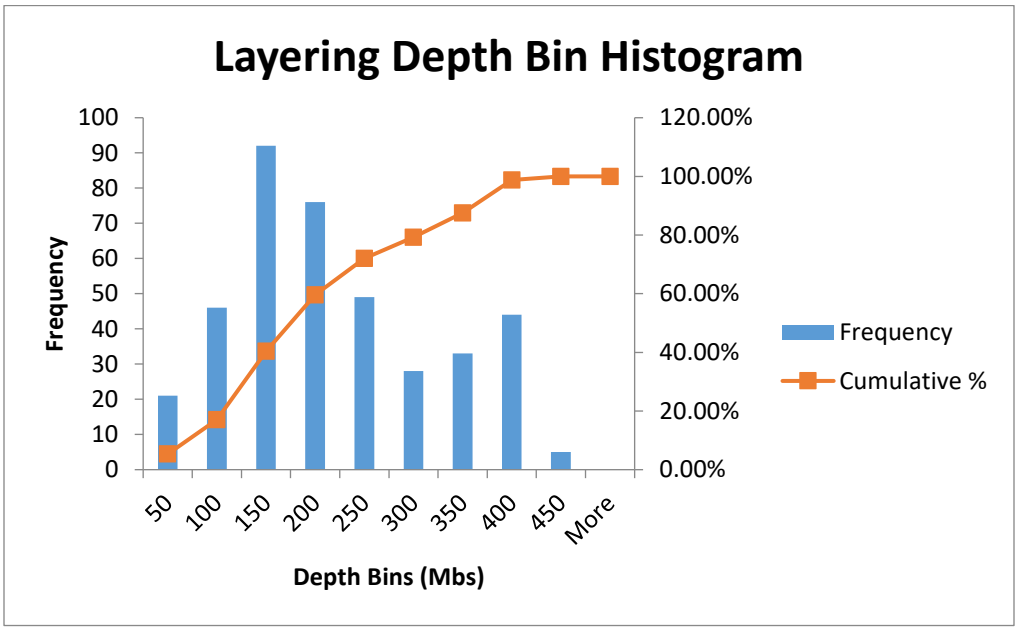

Figure 2.4 *Histogram displaying frequency and cumulative percentages of all instances of layering observed in Hole GT1.*

2.1.3 Dip Azimuth vs. Depth Plot: All Data

Figure 3.5 displays the reoriented dip azimuth for all magmatic fabric and layering features. The first significant pattern appears near 48 mbs, where the majority of data points share a north to northeast orientation with dip azimuth measurements between 000^{o} and 090^{o}. Several points deviate from this pattern by dipping more to the south and southeast, although with less frequency and precision than the north-oriented clusters.

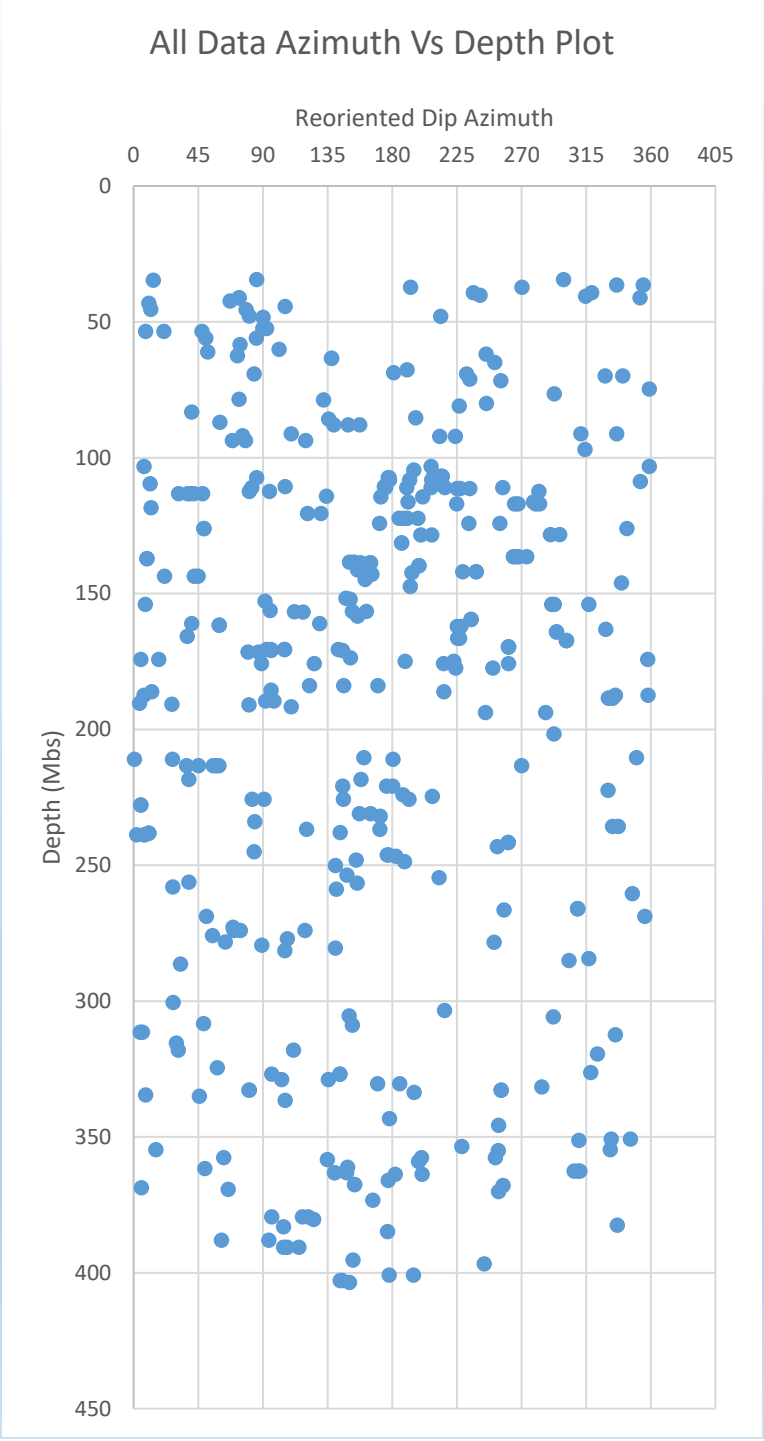

Figure 2.5 *Reoriented Dip Azimuth vs. Depth plot for all structures observed in this study.*

Magmatic fabrics and moderate-intensity layering became more prevalent further down the borehole image as a transition in dip direction took place by 76 mbs. The dip direction of structural features then changes towards the south with slightly more variety in angle between each data point. At 103 mbs, the majority of measurements range from dip azimuths of 162^{o} to 267^{o} as the data points concentrate towards the center of the histogram (Figure 3.6). The most north-oriented measurements begin to follow this pattern by dipping gradually towards the Southwest at 200^{o}, appearing on the graph as a "v-shaped" array of dots that ends near 140 mbs in depth. The frequency of dip and dip azimuth measurements then rises sharply with little deviation until the pattern starts to shift back towards north just below 150 mbs, completing a cycle that repeats intermittently throughout several sections of the borehole. A more north-associated trend persists for the next couple hundred mbs as the data points dip more steeply.

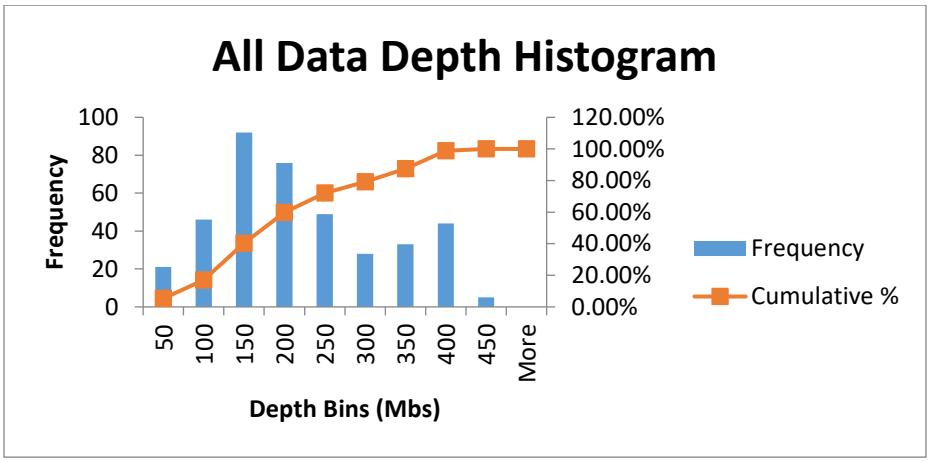

Figure 2.6 *Histogram displaying frequency and cumulative percentage for all data points observed in this study.*

2.1.4 Dip Azimuth Vs. Depth Plot: High Confidence

The azimuth versus depth plot for measurements with the highest confidence values in the data set (Figure 3.7) shares many patterns in common with the previous plots while having slightly less SW oriented dip azimuth values at 200^{o}. This is most apparent within the first 30 to 60 mbs of depth where most dip azimuth measurements share a NE and NW direction that coincides more closely with the magmatic fabrics depth plot. Past 105 mbs, however, dip azimuth values between 150^{o} and 270^{o} occur more frequently in a similar manner to the depth plots for layering and all data.

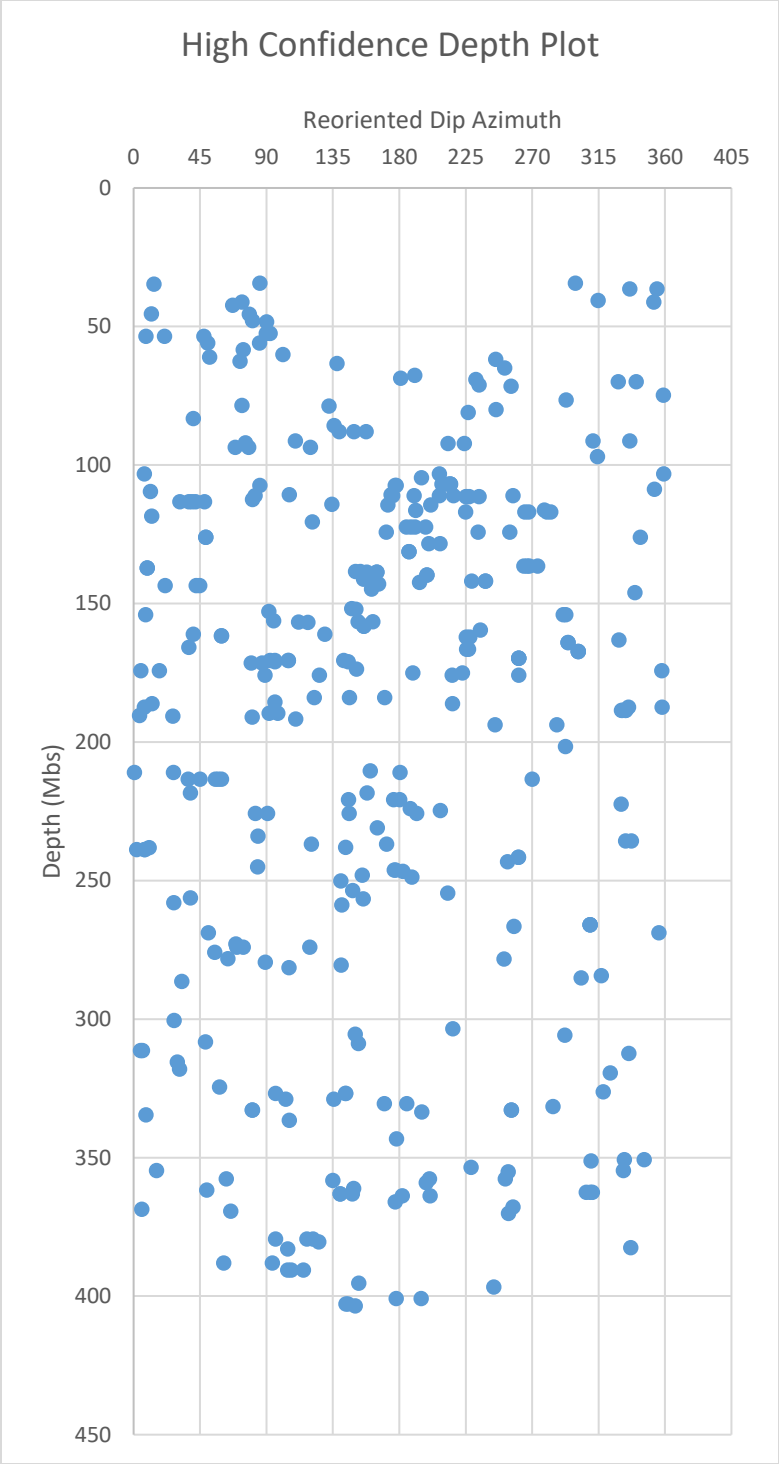

Figure 2.7 *Reoriented dip azimuth vs. depth plot for all measurements that have a confidence value of 4 or 5.*

The depth bin histogram for all high confidence dip azimuth measurements (Figure 3.8) shows a lower amount of dip azimuth measurements found in the 50 mbs and 250 mbs depth bins compared to the histogram for all data. The dominance of values in the 150 mbs depth bin is still present and the order of abundance between depth bins remains mostly unchanged.

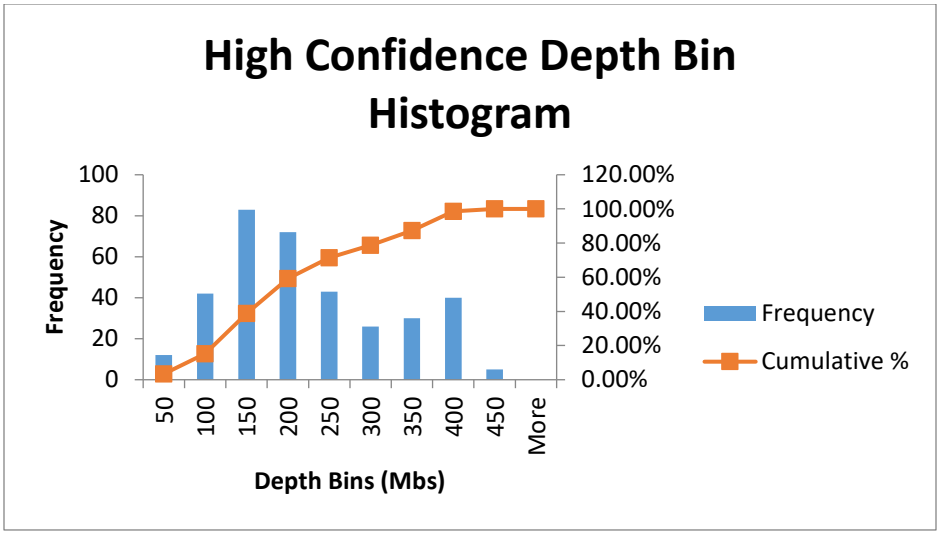

Figure 2.8 *Histogram displaying frequency and cumulative percentage for data points observed in this study that have a confidence value of 4 or 5.*

2.2 Stereonets

2.2.1 Stereonet: Magmatic Fabrics

The dip and dip direction of all magmatic fabrics identified in the GT1 OBI were used to construct a stereonet plot and respective Rose diagram (Figure 3.9). Most MF measurements share an ENE-WSW strike orientation while several less pronounced patterns of strike vary in direction between WNW to ESE. These patterns are also apparent when plotted as poles to planes and complimented with contouring (Figure 3.10) as the majority of poles found in the center of the contour area represent sub-horizontal MFs with the exception of smaller populations on the outer contours that deviate and become increasingly steep as their distance from the center increases.

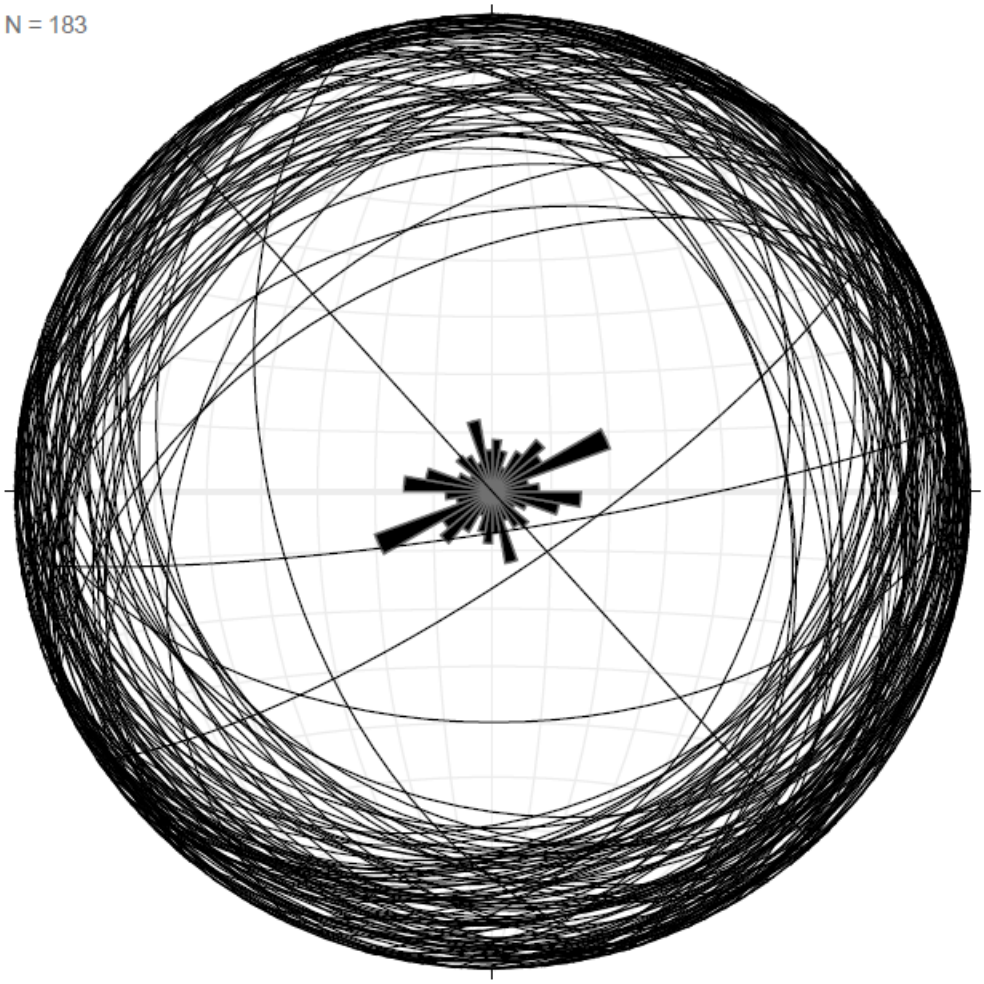

Figure 2.9 *Stereonet of magmatic fabrics displayed as planes alongside a Rose Diagram in the center.*

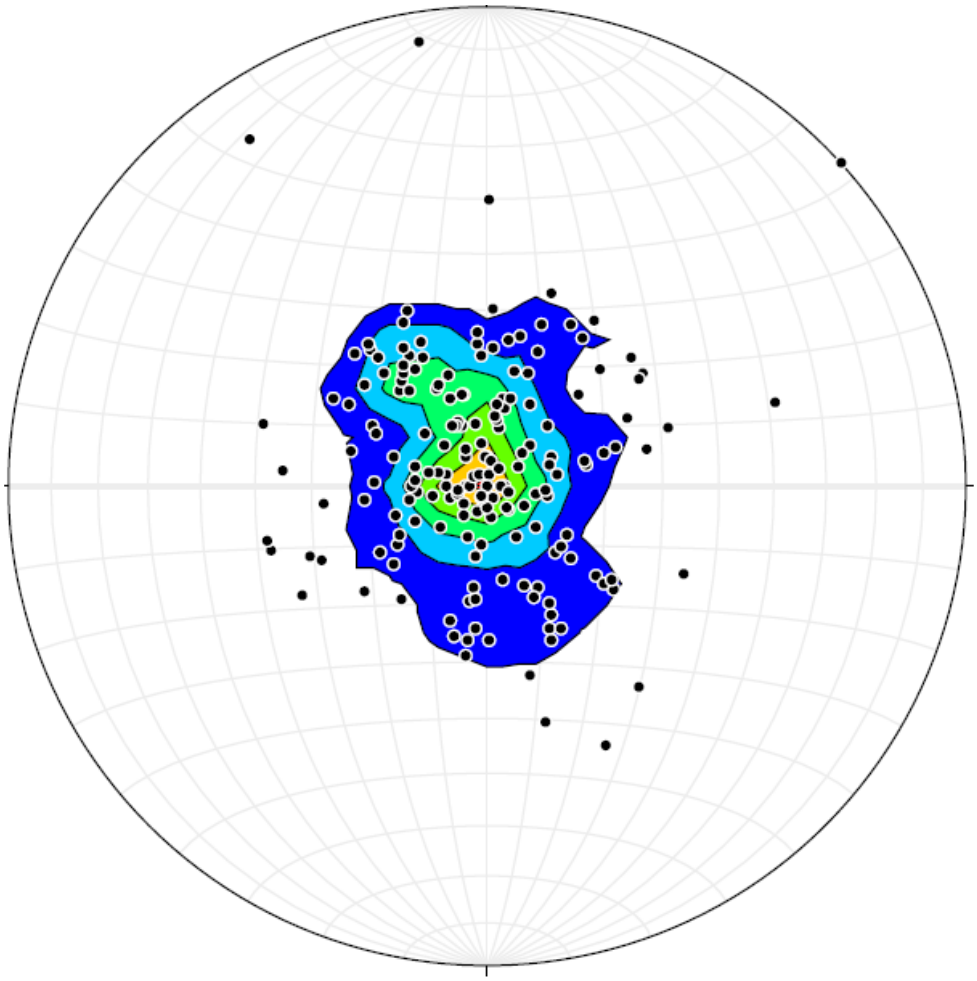

Figure 2.10 *Stereonet of magmatic fabric poles displayed alongside 1% area contouring with the contour interval spacing value set to 3%.*

2.2.2 Stereonet: Layering

Layering plotted on a stereonet (Figure 3.11) shows a greater proportion of measurements oriented WNW-ESE compared to the magmatic fabrics. The main population strikes N-S, with a secondary population striking E-W. A considerable amount of variation is also present as the Rose diagram shows lesser percentages of planes striking in almost every direction.

The pole distribution for layering measurements (Figure 3.12) is horizontal to sub-horizontal in the center and transitions to being sub vertical in the outer contours. The majority of poles are in the center of the stereonet, indicating most planes are sub-horizontal.

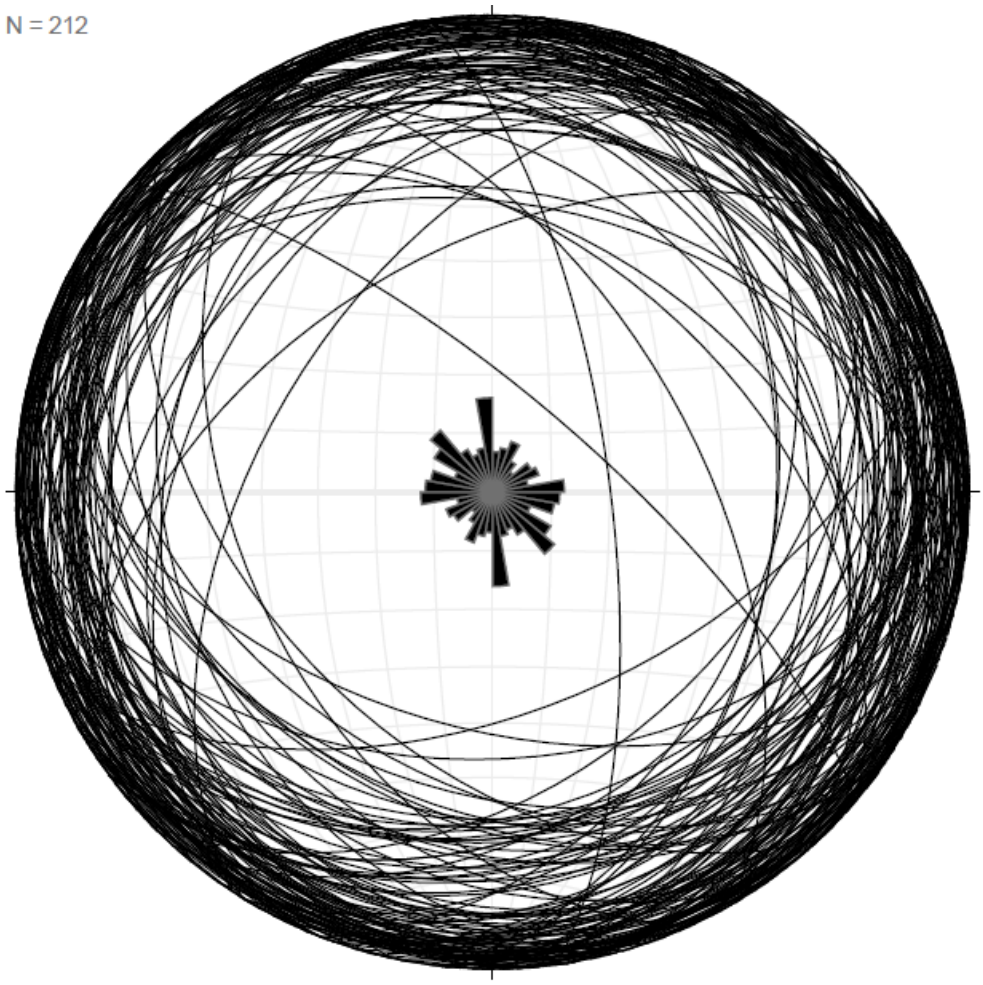

Figure 2.11 *Stereonet with respective poles of layering plotted.*

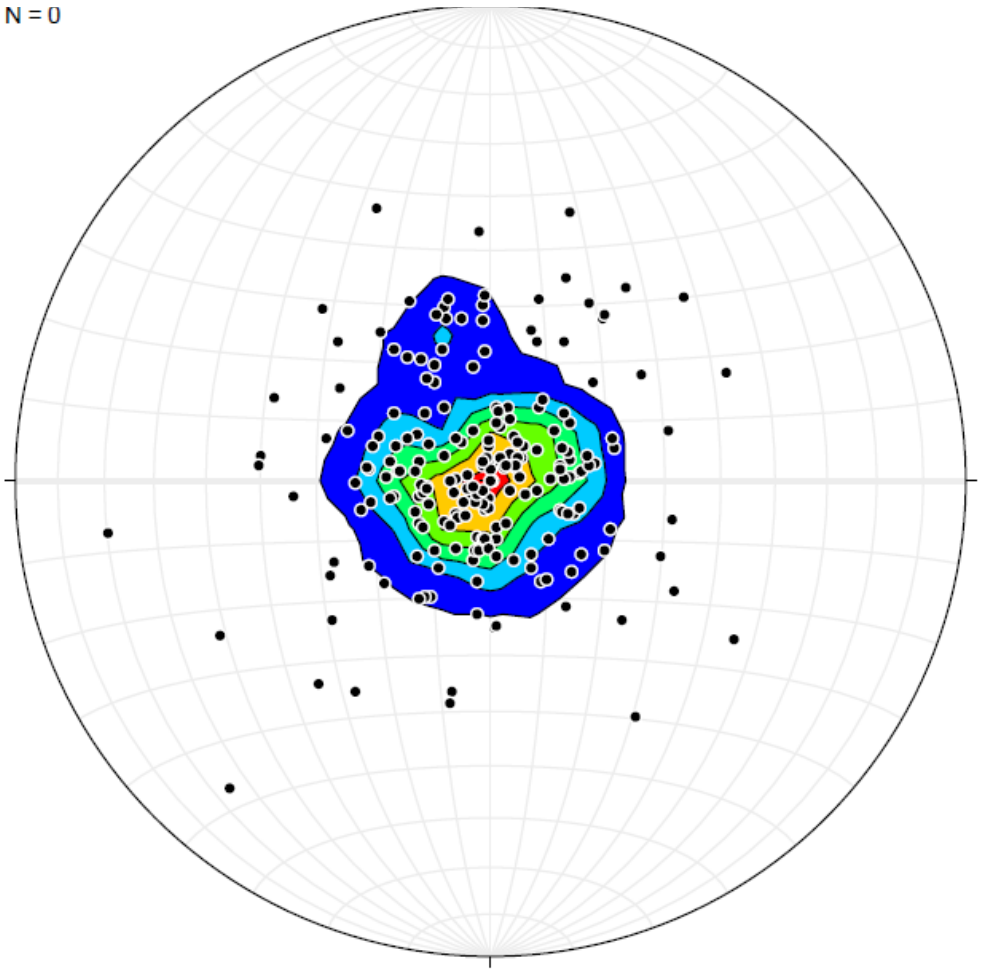

Figure 2.12 *Stereonet displaying poles to layering with 1% area contouring with contour spacing intervals of 3%.*

2.2.3 Stereonet: All Data

The stereonets constructed from all magmatic fabric and layering measurements (Figures. 3.13 and 3.14) show a high number of both steep and shallow dips oriented in several different directions. The largest population, however not by much, is ENE-WSW with a strike as low as 060.

Three subpopulations are evident and include strikes N-S, E-W, and NW-SE. The distribution of poles has a varied shape that ranges from horizontal to mostly sub-vertical, with the majority of poles indicating most planar features are sub-horizontal to shallowly dipping.

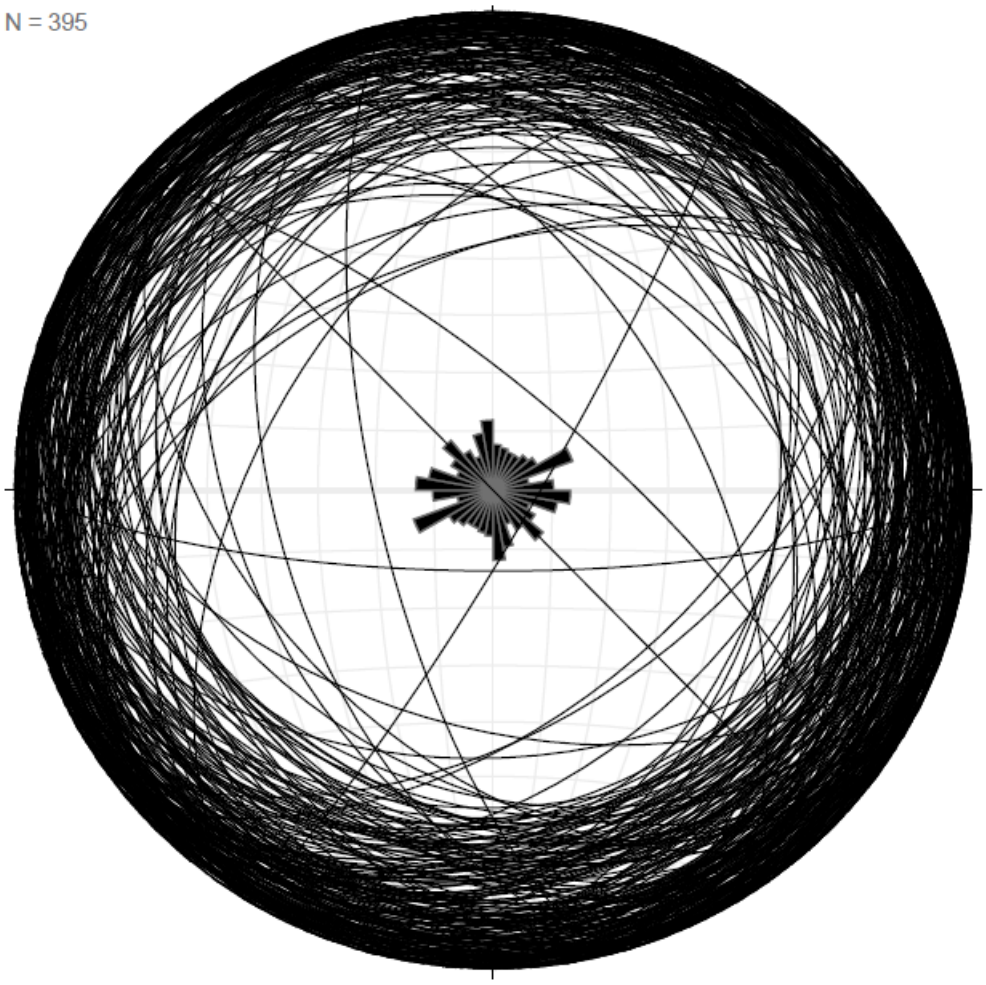

Figure 2.13 *Stereonet containing all data plotted as planes along with Rose diagram.*

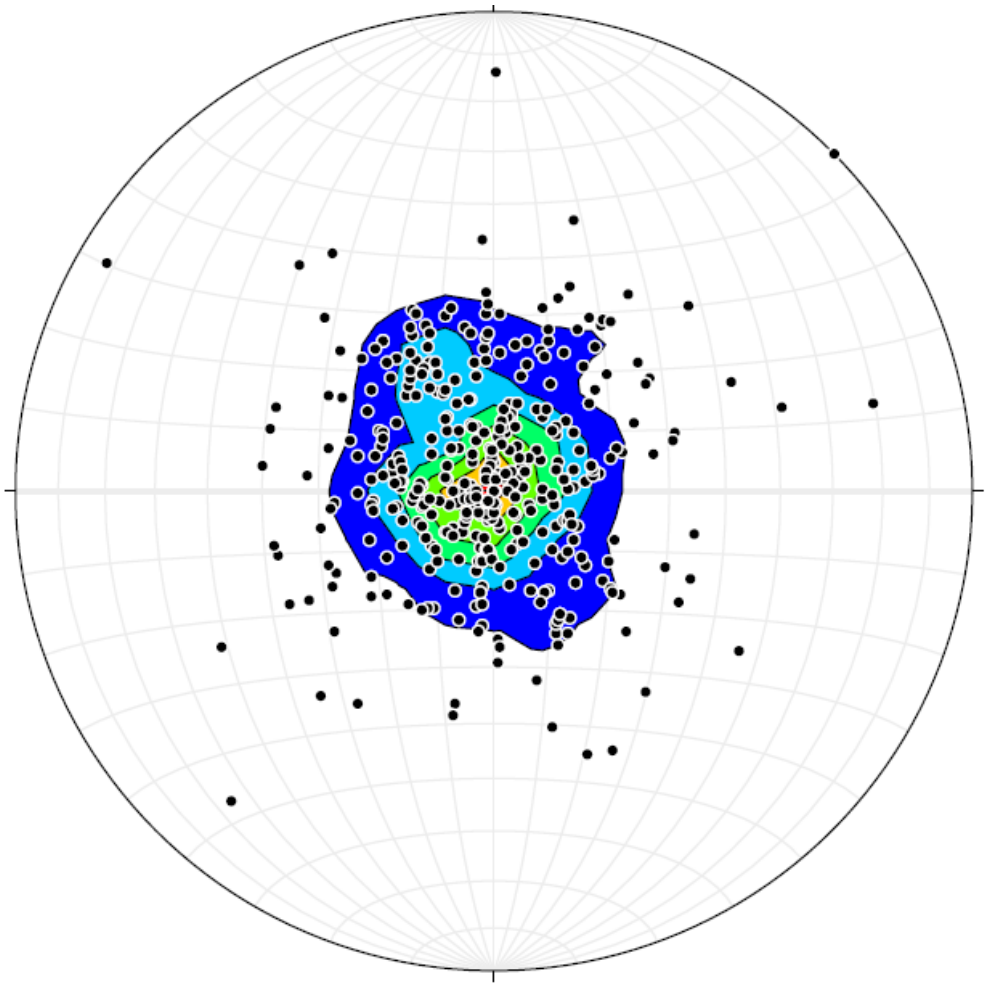

Figure 2.14 *Stereonet of all data displayed as poles and 1% area contouring with contour spacing intervals of 3%.*

2.2.4 Stereonet: High Confidence

The stereonets plotted from all magmatic fabric and layering measurements with a confidence value of either 4 or 5 (Figures 3.15 and 3.16) exhibit a relatively high amount of variance in plane direction and the distribution of poles. Planes visible in the Rose diagram extend in nearly every direction while the strongest pattern still strikes ENE-WSW in a similar manner to the stereonet plots for both magmatic fabrics and all data.

The second most pronounced pattern visible in this stereonet strikes east to west with a stike of 095. Two other subpopulations with nearly the same abundance include strikes that are N-S and NW-SE. The poles are mostly sub-horizontal and slightly more concentrated in the center contours compared to the plot of poles for all data sets.

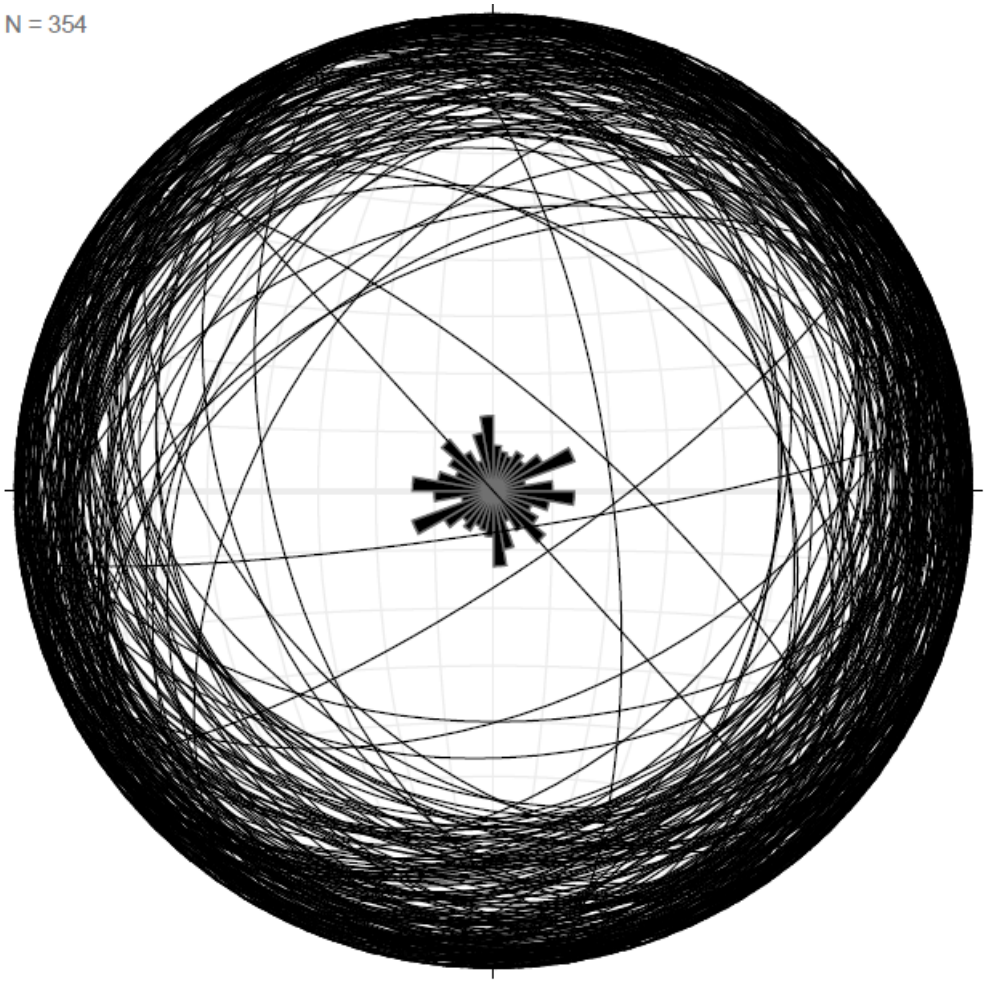

Figure 2.15 *Stereonet plot of all high confidence values plotted as planes and a Rose diagram.*

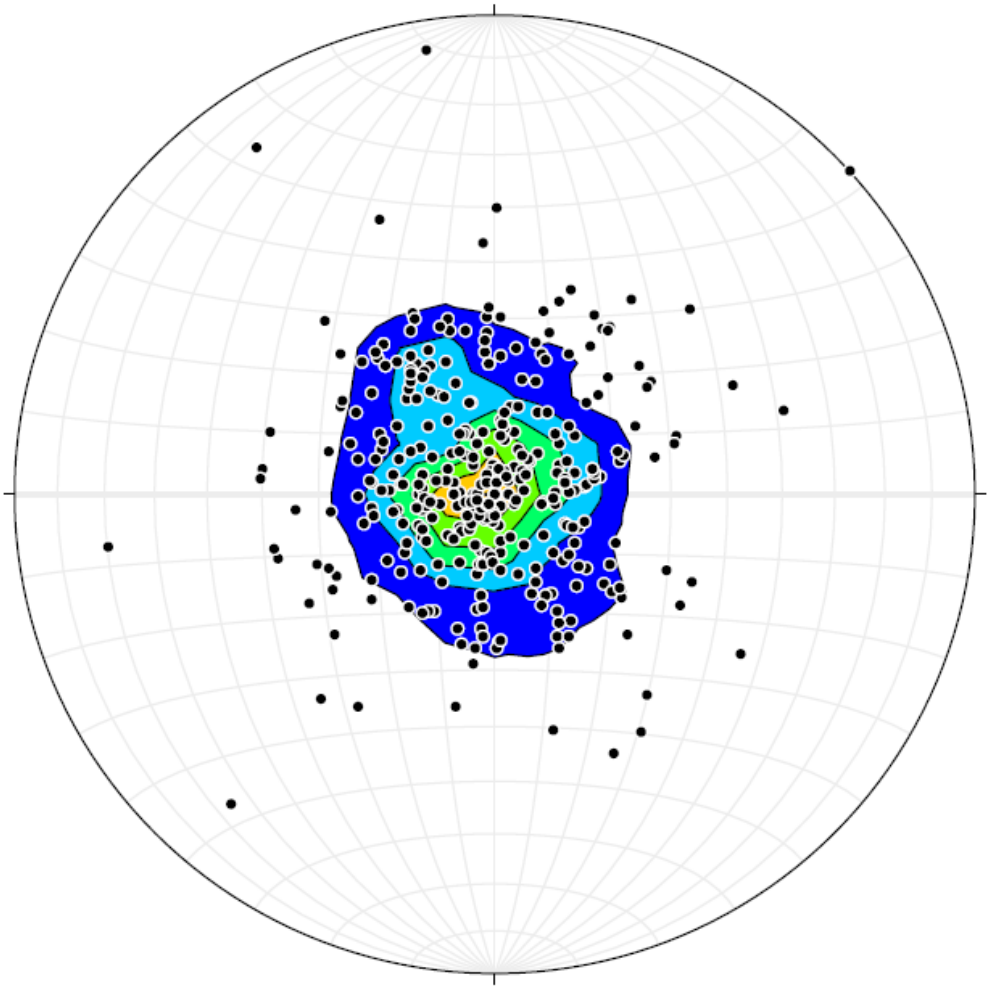

Figure 2.16 *Stereonet plot of high confidence poles with 1% area contours in intervals of 3%.*

2.3 Depth Bin Stereonets

The depths below Hole GT1 were separated into bins and plotted to stereonets in order to observe and compare changes to magmatic fabrics and layering orientation with increasing vertical distance below the surface. An interval of every 50 mbs was chosen for each depth bin so that orientation patterns would be visible without being too cluttered. Figures 3.17, 3.18, and 3.19 display the MF and layering stereonets for each depth bin beside one another to help visualize those changes with depth. The most common strike directions found from every stereonet are summarized in Table 1.

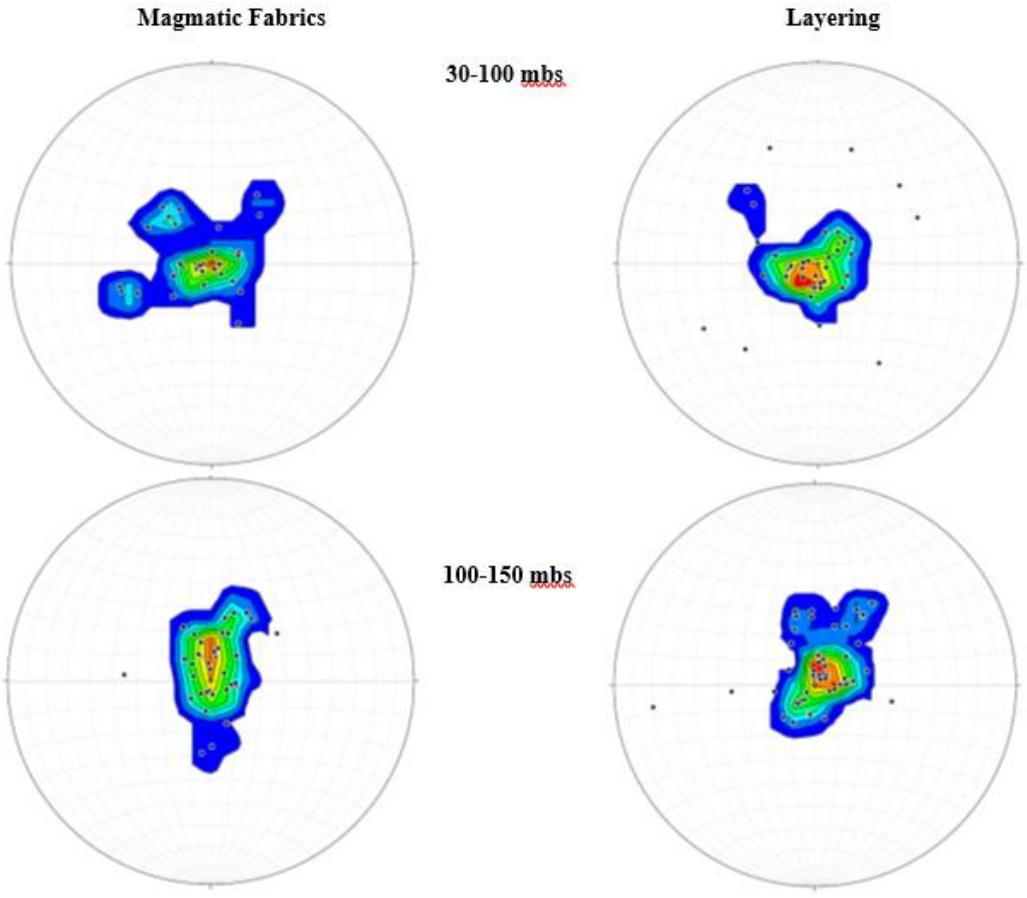

Figure 2.17 *Comparison between depth bin stereonets for magmatic fabrics and layering from 30mbs to 150mbs.*

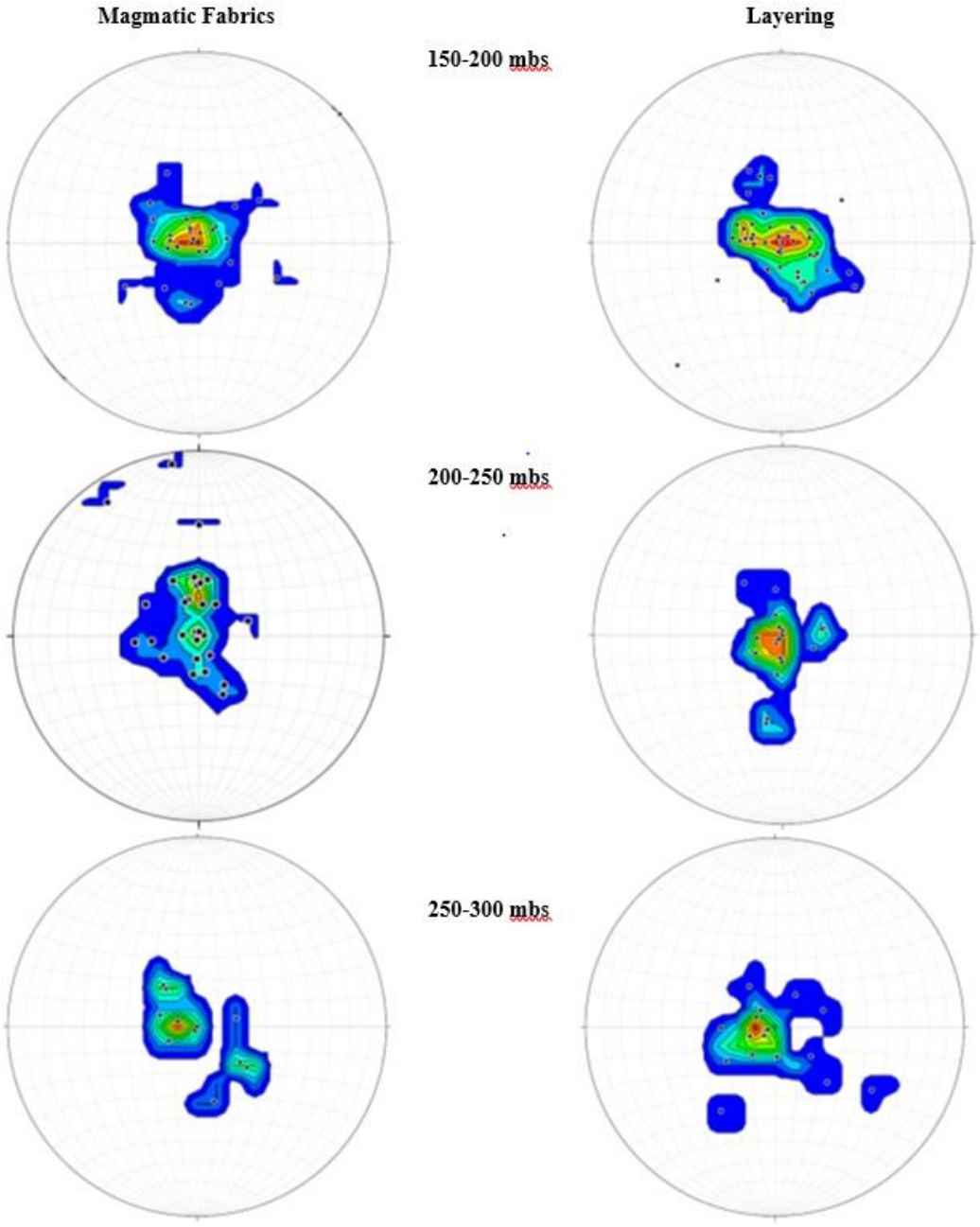

Figure 2.18 *Comparison between depth bin stereonets for magmatic fabrics and layering from 150mbs to 300mbs.*

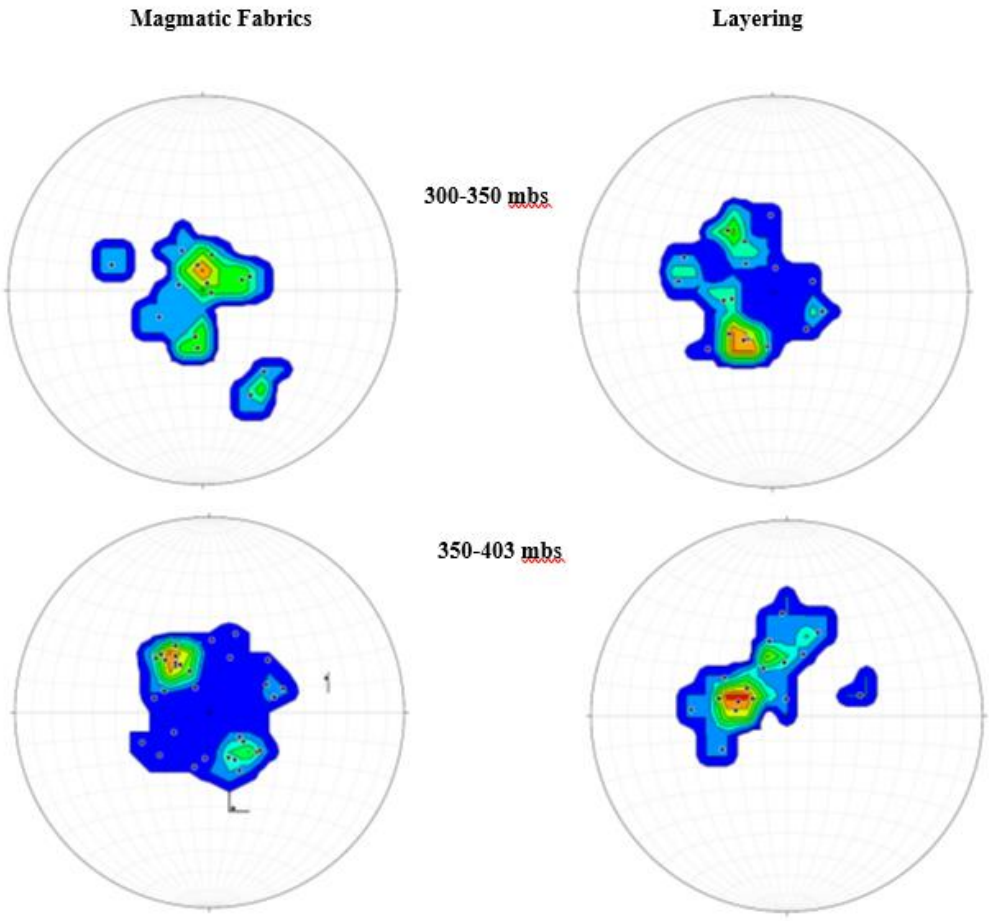

Figure 2.19 *Comparison between depth bin stereonets for magmatic fabrics and layering from 300mbs to 403mbs.*

Table 2.1 *Summary of strikes found for each feature type within the respective depth bin*

Depth Bin (mbs)	**All**	**MF**	**Layering**
30-100	NNE-SSW	NNE-SSW	WNW-ESE
100-150	WNW-ESE	ESE-WNW	N-S; NW-SE
150-200	ENE-WSW	NW-SE; ENE-WSW	N-S; ENE-WSW
200-250	WNW-ESE	E-W	WNW-ESE
250-300	NE-SW	ENE-WSW; NNE-SSW	NW-SE
300-350	E-W	NNE-SSW	NE-SW; NW-SE
350-403	ENE-WSW	NE-SW	E-W; NNE-SSW

2.3.2 Depth Bins: Magmatic Fabrics

2.3.2.1 MF Depth Bin: 30-100 Mbs (30 Measurements)

The stereonet plot of planes for all magmatic fabrics identified in the 30-100 mbs depth bin (Figure 3.20) shows a strong inclination for two major orientation patterns. Most planes on the Rose diagram strike NNW-SSE with small variations in strike that range from 150 to 180. The second largest pattern is much more focused (one main peak) and strikes NE-SW with an average strike of 042. A third, significantly weaker pattern also strikes NE-SW but with a strike of 063.

The distribution of poles is mostly scattered and sub-horizontal with only a few magmatic fabric measurements located within the central contour (Figure 3.21). The poles tend to be isolated into evenly spaced clusters that become more sparsely distributed in the outer contours. A girdle like pattern is evident from NE to SW indicating roughly N-S strike and dips towards the NE and SW.

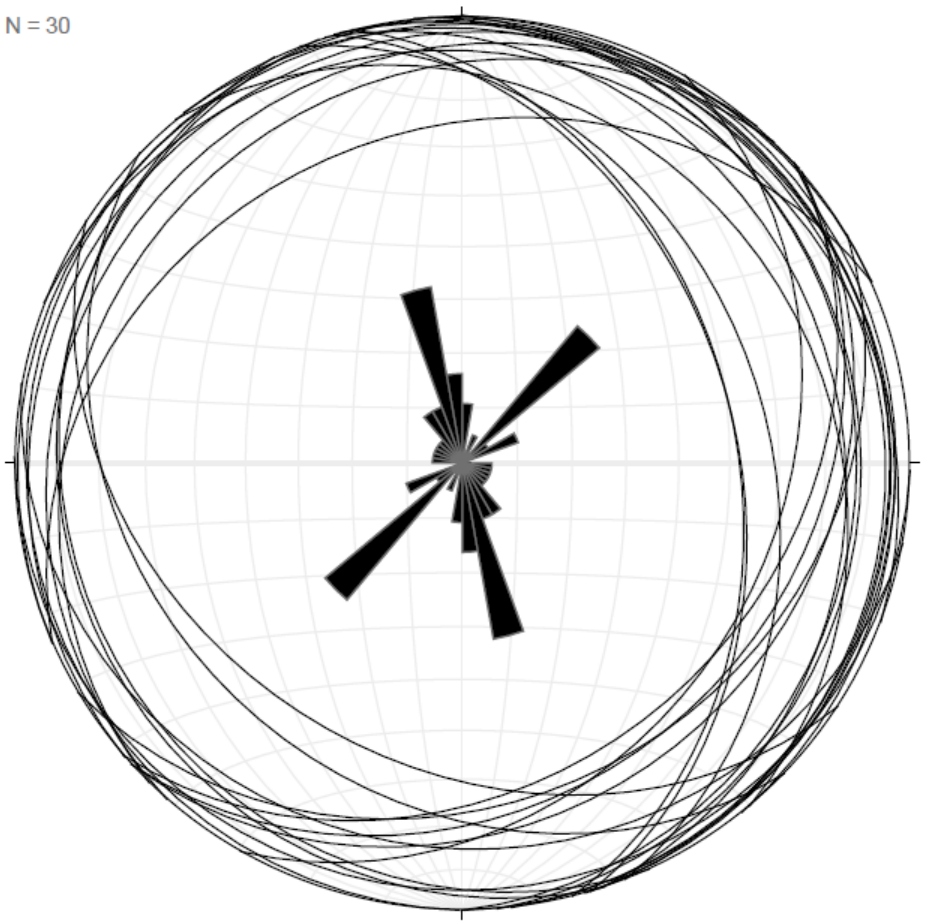

Figure 2.20 *Stereonet plot of dip strike for all MF measurements in the 30-100 mbs depth bin.*

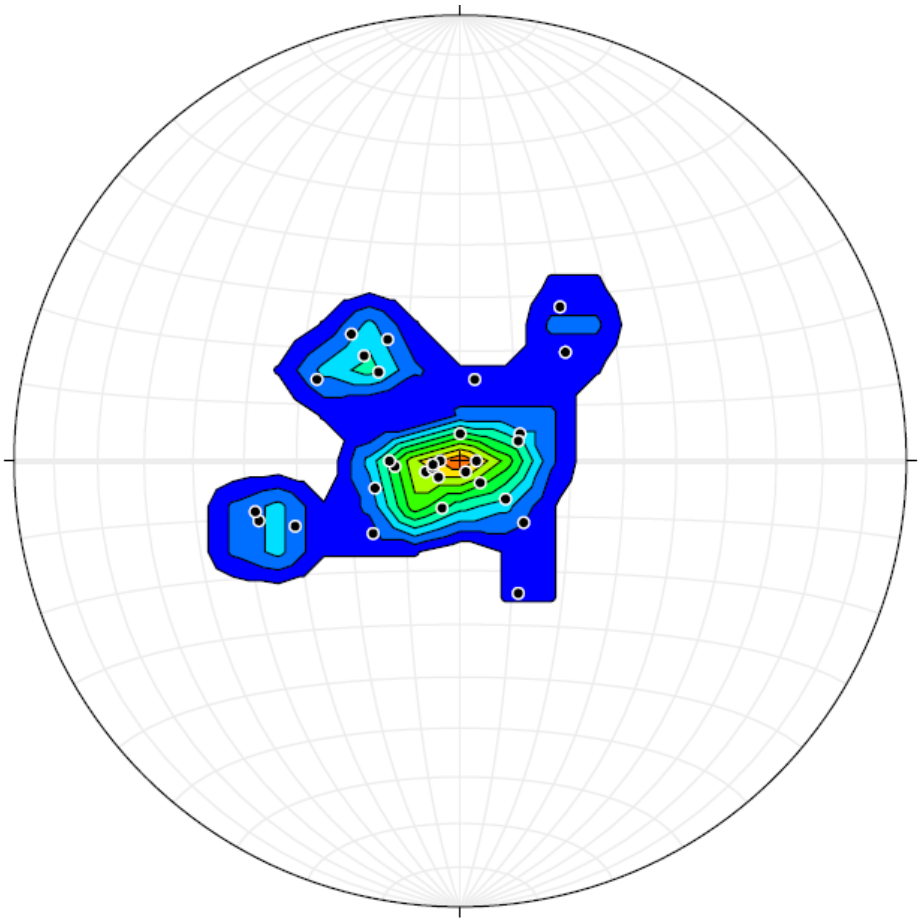

Figure 2.21 *Stereonet plot for all MF measurements in the 30-100 mbs depth bin as poles with 1% area contours in intervals of 3%.*

2.3.2.2 MF Depth Bin: 100-150 Mbs (37 Measurements)

The stereonet plot of planes for only magmatic fabrics in the 100-150 mbs depth bin (Figure 3.22) shows a strong pattern of WNW-ESE oriented strikes among some instances of variance. The second most prevalent pattern has an NNE-SSW strike and a general strike of 005 or 186.

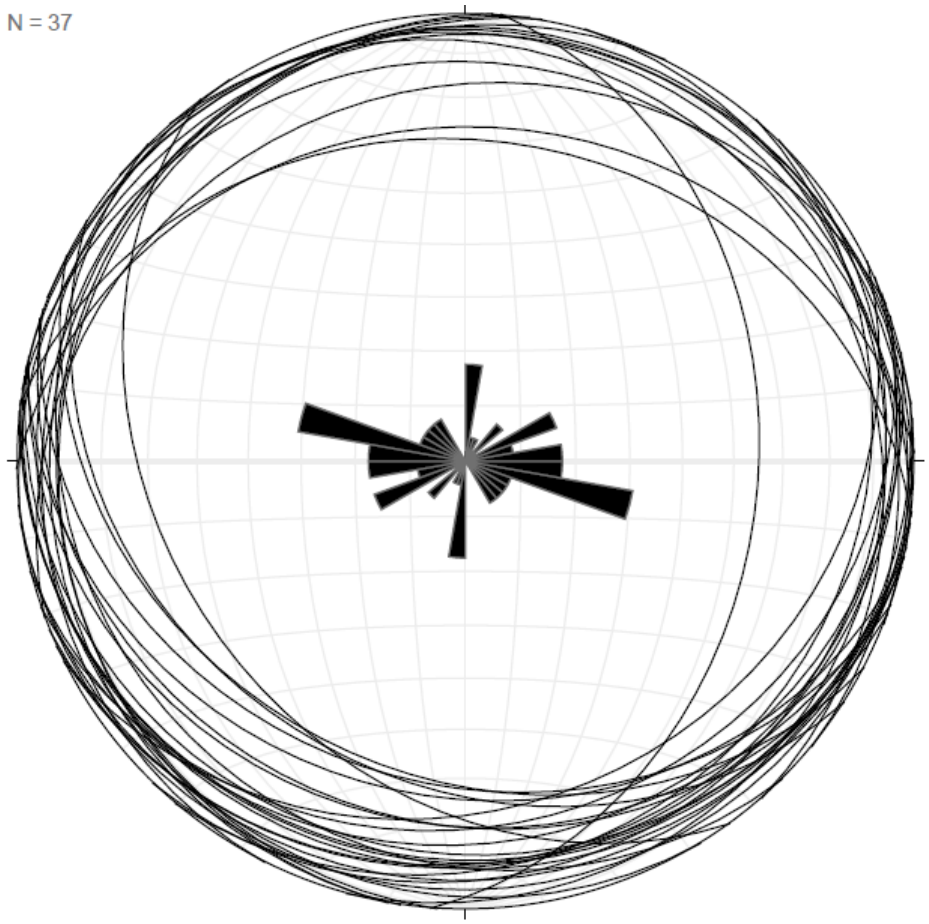

Figure 2.22 *Stereonet plot of dip and strike for all MF measurements in the 100-150 mbs depth bin.*

The pole and contour stereonet plot for magmatic fabrics in the 100-150 mbs depth bin (Figure 3.23) displays a sub-horizontal distribution of poles that are evenly spaced from one another between the inner and outer contours. A girdle like pattern is evident from N to S indicating roughly E-W strike and dips towards the N and S.

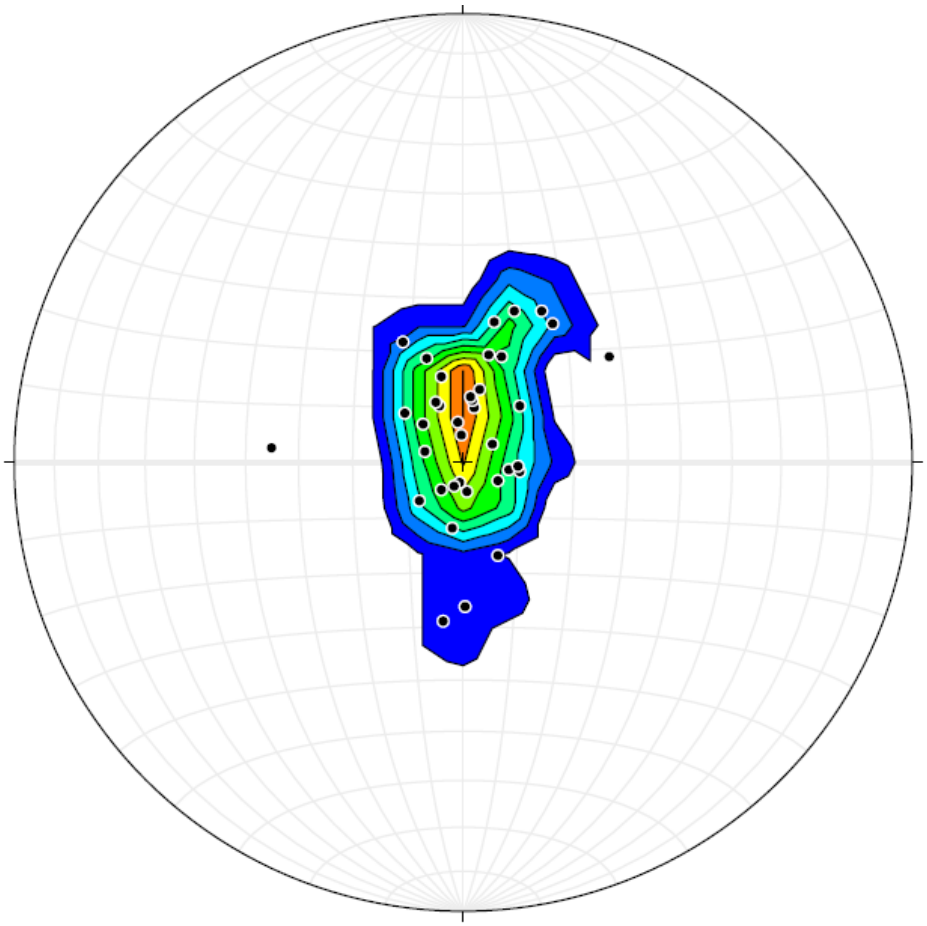

Figure 2.23 *Stereonet plot for all MF measurements in the 100-150 mbs depth bin as poles with 1% area contours in intervals of 3%.*

2.3.2.3 MF Depth Bin: 150-200 Mbs (29 Measurements)

The stereonet plot of planes for all magmatic fabrics in the 150-200 mbs bin (Figure 3.24) shows a wide range of strike directions apparent in the rose diagram. The two largest patterns strike NW-SE and ENE-WSW with average strike values of 135 and 066 respectively. Other subpopulations include strikes N-S and NE-SW.

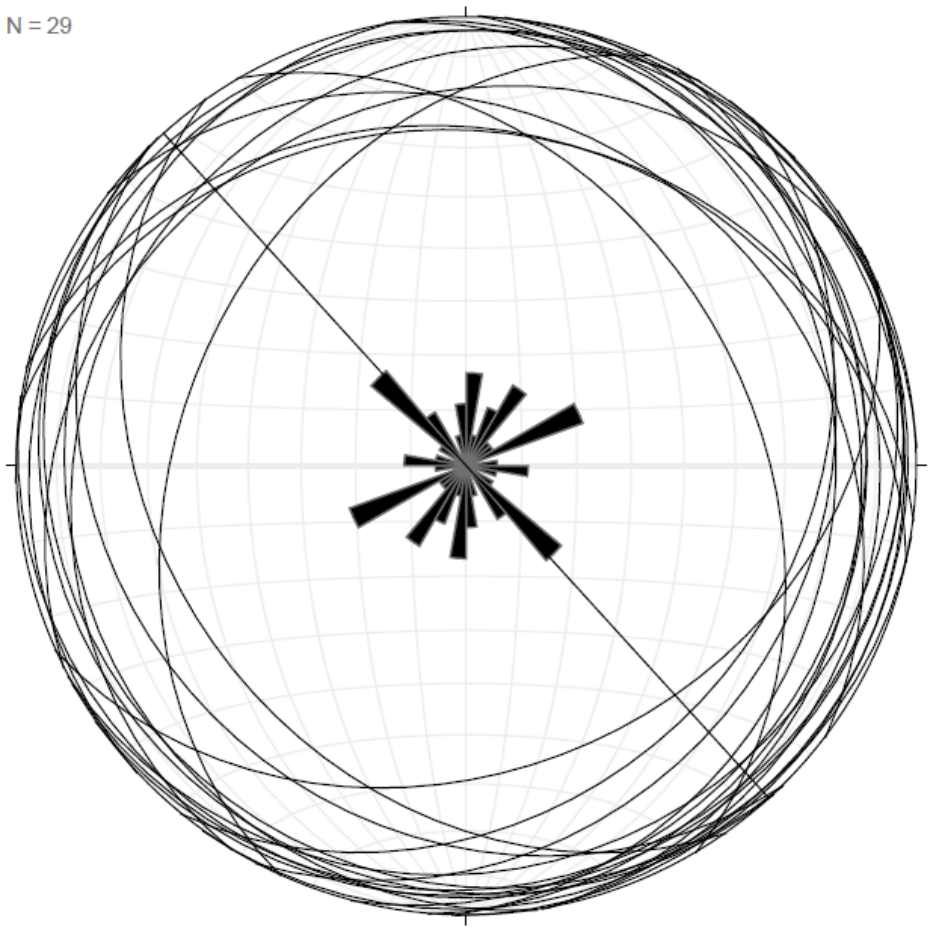

Figure 2.24 *Stereonet plot of dip and strike for all MF measurements in the 150-200 mbs depth bin.*

The stereonet plot of poles with contours for all magmatic fabrics in the 150-200 mbs bin (Figure 3.25) shows a spaced and variable distribution of poles that are sub-horizontal throughout the inner and outer contours.

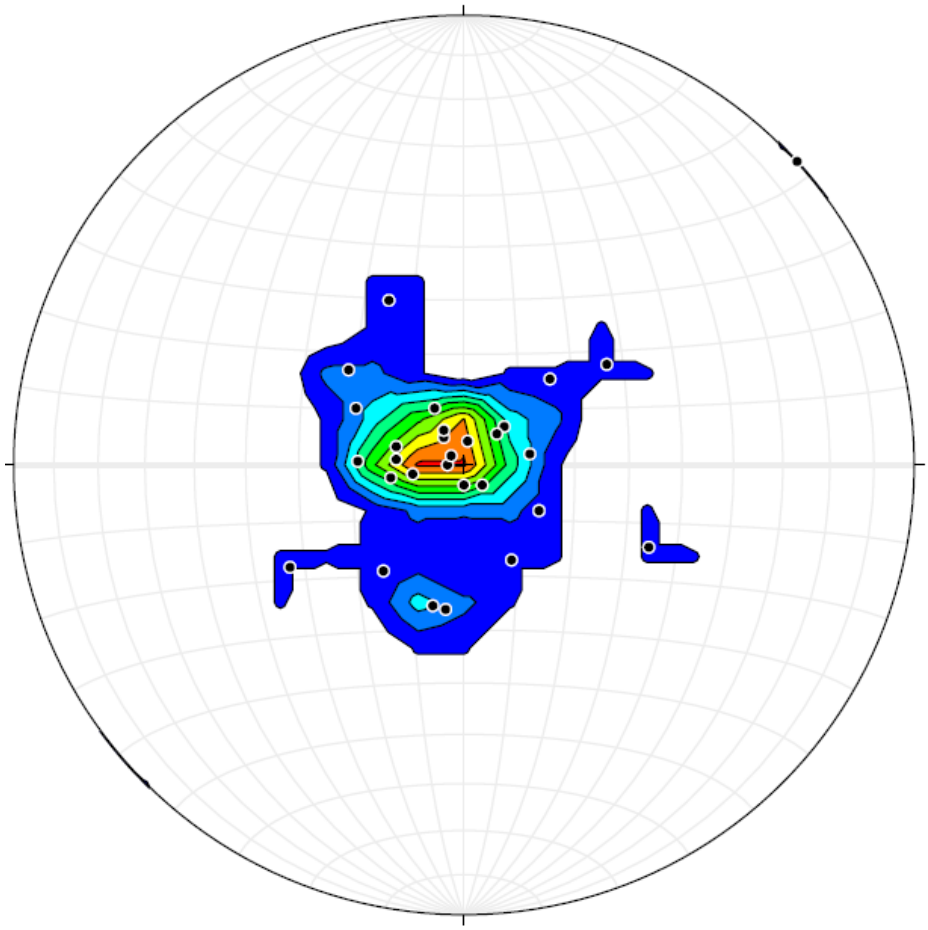

Figure 2.25 *Stereonet plot of all MF measurements in the 150-200 mbs depth bin as poles with 1% area contours in intervals of 3%.*

2.3.2.4 MF Depth Bin: 200-250 Mbs (29 Measurements)

The majority of magmatic fabrics within the 200-250 mbs depth bin (Figure 3.26) strike close to E-W with and average strike slightly above 095. The second most prevalent pattern strikes WNW-ESE with a strike close to 180.

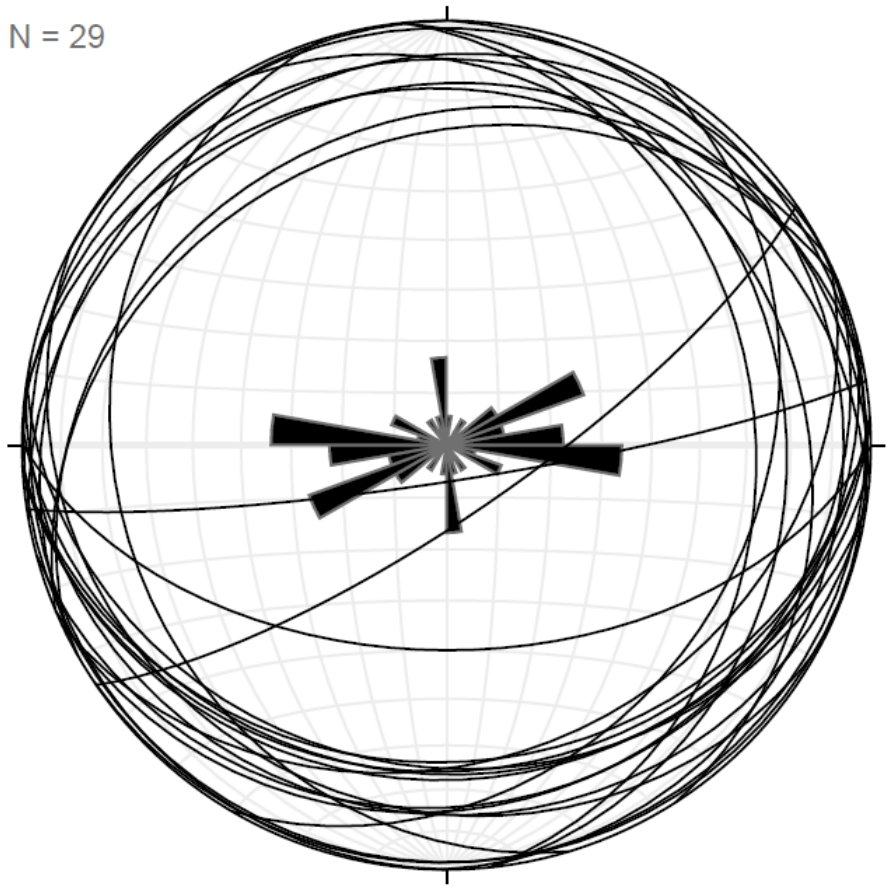

Figure 2.26 *Stereonet plot of dip and strike for all MF measurements in the 200-250 mbs depth bin.*

The 200-250 mbs bin (Figure 3.27) exhibits an almost completely vertical to sub-vertical distribution of poles. The poles form a dense cluster within the central contours and become slightly more spaced apart in the outer contours. The girdle pattern indicates a mostly E-W strike with N-S dips.

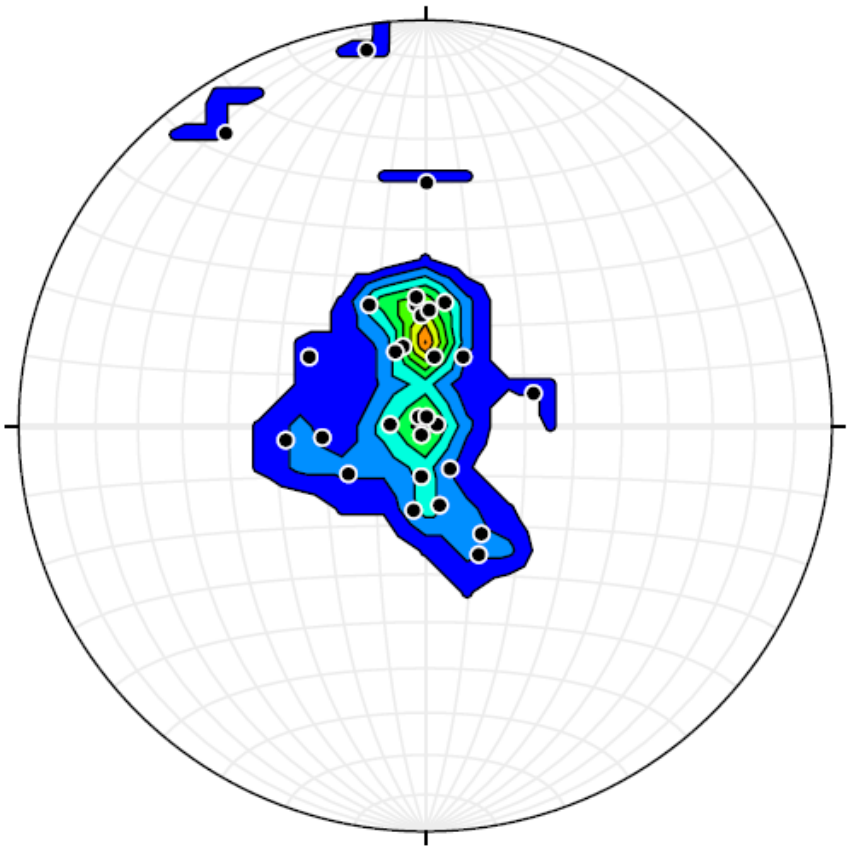

Figure 2.27 *Stereonet plot for all MF measurements in the 200-250 mbs depth bin as poles with 1% area contours in intervals of 3%.*

2.3.2.5 MF Depth Bin 250-300 Mbs (11 Measurements)

The stereonet plot and Rose diagram for exclusively magmatic fabrics in the 250-300 mbs depth bin (Figure 3.28) show that the most common strike direction is ENE-WSW with a trend value of either 013, 033, or 055.

The stereonet plot of poles for all magmatic fabrics within the 250-300 mbs depth bin (Figure 3.29) displays a distribution that is mostly sub-horizontal throughout the inner and outer contours with some deviation present among poles outside the outer contours. There is also a significant decline in the number of MF measurements overall.

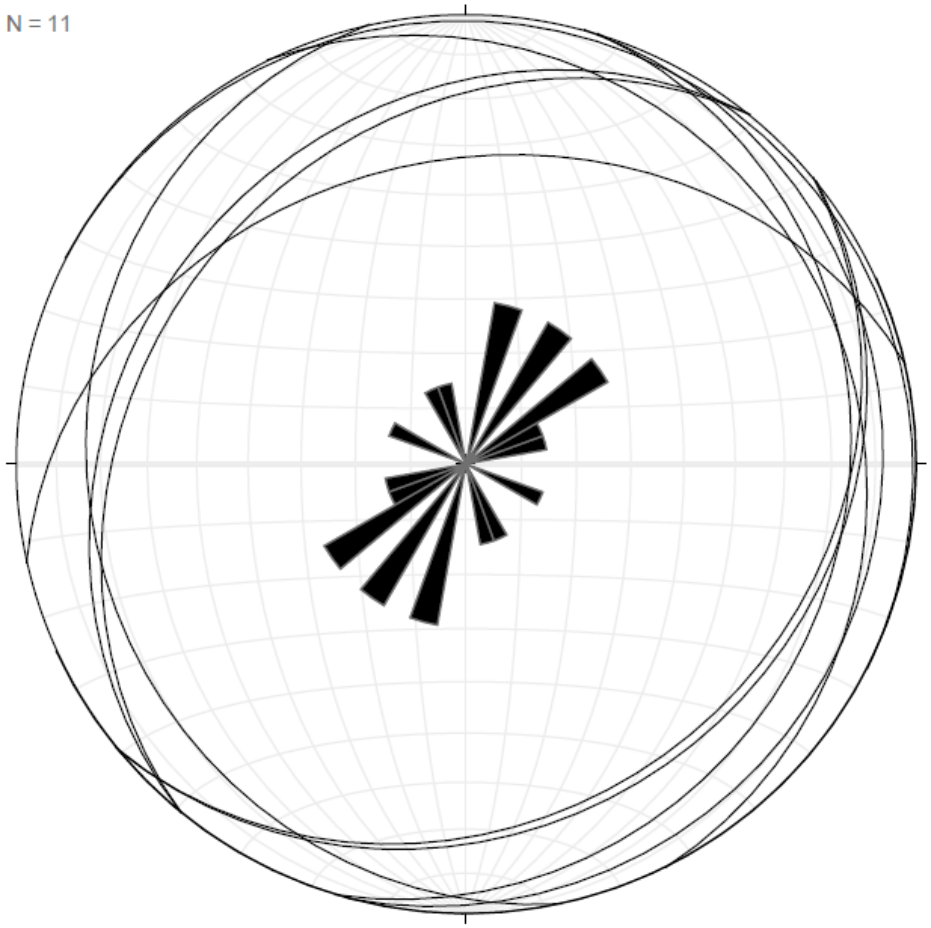

Figure 2.28 *Stereonet plot of dip and strike for all MF measurements in the 250-300 mbs depth bin.*

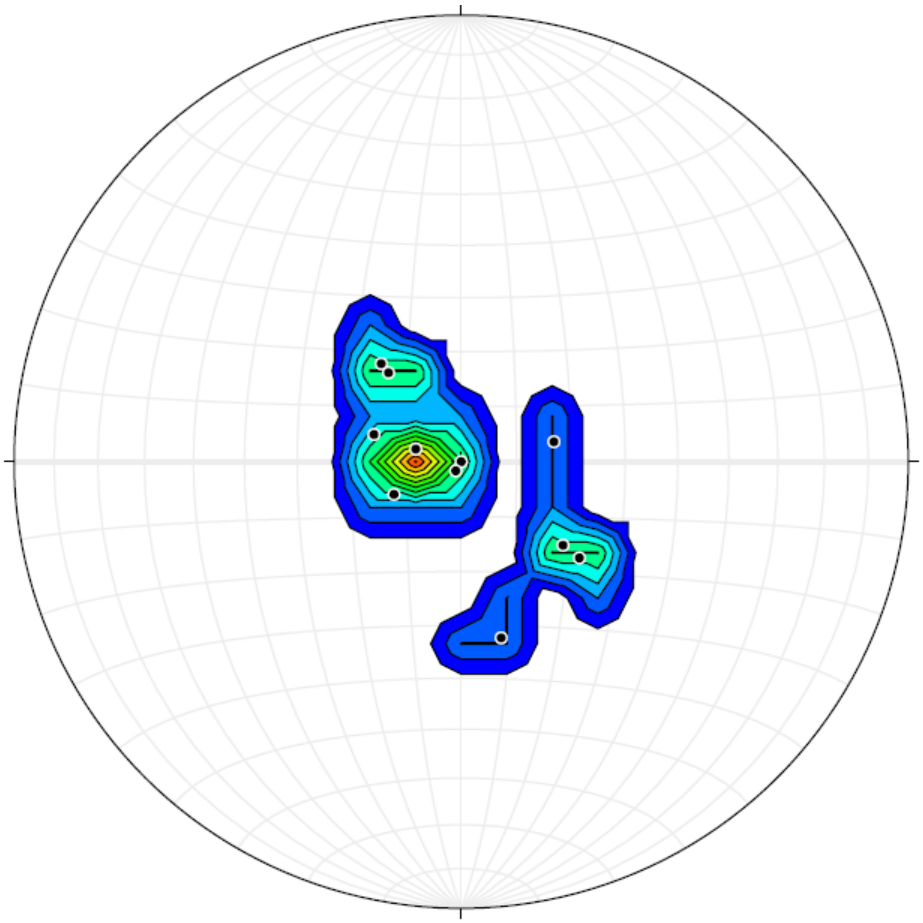

Figure 2.29 *Stereonet plot for all MF measurements in the 250-300 mbs depth bin as poles with 1% area contours in intervals of 3%.*

2.3.2.6 MF Depth Bin: 300-350 Mbs (14 Measurements)

The stereonet plot for all magmatic fabrics in the 300-350 mbs depth bin (Figure 3.30) shows that the majority of planes strike NE-SW with an average trend value of 014. One weaker pattern also strikes NE-SW and has a trend of 063 while the remaining patterns have NW to SE strikes.

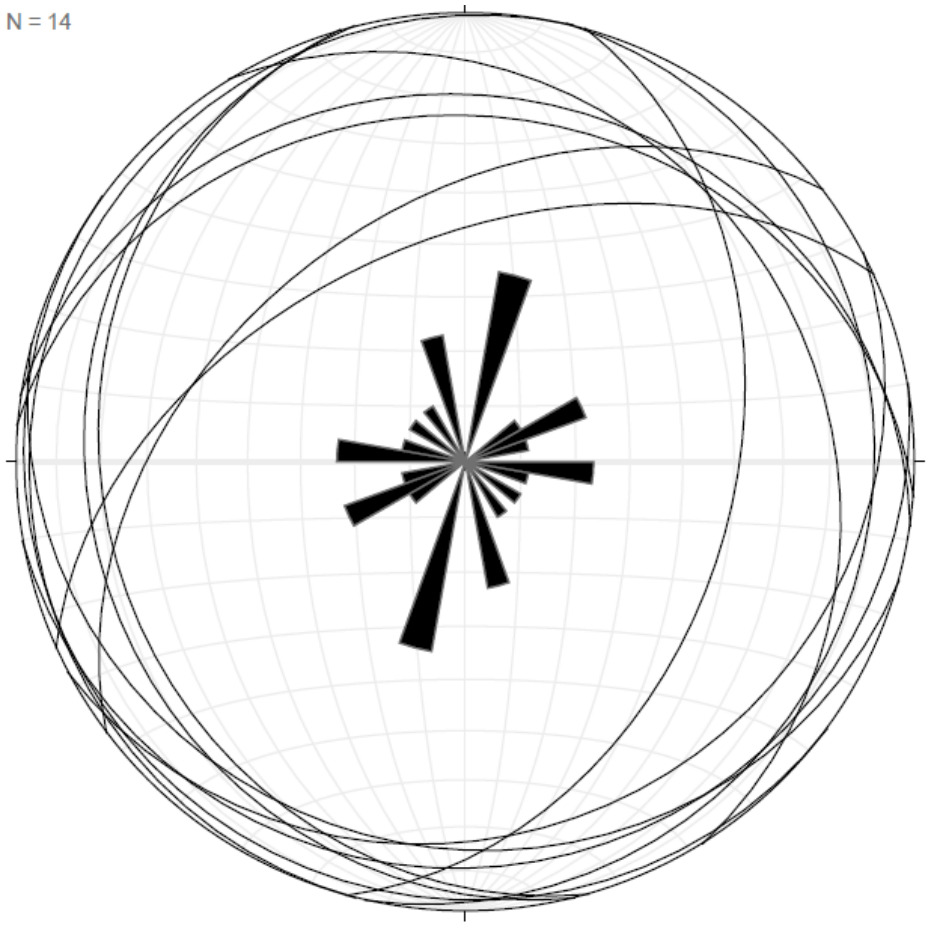

Figure 2.30 *Stereonet plot of dip and strike for all MF measurements in the 300-350 mbs depth bin.*

The stereonet plot of poles for all magmatic fabric measurements in the 300-350 mbs bin (Figure 3.31) displays a sub-vertical distribution of poles between the inner and outer contours.

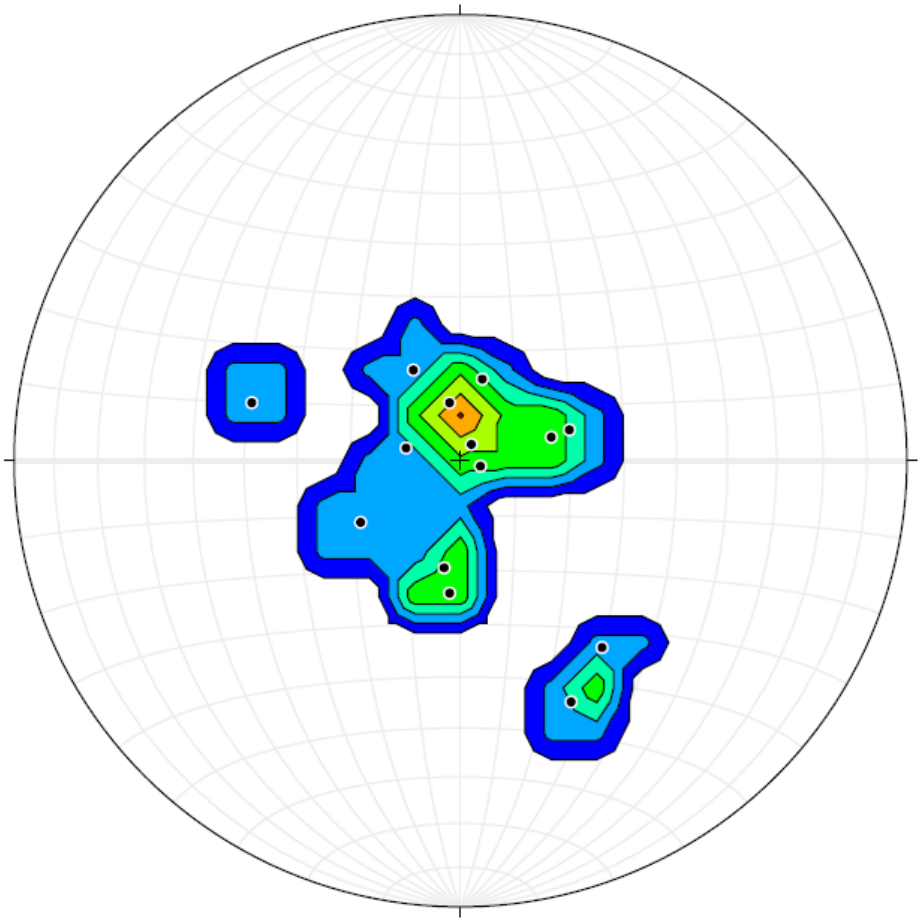

Figure 2.31 *Stereonet plot for all MF measurements in the 300-350 mbs depth bin as poles with 1% area contours in intervals of 3%.*

2.3.2.7 MF Depth Bin: 350-403 Mbs (33 Measurements)

The strongest pattern present in the plot of planes for all magmatic fabrics in the 350-403 mbs depth bin (Figure 3.32) has a NE-SW strike and an average trend of 063. Most other planes have either a E-W or NNW-SSE strike.

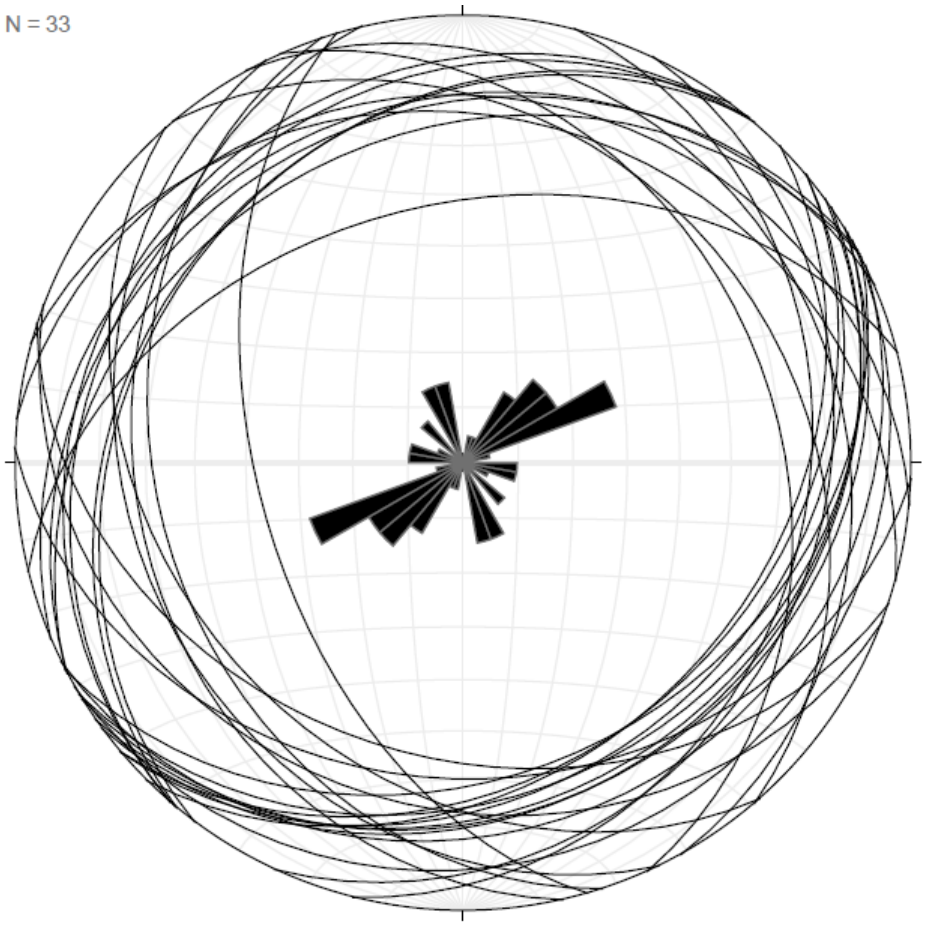

Figure 2.32 *Stereonet plot of dip and strike for all MF measurements in the 350-403 mbs depth bin.*

The pole distribution for magmatic fabrics in the 350-403 mbs depth bin (Figure 3.33) is initially vertical to sub-vertical in the center contours and becomes slightly more sub-horizontal in the outer contours. A double bull's eye pattern indicates most MFs strike NE-SW and dip either NW or SE.

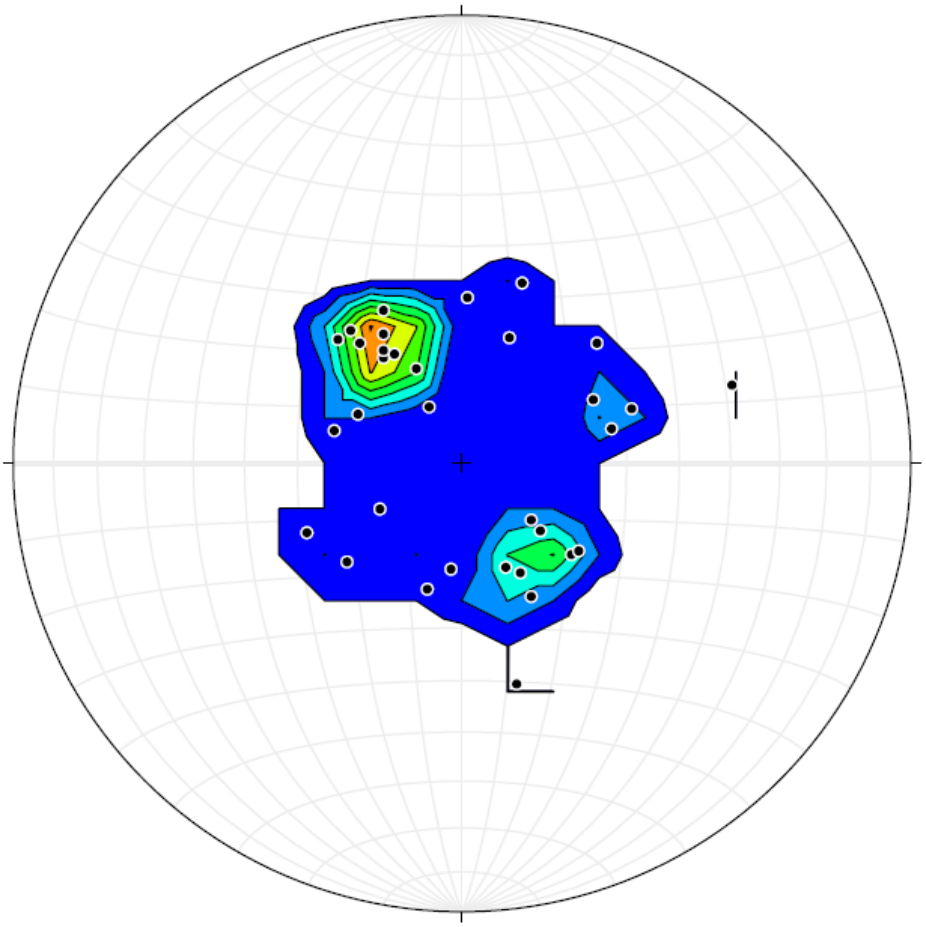

Figure 2.33 *Stereonet plot for all MF measurements in the 350-403 mbs depth bin as poles with 1% area contours in intervals of 3%.*

2.3.3 Depth Bins: Layering

2.3.3.1 Layering Depth Bin: 30-100 Mbs (38 Measurements)

The stereonet plot of planes for all layering measurements in the 30-100 mbs interval exhibits a wide range of differing orientations that radiate from nearly every direction in the Rose diagram (Figure 3.34). The highest number of layering measurements strike ESE-WNW with a general strike of 105 or 287. A slightly smaller pattern of layering measurements covers a much broader range of NW-SE oriented strikes. The strike value associated with these planes ranges from 133 to 172. The lesser patterns of layering have strikes in three subpopulations to the NE and SW.

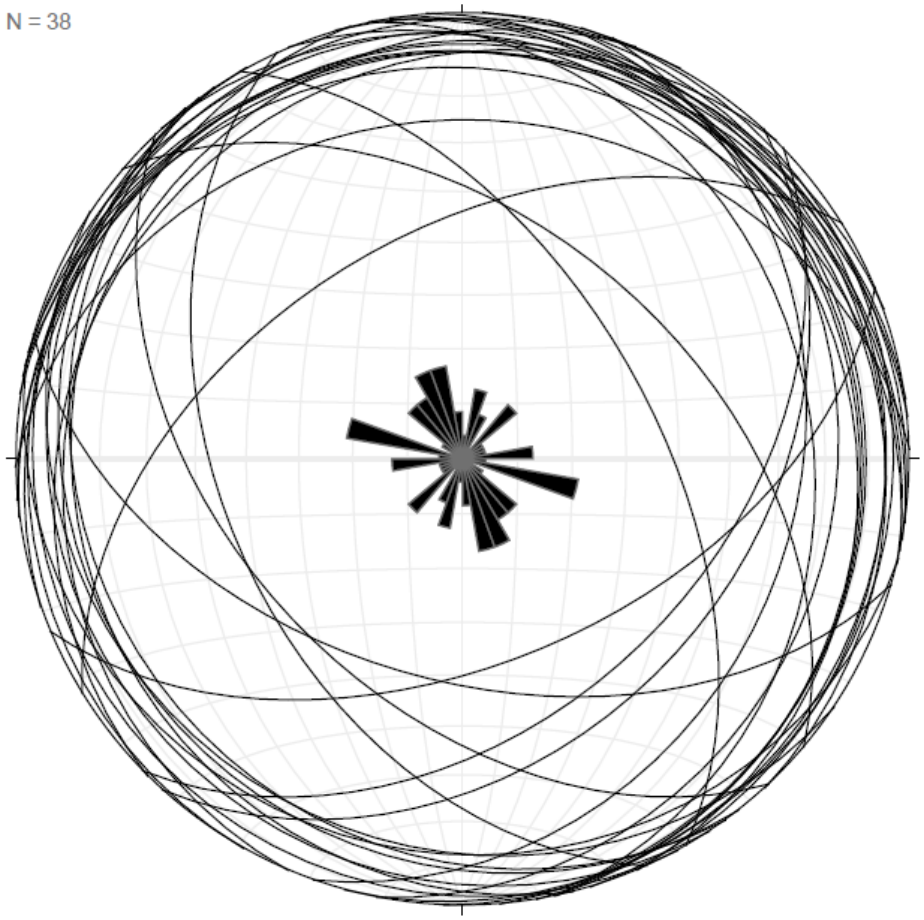

Figure 2.34 *Stereonet plot of dip and strike for all layering measurements in the 30-100 mbs depth bin.*

The distribution of poles for all layering measurements in the 30-100 mbs depth bin (Figure 3.35) is mostly sub-horizontal and the poles are moderately spaced apart from one another with the exception of small clusters located just outside of the center contours. A girdle like pattern is evident from NE to SW indicating roughly N-S strike and dips towards the NE and SW.

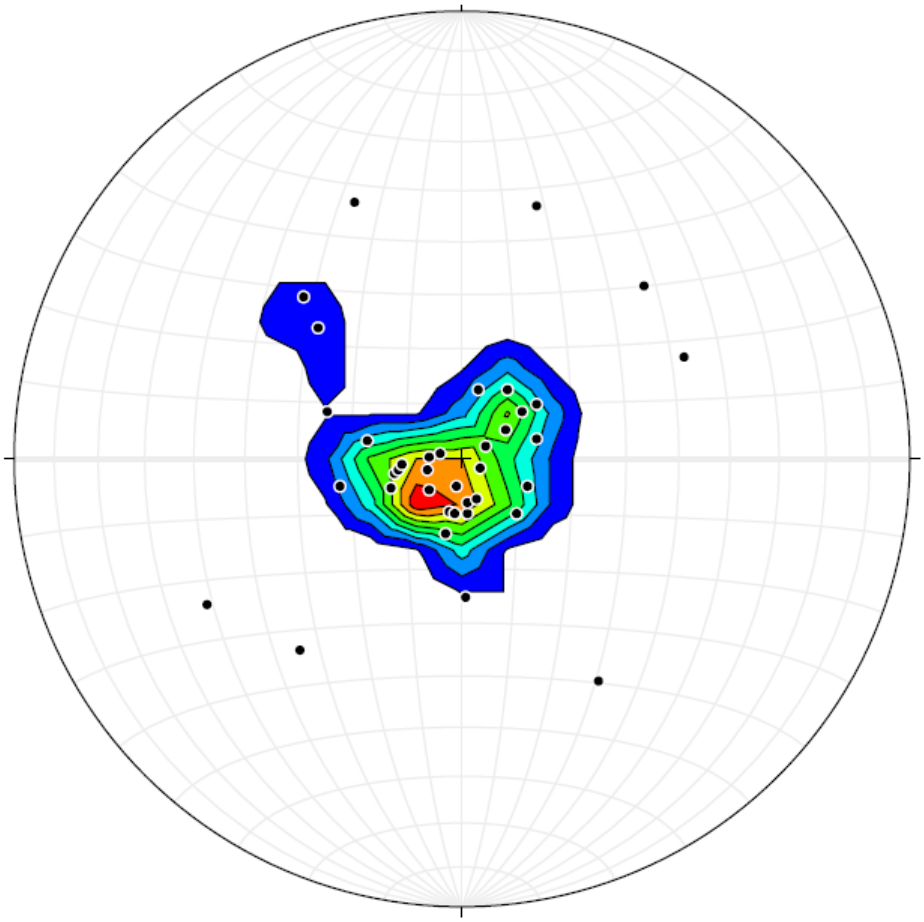

Figure 2.35 *Stereonet plot for all layering measurements in the 30-100 mbs depth bin as poles with 1% area contours in intervals of 3%.*

2.3.3.2 Layering Depth Bin: 100-150 Mbs (55 Measurements)

The stereonet plot of planes and Rose diagram for all layering measurements in the 100-150 mbs bin (Figure 3.36) displays two major patterns in orientation. The slightly larger pattern strikes NW-SE with a strike of 135 and is accompanied by a wide range of lesser measurements with similar strikes. The other major pattern has a WNW-ESE strike with a value of 178. Subpopulations strike from NW-SE to E-W.

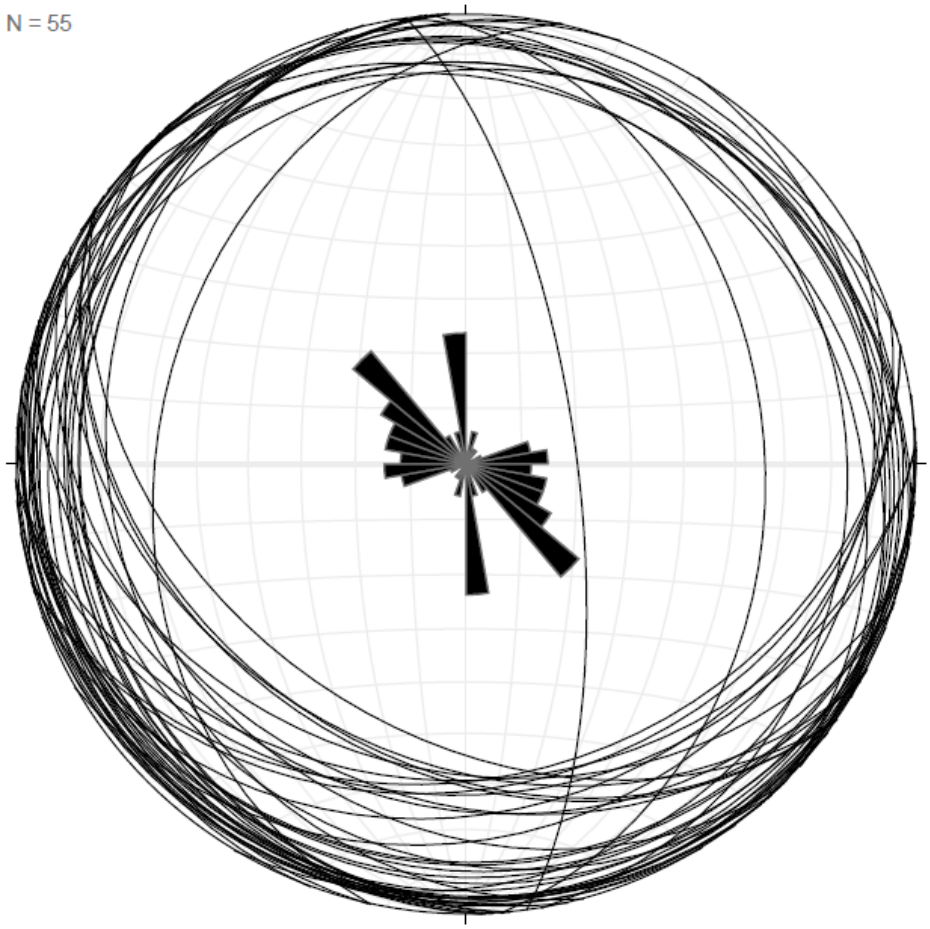

Figure 2.36 *Stereonet plot of dip and strike for all layering measurements in the 100-150 mbs depth bin.*

The stereonet plot of poles for layering measurements in the 100-150 mbs depth bin (Figure 3.37) displays a relatively varied arrangement of poles that is sub-horizontal in the central contours. A girdle like pattern is evident from NE to SW indicating roughly N-S strike and dips towards the NE and SW.

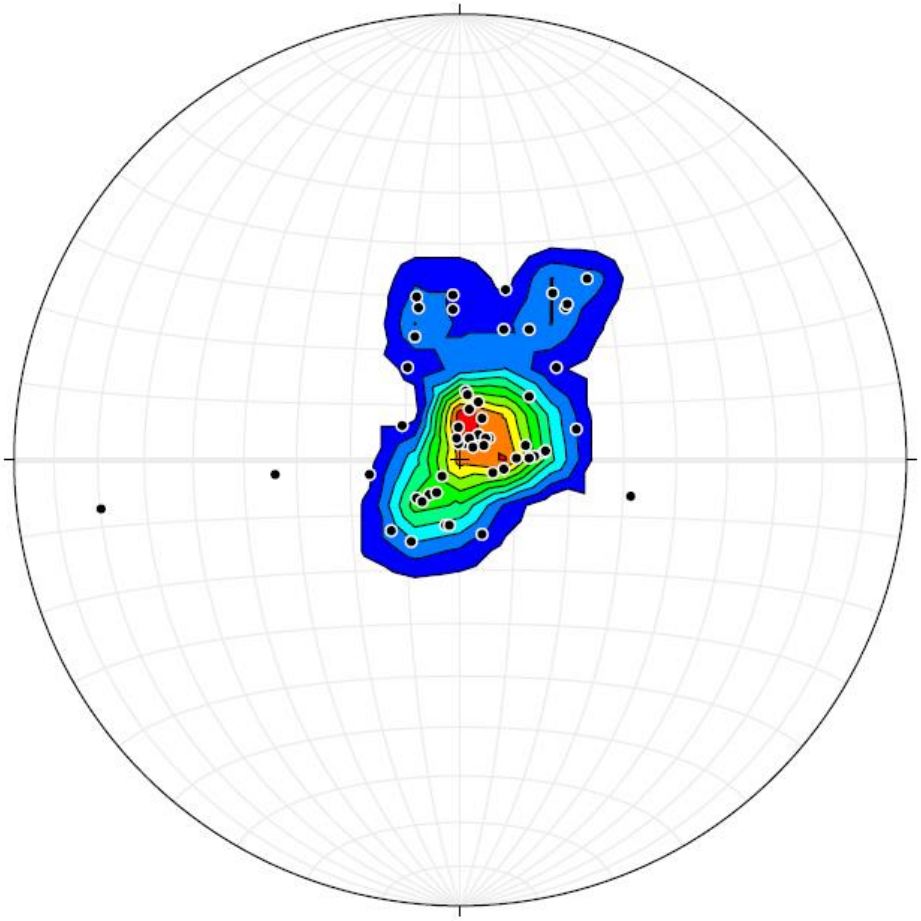

Figure 2.37 *Stereonet plot for all layering measurements in the 100-150 mbs depth bin as poles with 1% area contours in intervals of 3%.*

2.3.3.3 Layering Depth Bin: 150-200 Mbs (47 Measurements)

The plot of planes for all layering measurements in the 150-200 mbs depth bin exhibits a varying distribution of strike directions on the respective Rose diagram (Figure 3.38). The most pronounced pattern of strike is oriented ENE-WSW with an average

trend of 064. One other major pattern strikes broadly N-S with an average trend that ranges from 173 to 193. There are other subpopulations that strike E-W, NNE-SSW, and NW-SE.

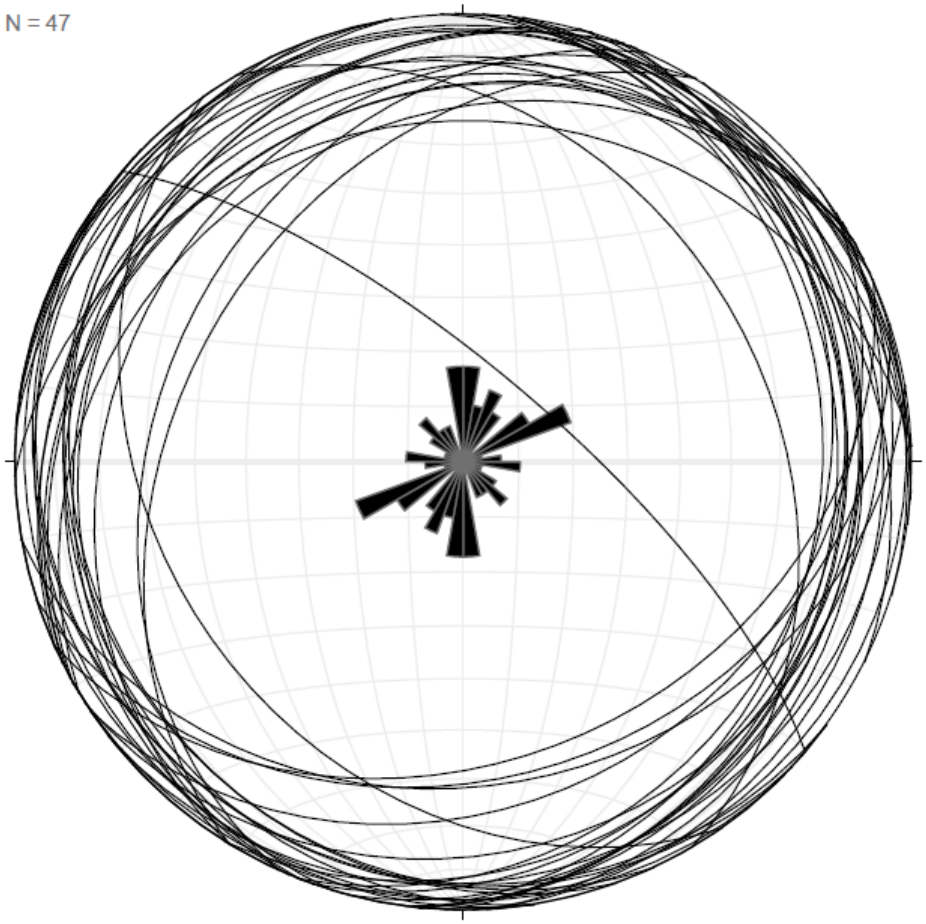

Figure 2.38 *Stereonet plot of all layering measurements in the 150-200 mbs depth bin as poles with 1% area contours in intervals of 3%.*

The stereonet plot of poles for all layering measurements in the 150-200 mbs depth bin (Figure 3.39) shows a horizontal to sub horizontal distribution of poles within the central contours. The girdle pattern is E-W with strikes mostly N-S and dips to the E and W.

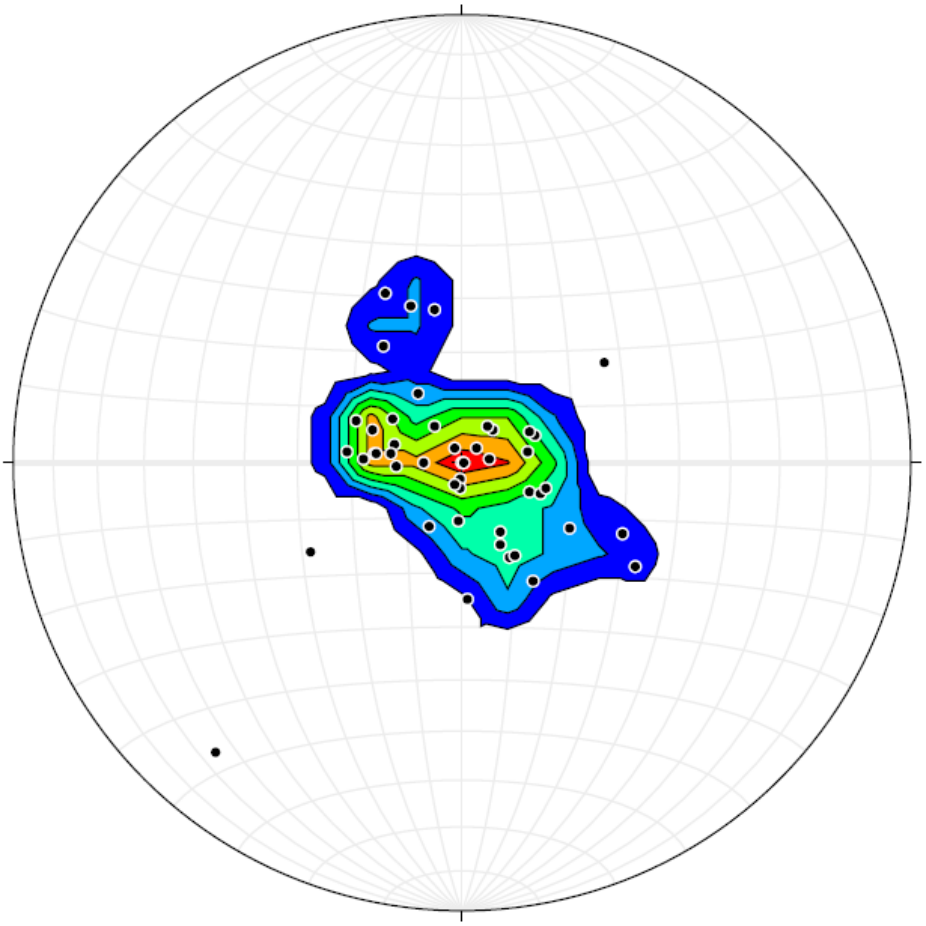

Figure 2.39 *Stereonet plot of all layering measurements in the 150-200 mbs depth bin as poles with 1% area contours in intervals of 3%.*

2.3.3.4 Layering Depth Bin: 200-250 Mbs (20 Measurements)

The vast majority of layering measurements in the 200-250 mbs depth bin share a WNW-ESE strike and an average trend of 094 when plotted on the Rose diagram (Figure 3.40). There are also subpopulations that strike N-S, NW-SE, and WNW-ESE.

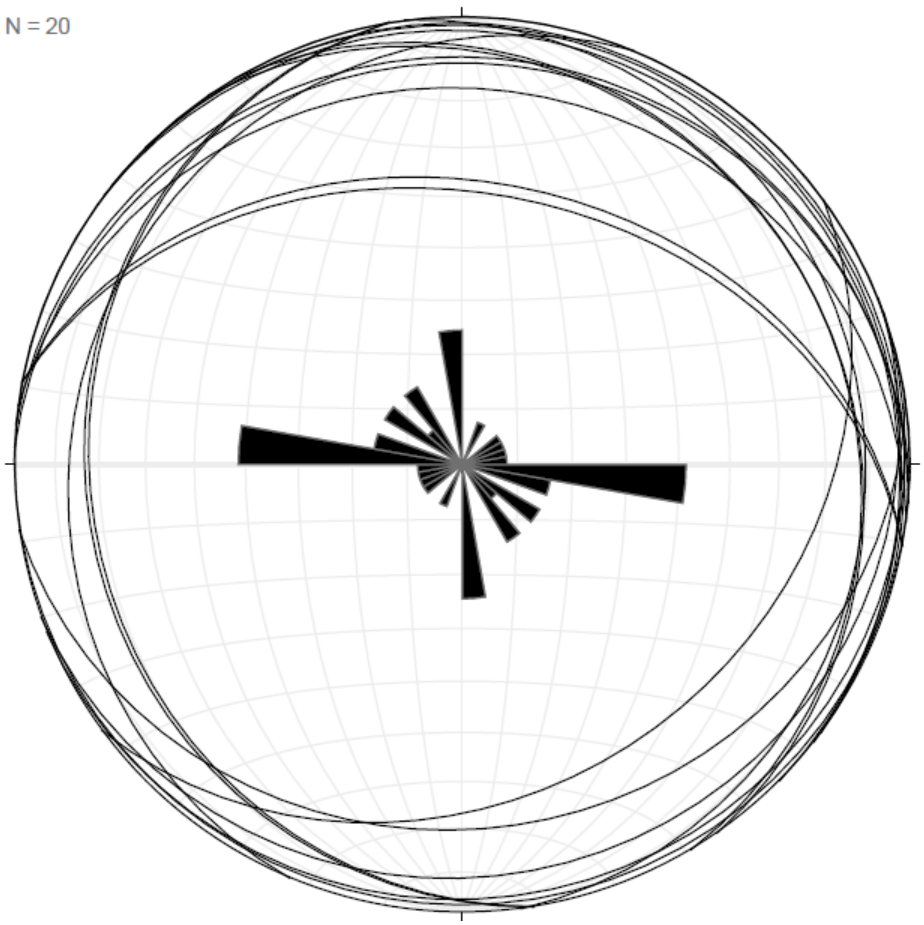

Figure 2.40 *Stereonet plot of dip and strike for all layering measurements in the 200-250 mbs depth bin.*

The distribution of poles for all layering measurements in the 200-250 mbs depth bin (Figure 3.41) is mainly vertical to sub vertical within the central and outer contours with the exception of very few deviating poles that are arranged sub-horizontally.

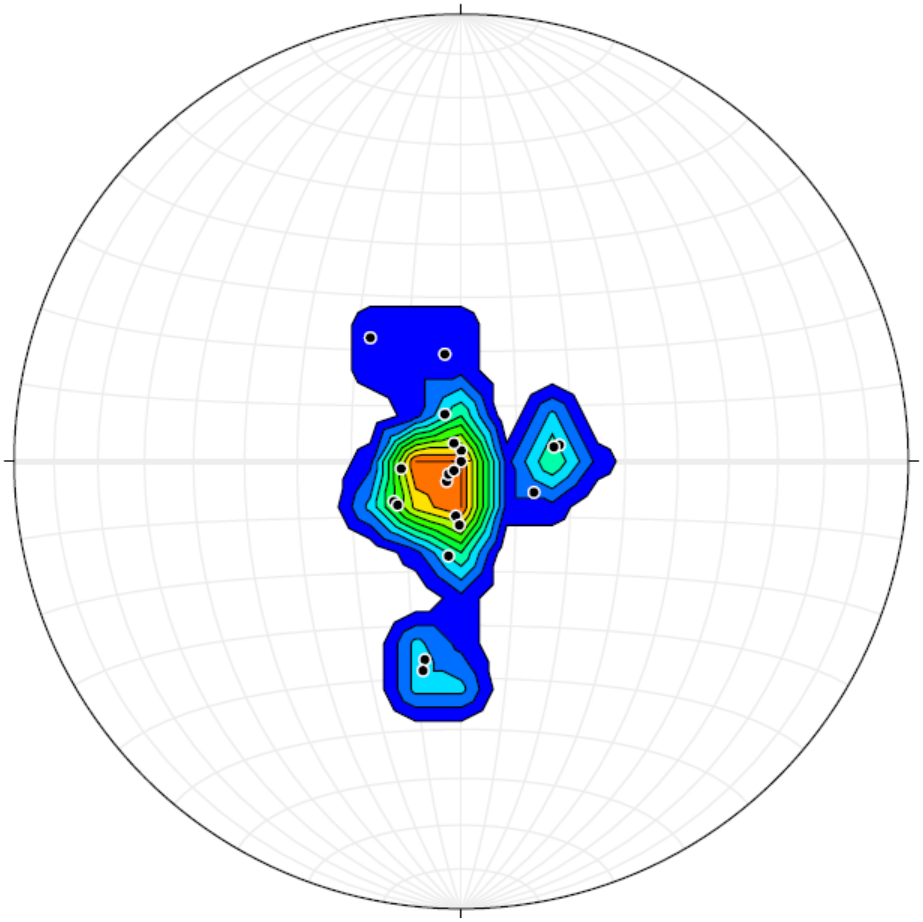

Figure 2.41 *Stereonet plot for all layering measurements in the 200-250 mbs depth bin as poles with 1% area contours in intervals of 3%.*

2.3.3.5 Layering Depth Bin: 250-300 Mbs (17 Measurements)

The Rose diagram and plotted planes for every layering measurement in the 250-300 mbs depth bin (Figure 3.42) exhibit moderate variation in strike direction. The strongest pattern is oriented NW-SE and has an average trend value close to 125. The main subpopulations strike NNW-SSE and NE-SW.

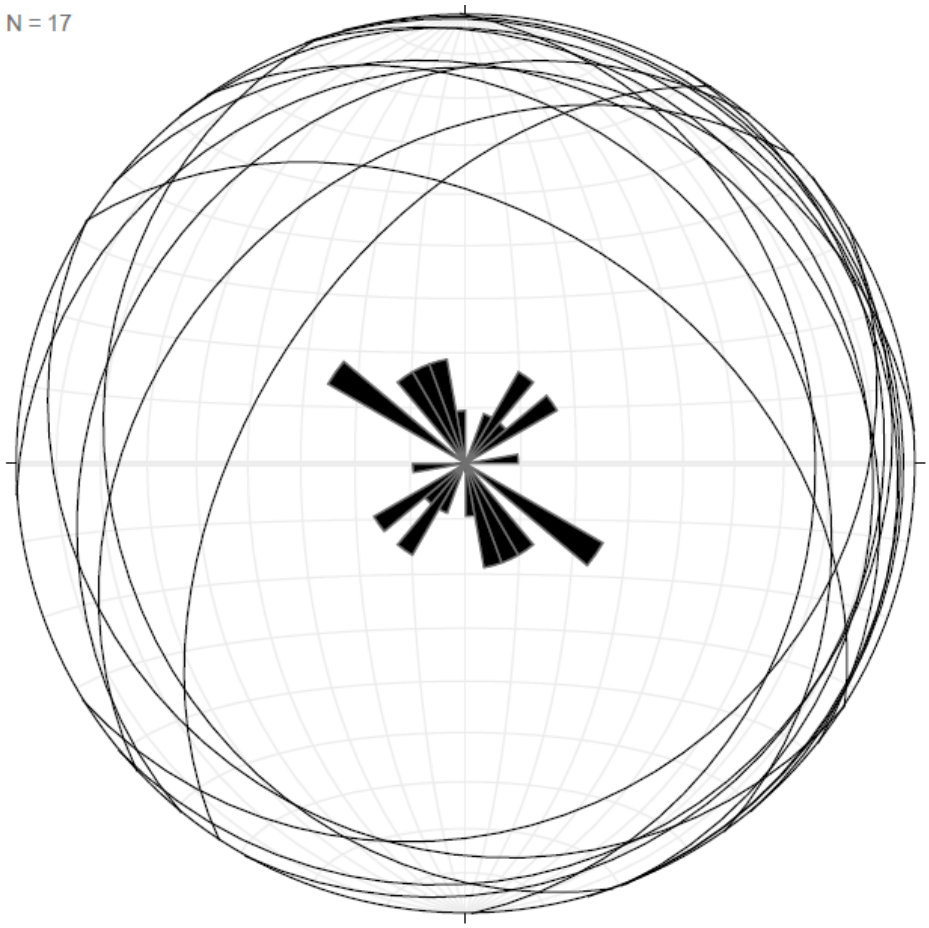

Figure 2.42 *Stereonet plot of dip and strike for all layering measurements in the 250-300 mbs depth bin.*

The distribution of poles for layering measurements in the 250-300 mbs depth bin (Figure 3.43) ranges from sub-vertical in the innermost contours to sub-horizontal in the outer contours as poles begin to spread out laterally away from the center.

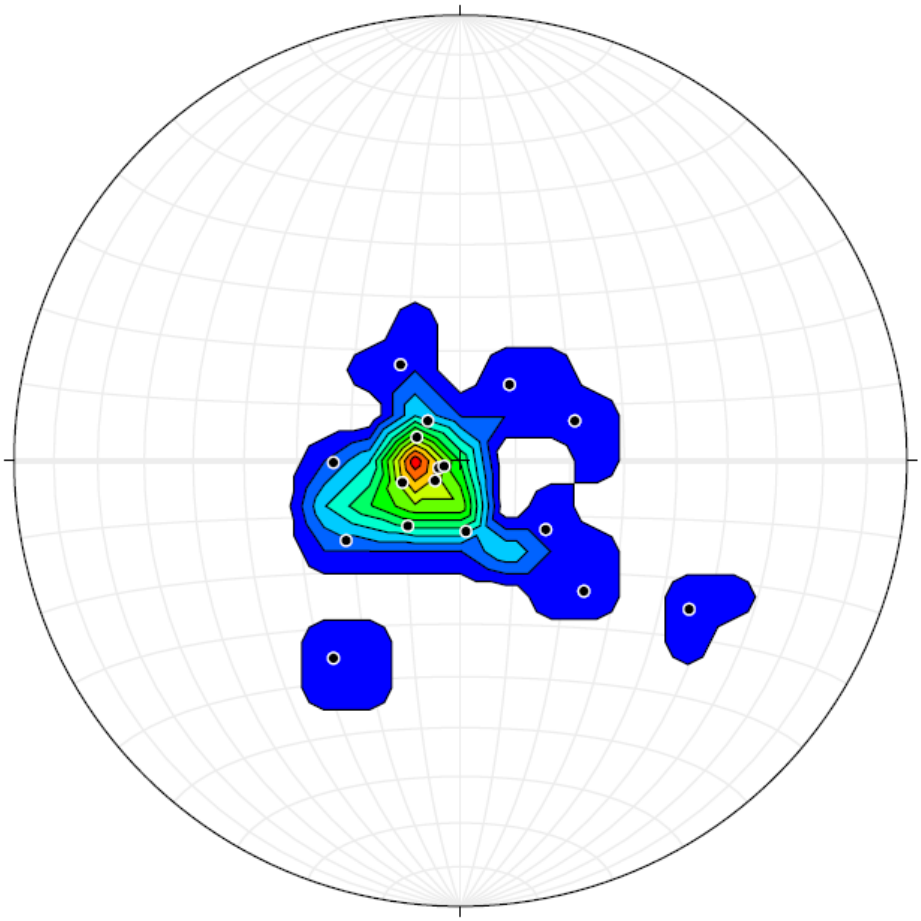

Figure 2.43 *Stereonet plot for all layering measurements in the 250-300 mbs depth bin as poles with 1% area contours in intervals of 3%.*

2.3.3.6 Layering Depth Bin: 300-350 Mbs (19 Measurements)

The stereonet plot for all layering measurements in the 300-350 mbs bin (Figure 3.44) displays consistent variation in strike direction on the Rose diagram. Many patterns strike NE-SW with trend values between 040 and 055 while other patterns are oriented NW-SE with trend values of 090, 116, or 138.

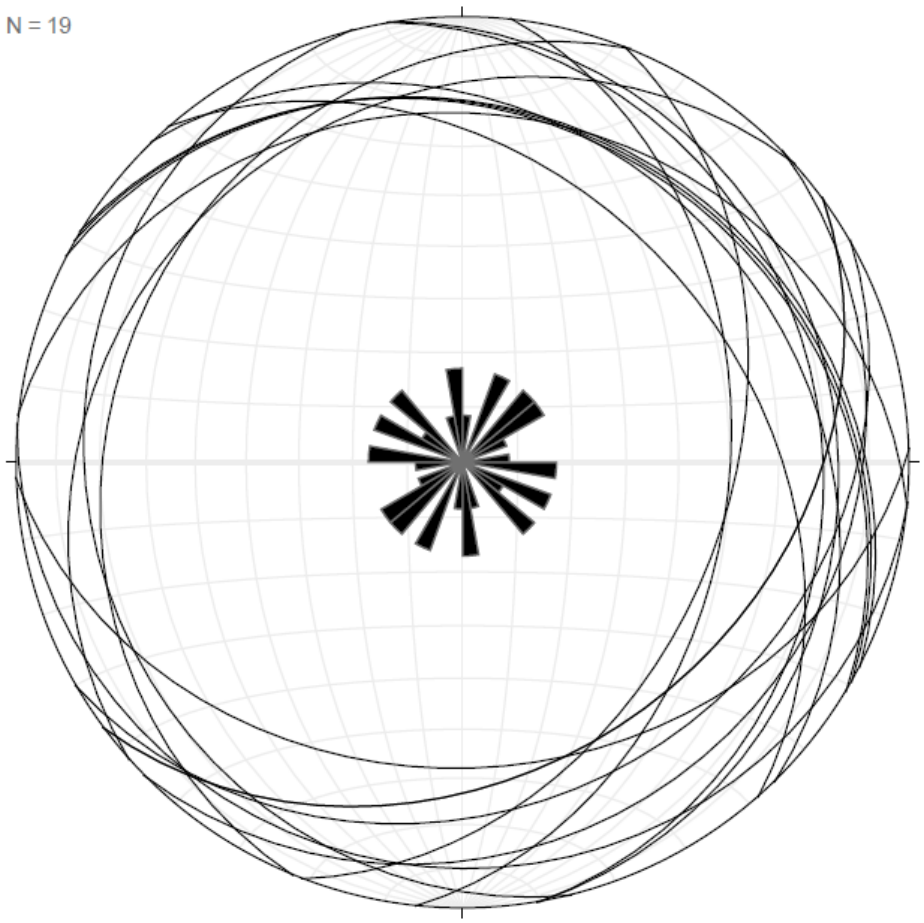

Figure 2.44 *Stereonet plot of dip and strike for all layering measurements in the 300-350 mbs depth bin.*

The pole distribution for layering measurements in the 300-350 mbs depth bin (Figure 3.45) is primarily horizontal to sub-horizontal between the inner and outer contours. While poles within the central contours are more closely clustered, poles in the outer contours are spaced significantly further from one another and typically isolated.

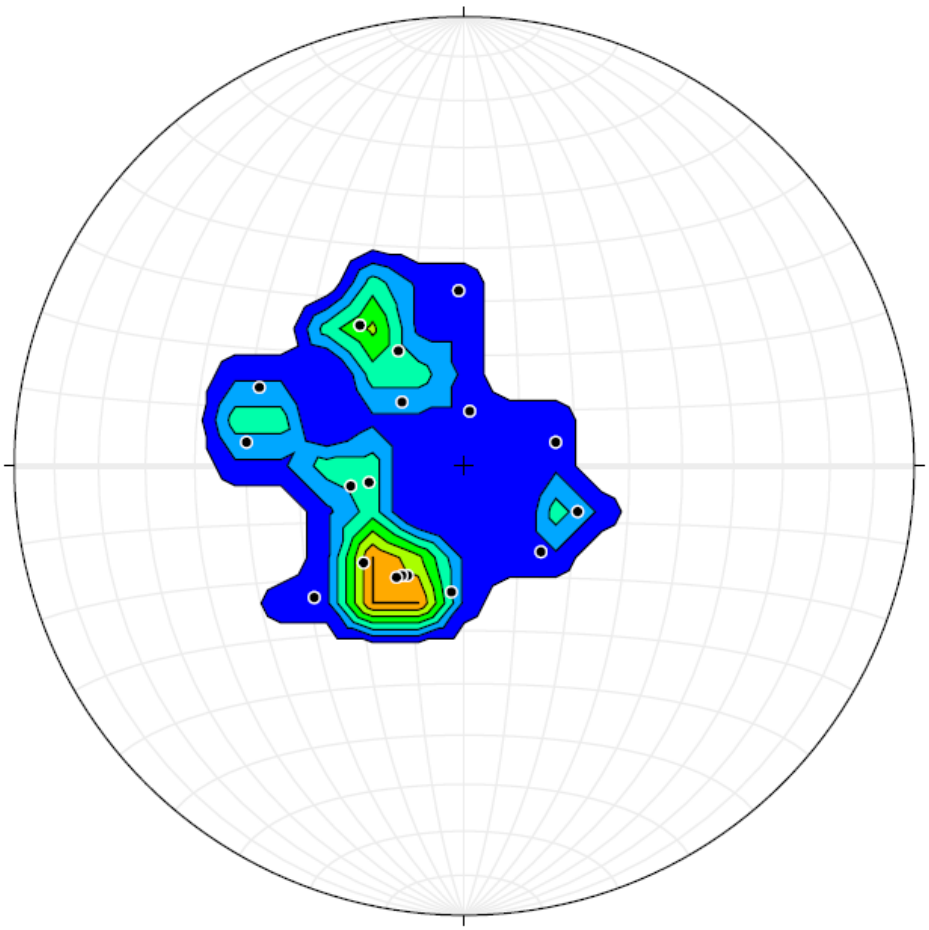

Figure 2.45 *Stereonet plot for all layering measurements in the 300-350 mbs depth bin as poles with 1% area contours in intervals of 3%.*

2.3.3.7 Layering Depth Bin: 350-403 Mbs (16 Measurements)

Two major strike patterns are prevalent in the stereonet plot of planes for layering measurements within the 350-403 mbs bin (Figure 3.46). The highest number of planes share a W to E strike with a trend value close to 090. The second most frequent pattern strikes NNE to SSW with a range of trend values between 000 and 035.

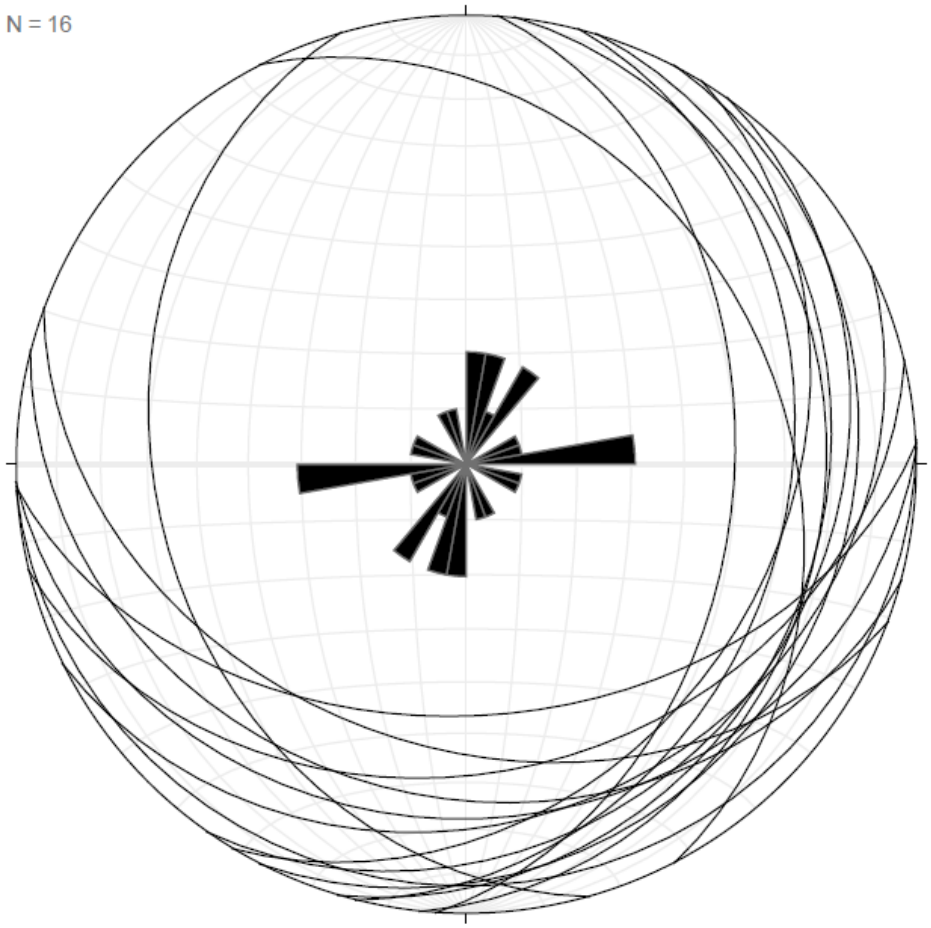

Figure 2.46 *Stereonet plot of dip and strike for all layering measurements in the 350-403 mbs depth bin.*

The pole distribution for layering measurements in the 350-403 mbs depth bin (Figure 3.47) are mainly horizontal to sub horizontal in the central contours and become sub-vertical between the outer contours.

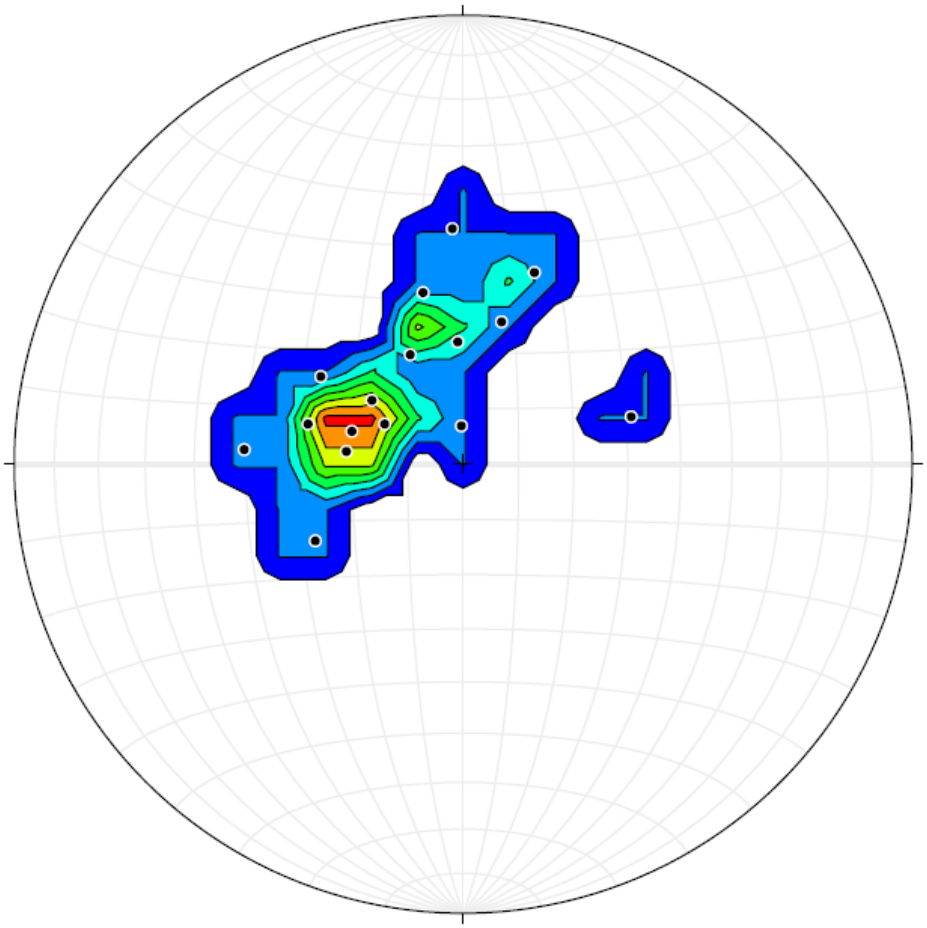

Figure 2.47 *Stereonet plot for all layering measurements in the 350-403 mbs depth bin as poles with 1% area contours in intervals of 3%.*

2.3.4 Depth Bins: All Data

2.3.4.1 All Data Depth Bin: 30-100 Mbs (68 Measurements)

The largest pattern for both layering and magmatic fabrics in the initial 100 mbs of depth in Hole GT1 (Figure 3.48) strikes NNW-SSE with an average strike of roughly 165. The other major pattern present strikes of NE-SW with a strike of 040 and the weakest pattern strikes NW-SE with a strike of 105. The last subpopulation has a strike that is ESE-WNW.

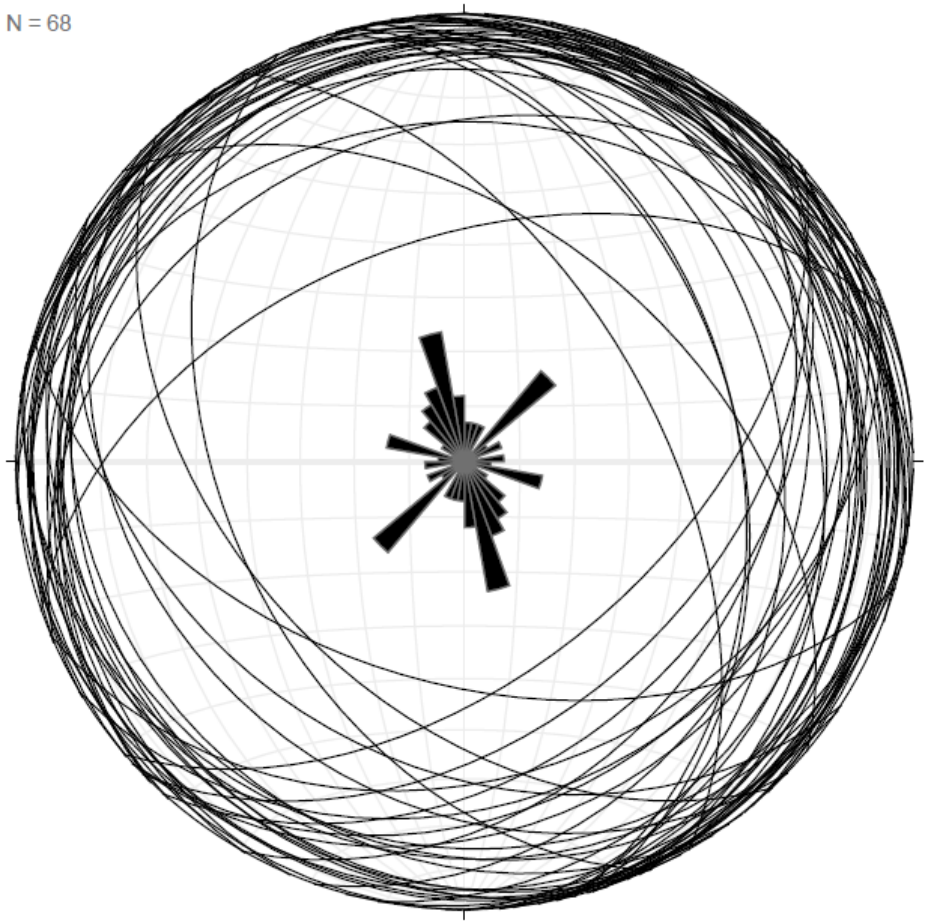

Figure 2.48 *Stereonet plot of dip and strike for the 30-100 mbs depth bin.*

The stereonet plot of poles with contours for the 30-100 mbs depth bin (Fiure 3.49) shows a primarily near horizontal dip. Most poles are spaced relatively close together within the central contour and become slightly more scattered in the outer contours. A girdle-like pattern from ENE to WSW matches the mainly N-S strike and indicates dips are to the NE and SW.

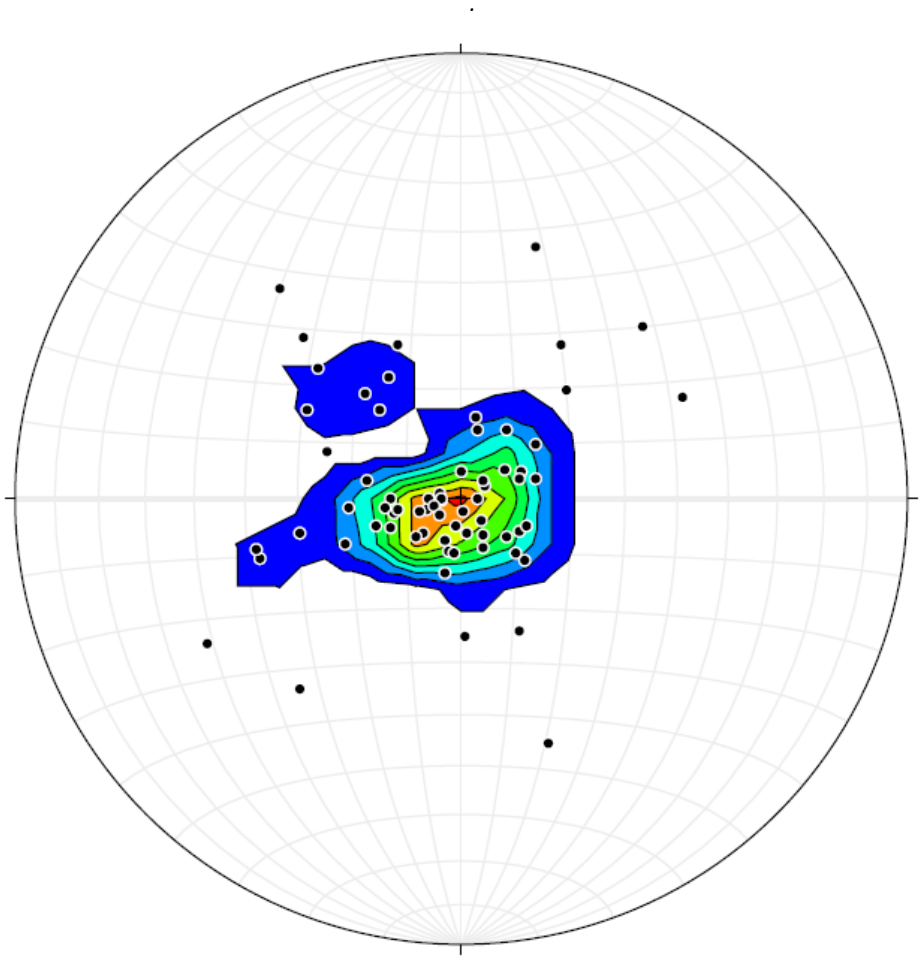

Figure 2.49 *Stereonet plot of the 30-100 mbs depth bin as poles with 1% area contours in intervals of 3%.*

2.3.4.2 All Data Depth Bin: 100-150 Mbs (92 Measurements)

The Rose diagram plot for the 100-150 mbs interval (Figure 3.50) shows that the highest number of dip and strike measurements have a strike close to 105 or 285 while an almost equally large portion of measurements in the bin has a 135 or 314 strike with subpopulations in between. Another subpopulation strikes N-S.

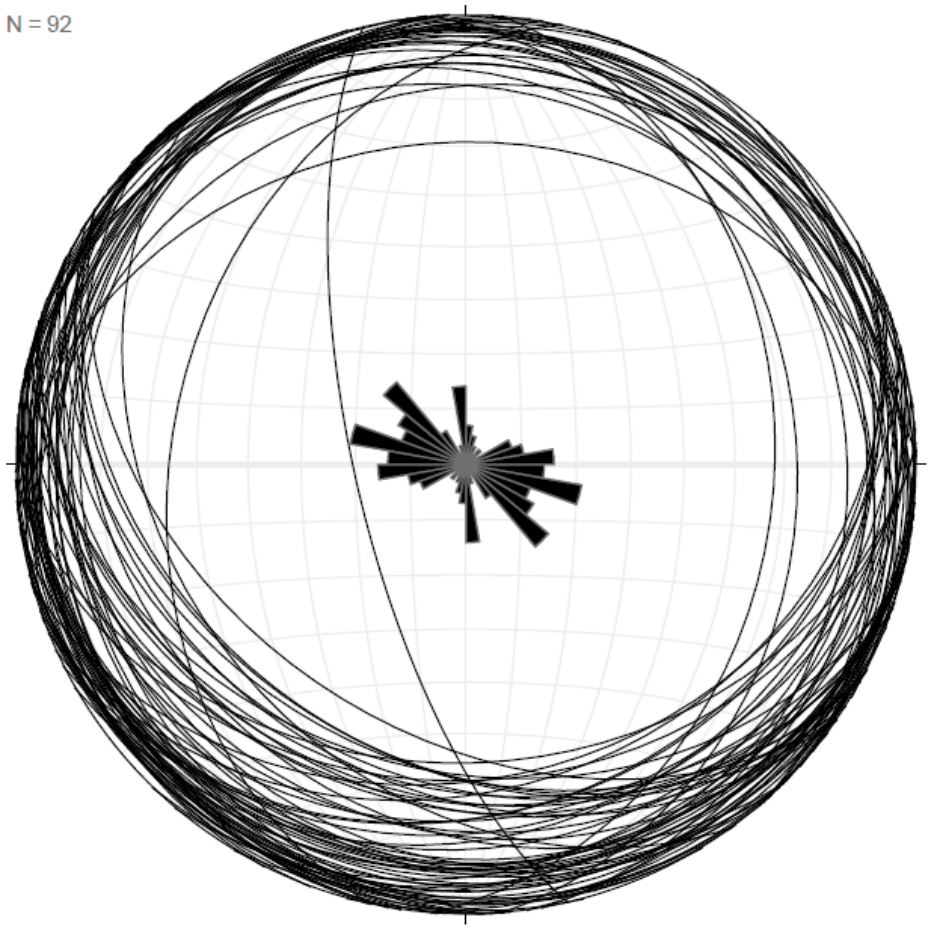

Figure 2.50 *Stereonet plot of dip and strike for the 100-150 mbs depth bin.*

The stereonet plot of poles for all magmatic fabric and layering measurements in the 100-150 mbs bin (Figure 3.51) displays a shallow to sub-horizontal distribution that is densely concentrated in the central contours. A girdle like pattern is evident from NNE to SSW indicating NW-SE strike and dips towards the NNE and SSW.

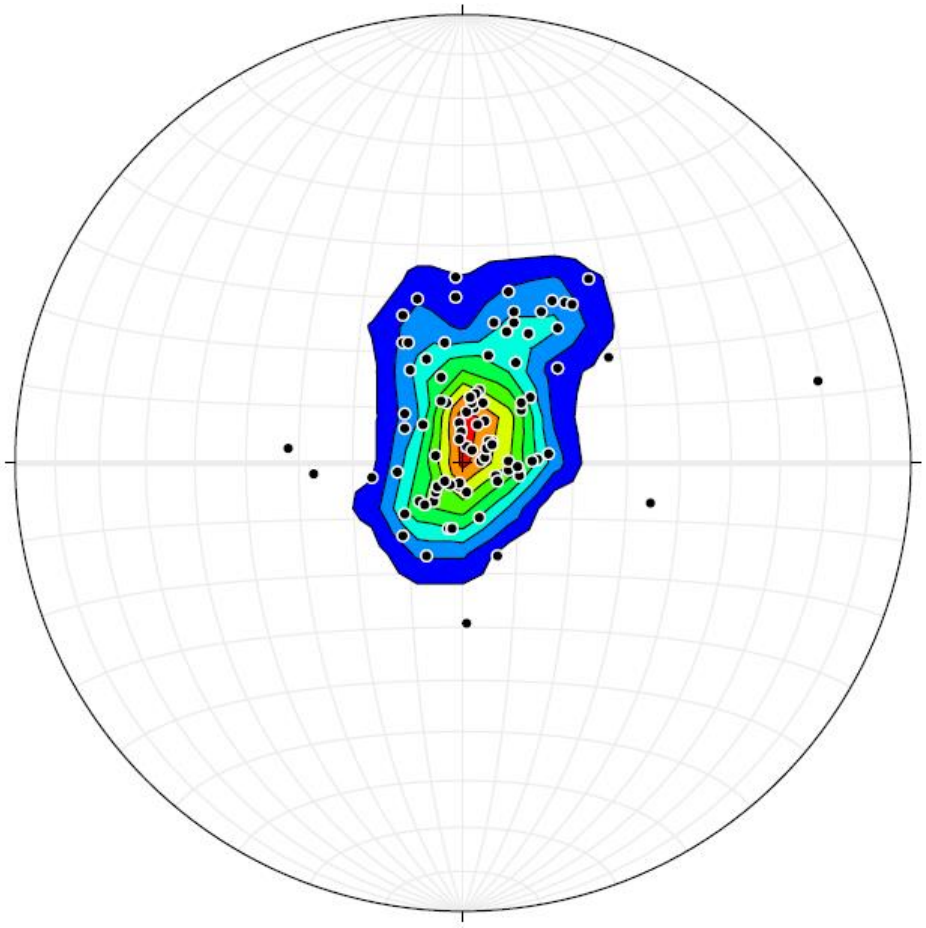

Figure 2.51 *Stereonet plot of the 100-150 mbs depth bin as poles with 1% area contours in intervals of 3%.*

2.3.4.3 All Data Depth Bin: 150-200 Mbs (76 Measurements)

The stereonet plot of polls and respective Rose diagram for all measurements within the 150-200 mbs depth bin (Figure 3.52) show a high amount of variation in strike direction. The largest number of planes strike NE-SW with a trend of 065. One pattern of note differs from the others as it strikes NW-SE with a general trend of 135 or 315. Other subpopulations include strikes toward N-S and E-W.

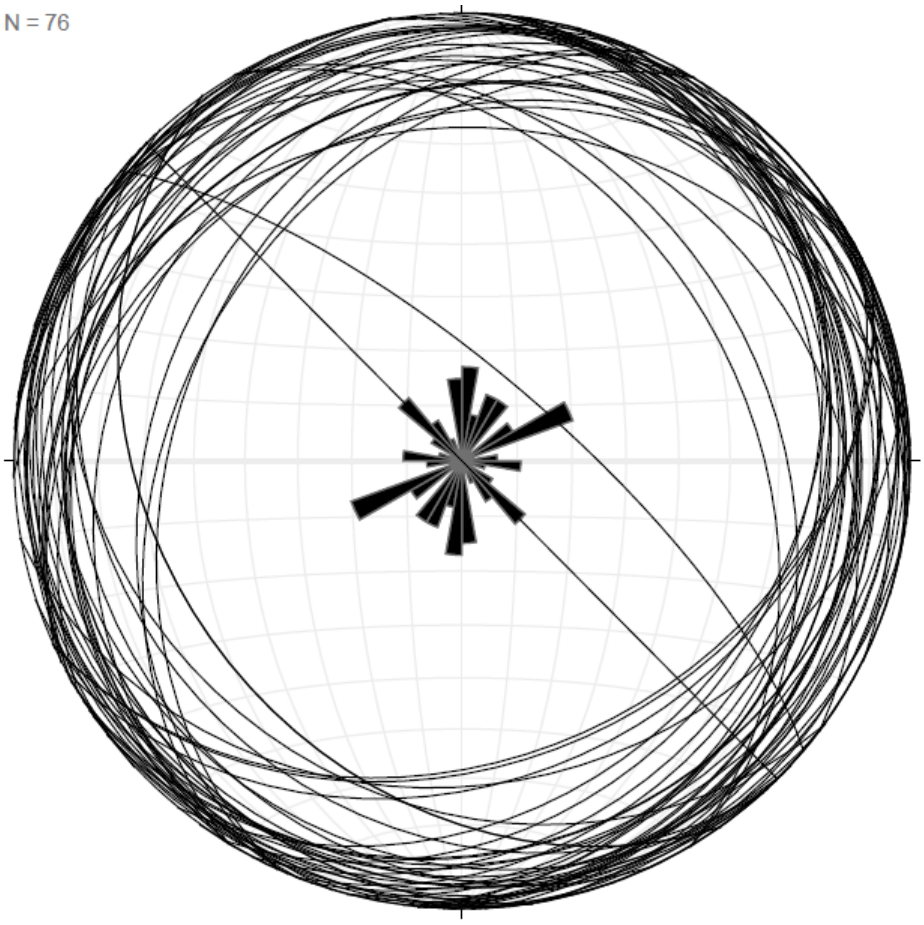

Figure 2.52 *Stereonet plot of dip and strike for the 150-200 mbs depth bin.*

The distribution of poles for all measurements within the 150-200 mbs depth bin (Figure 3.53) is mainly horizontal to sub-horizontal within the central contours.

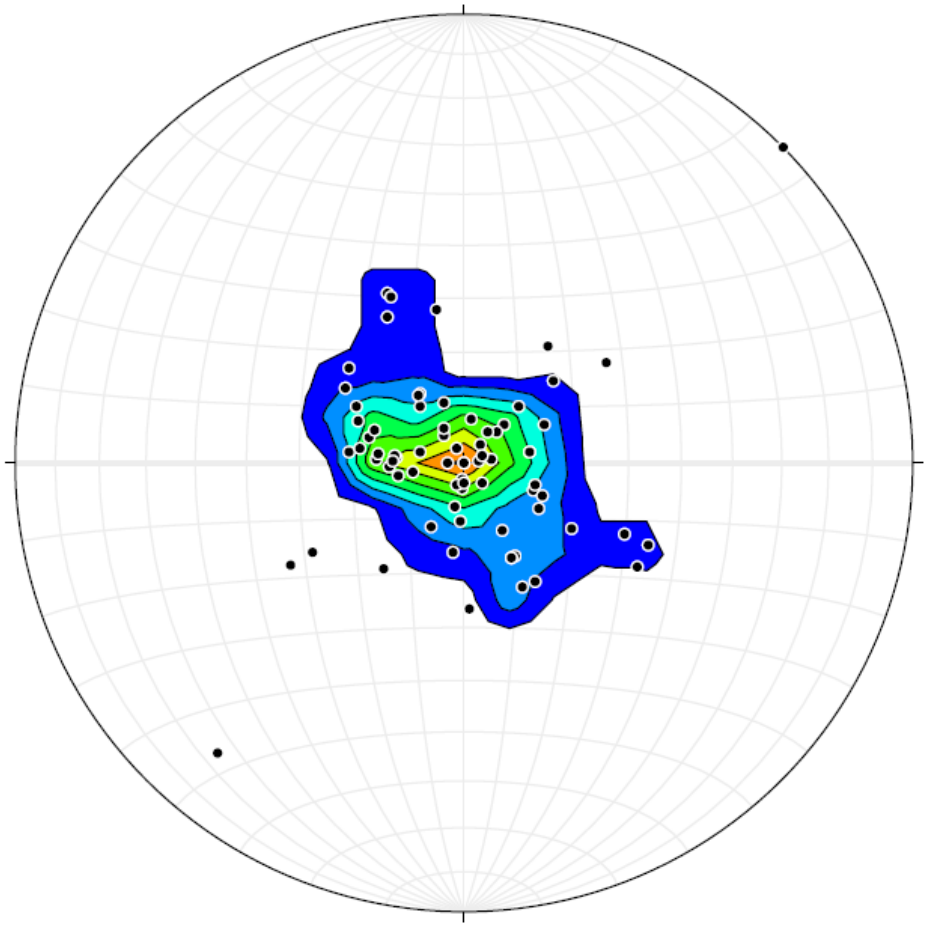

Figure 2.53 *Stereonet plot of the 150-200 mbs depth bin as poles with 1% area contours in intervals of 3%.*

2.3.4.4 All Data Depth Bin: 200-250 Mbs (49 Measurements)

The vast majority of dip and strike measurements within the 200-250 mbs bin share an ESE-WNW orientation with a trend of 094 or 275 (Figure 3.54). There are also subpopulations that strike NNW-SSE, ENE-WSW, and E-W.

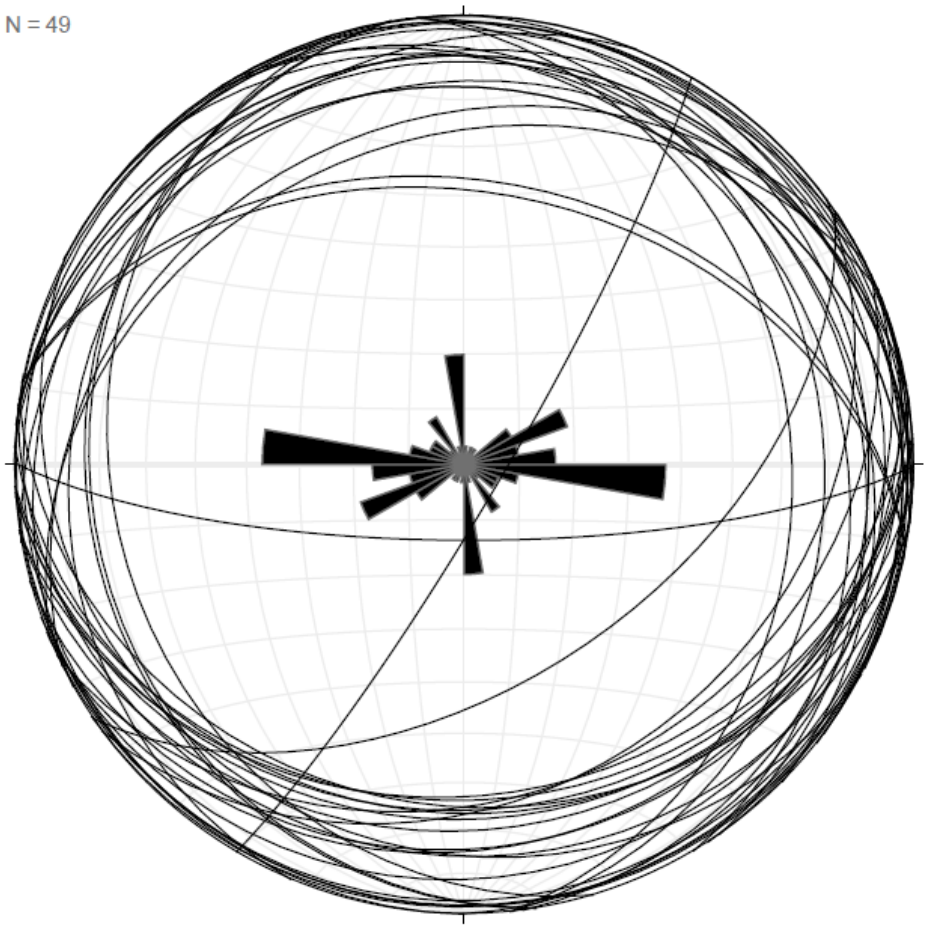

Figure 2.54 *Stereonet plot of dip and strike for the 200-250 mbs depth bin.*

The distribution of poles for all layering and magmatic fabrics in the 200-250 mbs depth bin (Figure 3.55) displays a sub-horizontal arrangement strongly clustered poles within the innermost contours. Girdle patterns indicates strikes are mainly E-W and dips are N and S.

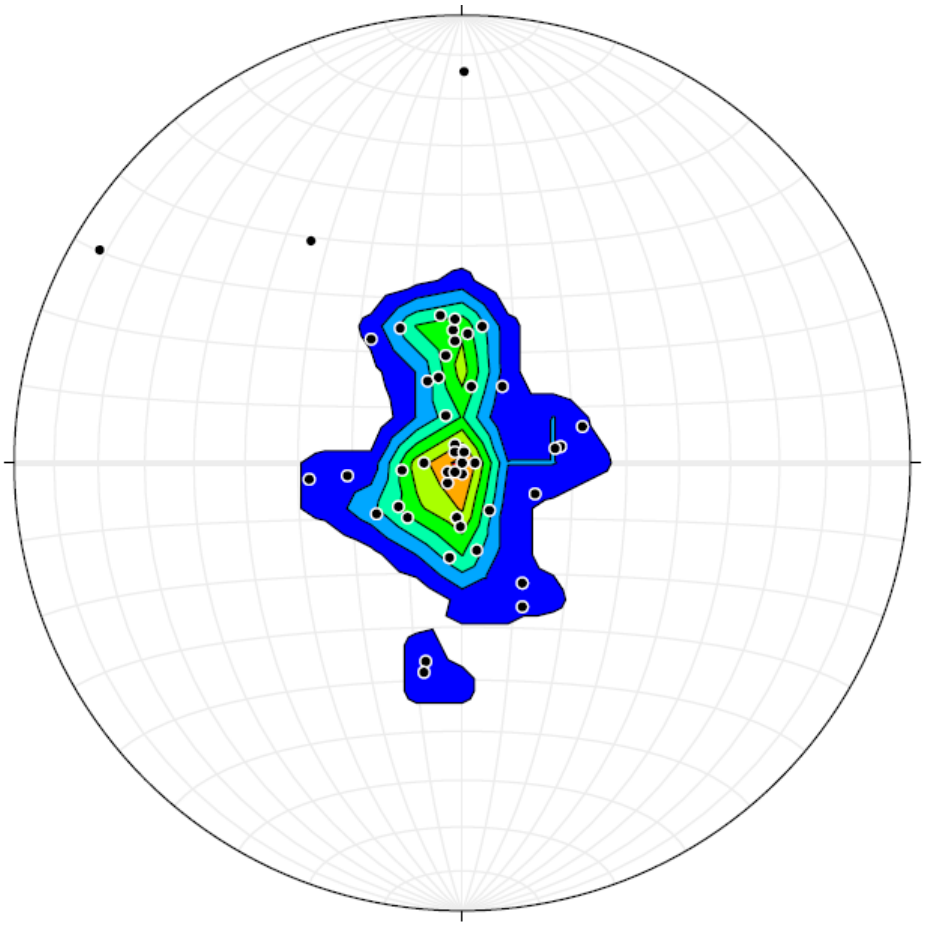

Figure 2.55 *Stereonet plot of the 200-250 mbs depth bin as poles with 1% area contours in intervals of 3%.*

2.3.4.5 All Data Depth Bin: 250-300 Mbs (28 Measurements)

The stereonet plot for all magmatic fabric and layering measurements within the 250-300 mbs depth bin (Figure 3.56) exhibits significant variance in strike direction. The majority of planes fall within two patterns that strike NE-SW with a trend of either 032 or 053. Most other patterns strike NW-SE with differing trend values between 120 and 170.

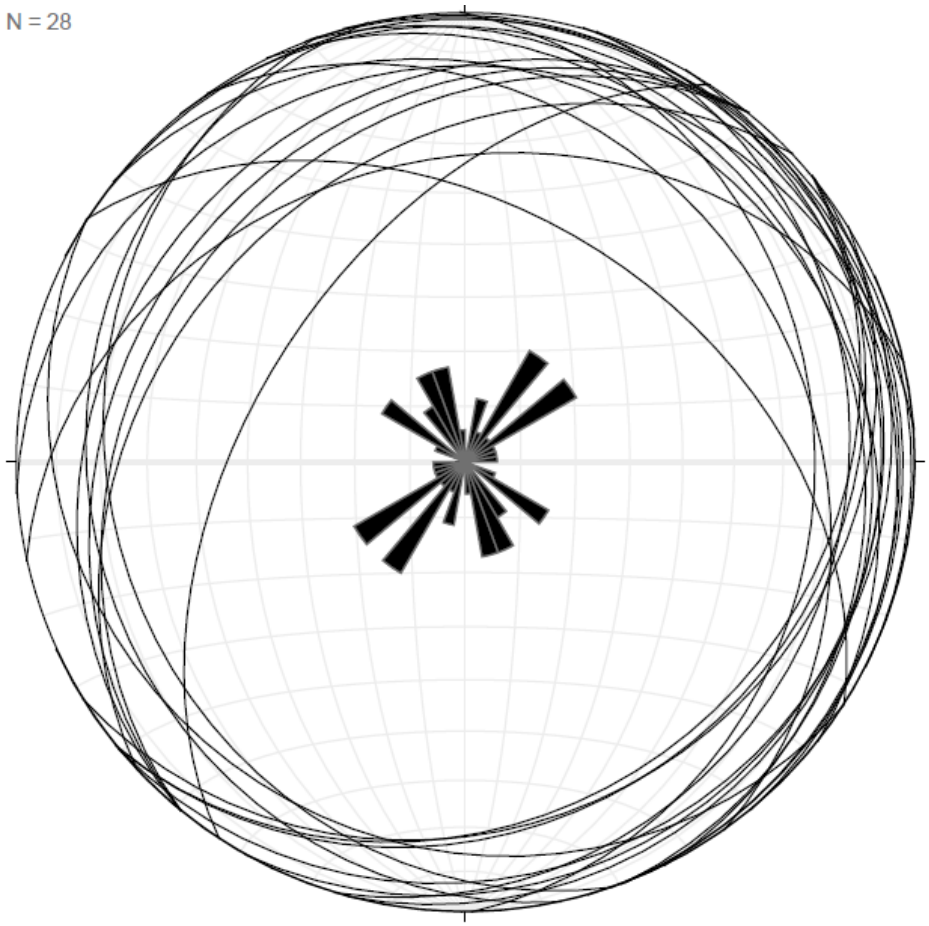

Figure 2.56 *Stereonet plot of dip and strike for the 250-300 mbs depth bin.*

The distribution of poles for all measurements within the 250-300 mbs bin stereonet (Figure 3.57) is sparsely scattered and can be either vertical or sub-horizontal between the central contours. Poles in the outer contours are typically isolated with the exception of moderately spaced clusters.

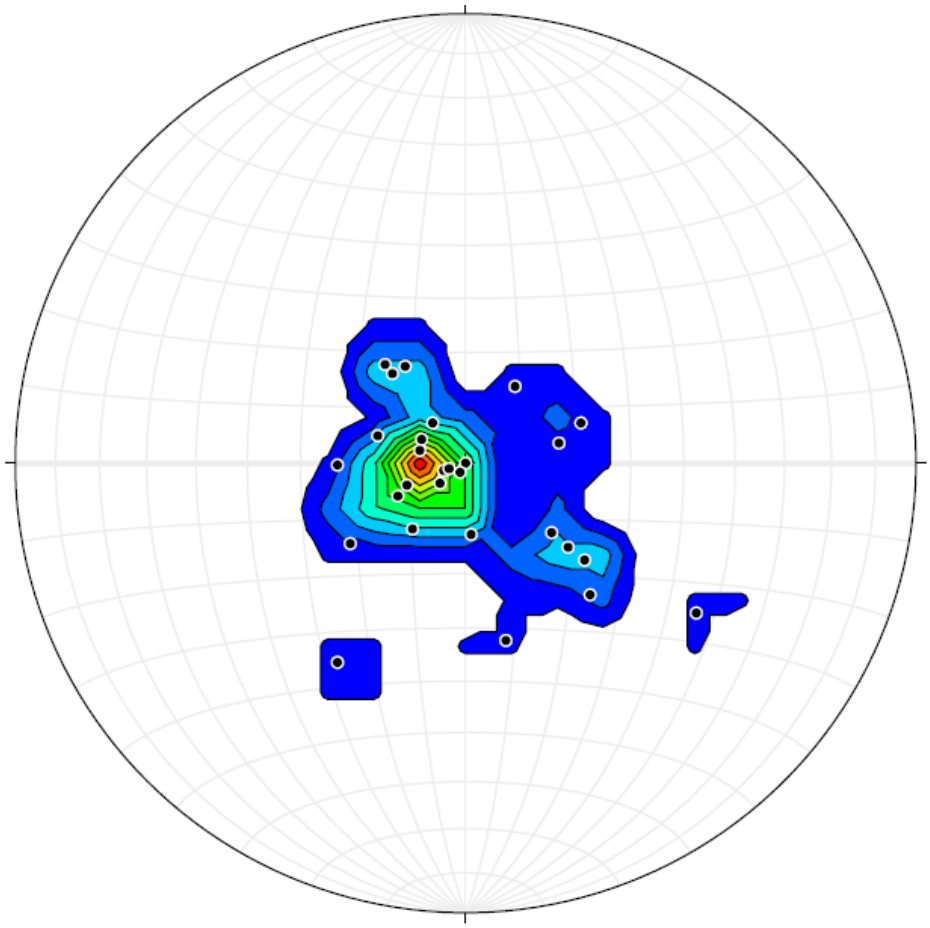

Figure 2.57 *Stereonet plot of the 250-300 mbs depth bin as poles with 1% area contours in intervals of 3%.*

2.3.4.6 All Data Depth Bin: 300-350 Mbs (33 Measurements)

The stereonet plot of planes for all magmatic fabric and layering measurements in the 300-350 mbs bin (Figure 3.58) shows that while strike direction is highly varied, the majority of planes strike E-W with a trend of 094. Another strong pattern strikes NE-SW with trend values between 048 and 067.

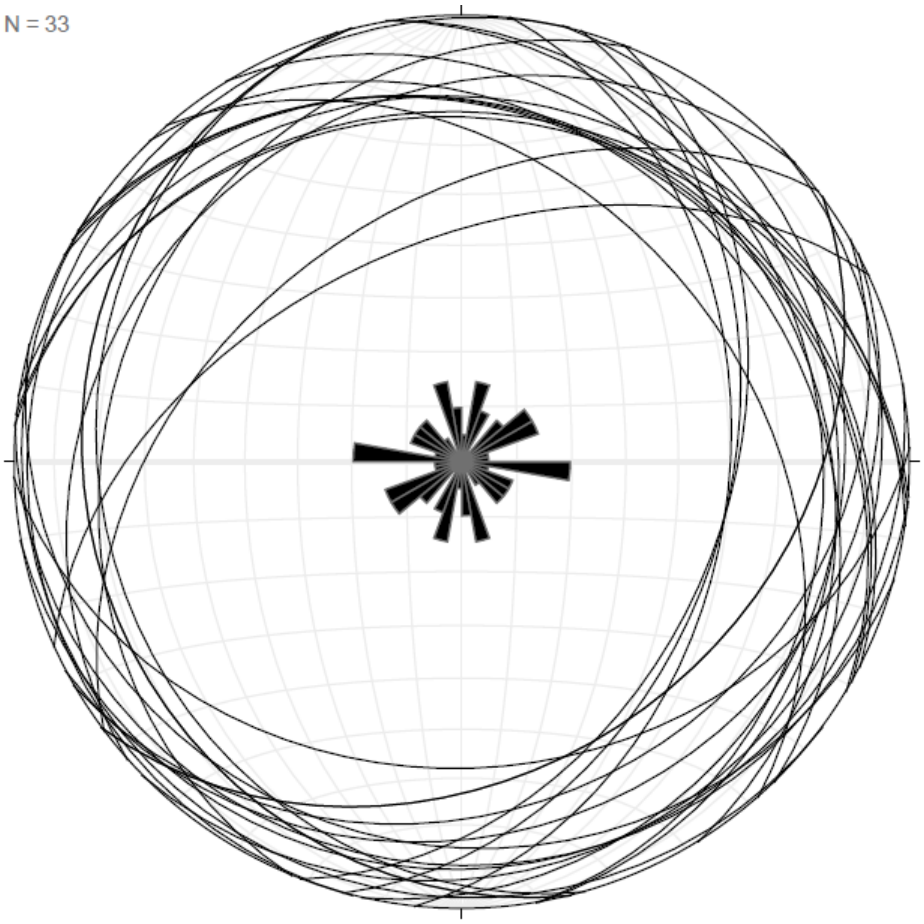

Figure 2.58 *Stereonet plot of dip and strike for the 300-350 mbs depth bin.*

The distribution of poles for all data within the 300-350 mbs depth bin (Figure 3.59) is generally horizontal to sub-horizontal in the central contours and sub vertical in the outer contours.

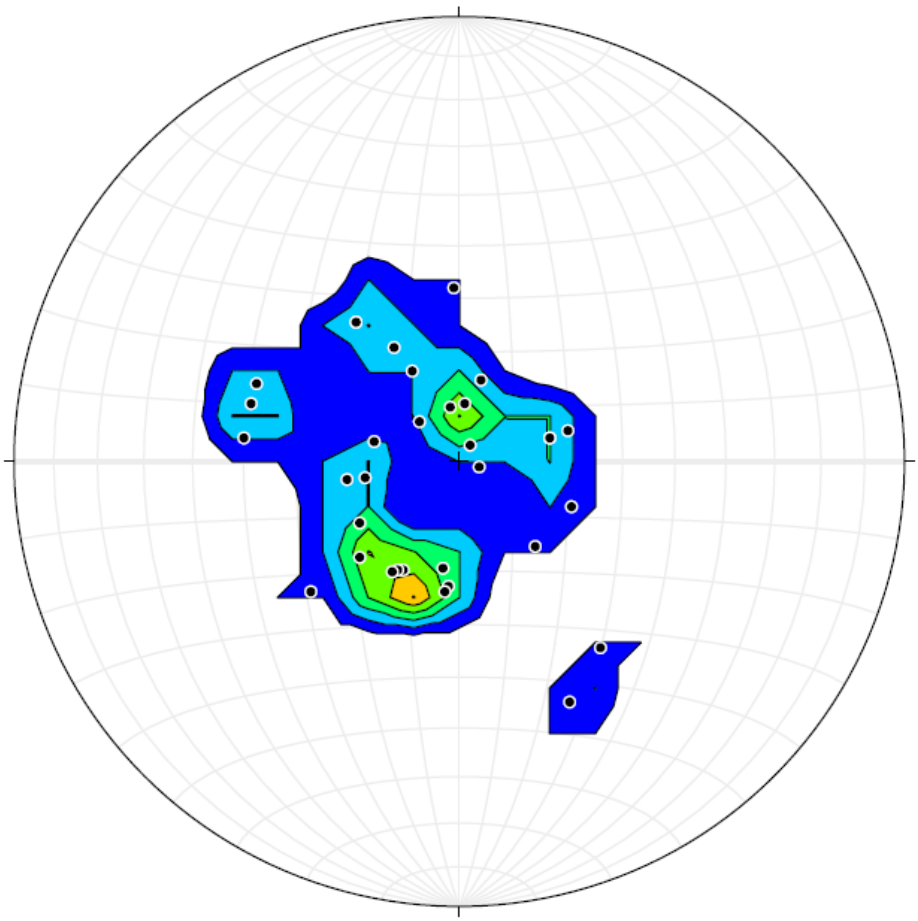

Figure 2.59 *Stereonet plot of the 300-350 mbs depth bin as poles with 1% area contours in intervals of 3%.*

2.3.4.7 All Data Depth Bin: 350-403 Mbs (49 Measurements)

The stereonet plane plot for all data in the 350-403 mbs bin (Figure 3.60) strikes primarily NE-SW with a broad range of trend values between 030 and 067. Another sizeable portion of planes strike NW-SE with and average trend of 160.

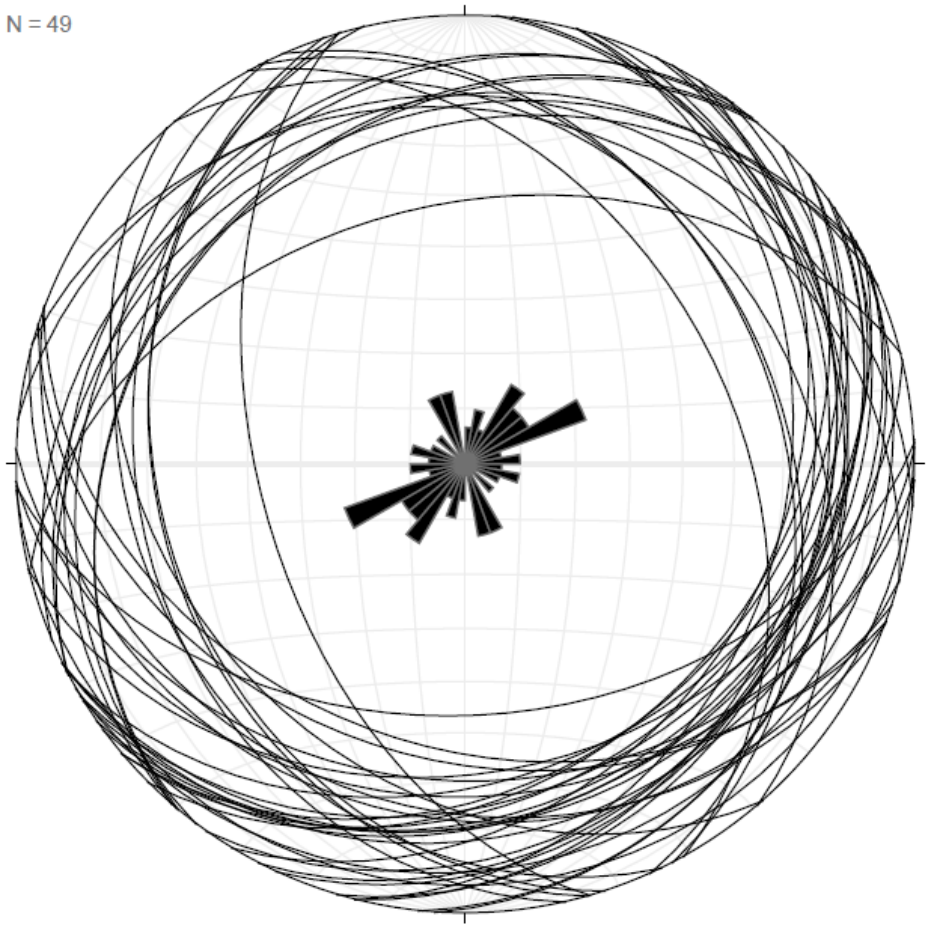

Figure 2.60 *Stereonet plot of dip and strike for the 350-403 mbs depth bin.*

The distribution of poles for all magmatic fabric and layering measurements in the 350-403 mbs bin (Figure 3.61) is vertical to sub vertical in the innermost contours and sub vertical to sub horizontal between the outer contours.

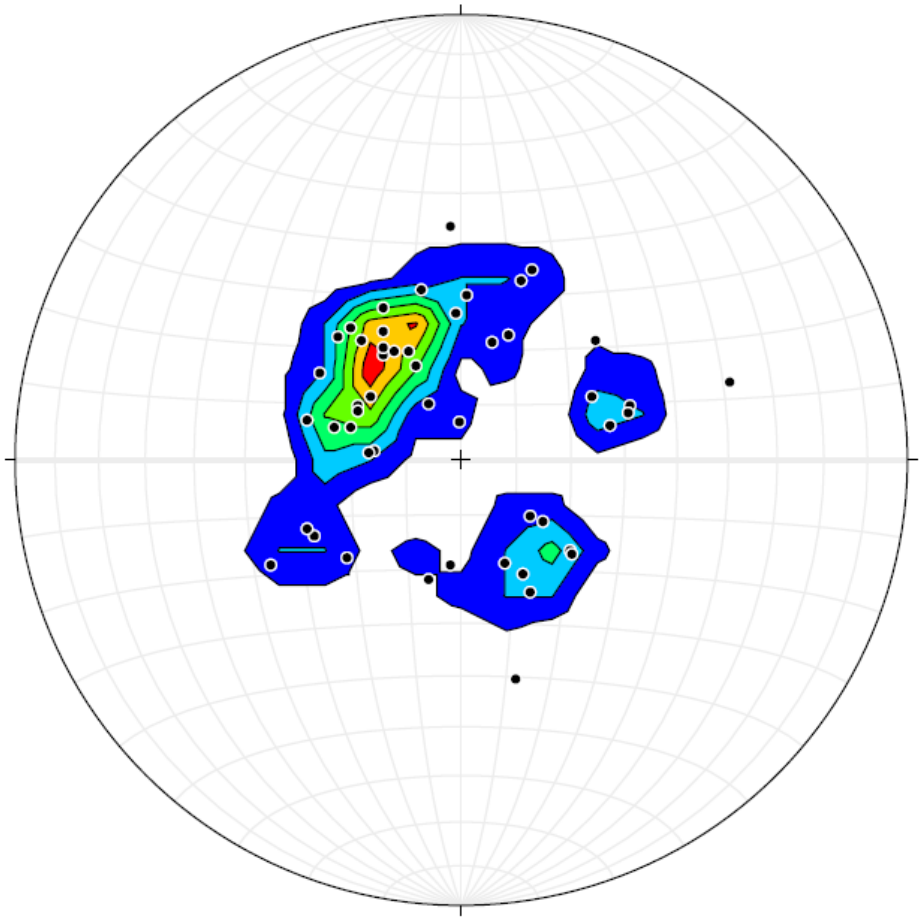

Figure 2.61 *Stereonet plot of the 350-403 mbs depth bin as poles with 1% area contours in intervals of 3%.*

– DISCUSSION

The results discussed above illustrate the downhole variety in orientation and intensity for magmatic fabrics and layering. Systematic changes in orientation with depth take place within distinct intervals where strike direction tends to shift from E-W to N-S. The following section will take these observations into account in an effort to pinpoint geological processes that are likely to form magmatic foliations and layering in the Wadi Tayin massif and discuss how those processes apply to the Oman Ophiolite as a whole and fast spreading ridges. Understanding how the observed patterns can be linked to flow direction above the mantle may provide details necessary for further developing an accurate model of lower crustal accretion.

3.1 Magmatic Fabric vs. Layering Orientation

When comparing the histogram plots for layering and magmatic fabrics, it appears that while the occurrence of both types of measurements is relatively similar throughout the borehole, there are key areas of contrast between the two at specific depth intervals. Layering is substantially more frequent in the initial 50 meters of depth while magmatic fabrics are scarce and sparsely distributed before becoming more abundant past 100 mbs. The difference in frequency between magmatic fabrics and layering can be best observed at 150 mbs, where they both reach their respective peaks in the number of measurements within a single depth bin. The number of magmatic fabrics reaches a total of almost 40 measurements by 150 mbs while the number of layering rises past 90 measurements. After peaking at 49 measurements for the 200-250 mbs depth bin, the frequency of magmatic fabrics lowers to around 28 in the 250-300 mbs depth bin and remains close to 20 measurements past 350 mbs. Instances of layering, however, diminish significantly

between 200 mbs and 250 mbs as the frequency of measurements decreases from 80 to 50 and continues falling. In the 400 mbs depth bin the frequency of magmatic fabrics remains significantly higher than that of layering while also having a substantial increase of magmatic fabrics beyond the 350 mbs threshold relative to previous depth bins. Some reasons for this could be that magmatic fabrics only require small increments of strain to form and can do so with less than 20% melt through grain alignment and contact melting (Nicolas, 1992; Nicolas and Ildefonse, 1996; Paterson et al., 2018) whereas internal contacts and layering can be erased through homogenization within a magma chamber, re-working in response to metamorphism or deformation, and the introduction of a newly arriving magma pulse (Paterson et al., 2018). Another possibility is that layering becomes more variable downhole in response to intermittent convection in the magma chamber, during which changes in convection velocity can cause layers to deposit rhythmically (Mock et al., 2020). This would also result in anorthosite layers forming near the top of the magma reservoir. Anorthosites were present in GT1, but not in regular intervals and not along obvious contacts with distinct magma bodies (Kelemen et al., 2020). In general, magmatic fabrics and layering do not appear to be distributed equally down hole and there is no apparent increase in their intensity with depth (Kelemen et al., 2020). The variability with depth throughout the core could imply that the processes driving the formation of magmatic fabrics and layering may not occur systematically throughout the crust.

3.2 Orientation Variations with Depth

The reoriented dip azimuth vs. depth plot for magmatic fabrics shows a varied range in dip azimuth values that is relatively more uniform at particular depth intervals.

This change can be observed where the orientation of dip azimuth changes from NW to SW between 100 and 150 mbs and then from SW-SE back to NW between 200 and 250 mbs. The consistency in dip azimuth between 200 and 250 mbs with relatively little shift resembles magmatic fabric orientations predicted by the Gabbro Glacier model (VanTongeren et al., 2015; Quick and Denlinger, 1993; MacLeod and Yaouancq, 2000; Morgan and Chen, 1993; Ben and Allard, 1989) while the greater variety in dip azimuth measurements seen throughout most of the depth plot resembles a more dynamic flow direction that would be expected to form according to the Sheeted Sills model (Amri et al., 1996; Boudier et al., 1996; Kelemen et al., 1997; Korenaga and Kelemen, 1997; Henstock et al, 1993).

The depth plot for layering in Hole GT1 includes a high amount of variability between data points with the exception of a significantly larger number of SW oriented dip azimuth measurements present at 100 mbs compared to the magmatic fabrics depth plot. A shift in orientation from NE to SW past 300 mbs is present in the depth plots for magmatic fabrics, layering, and high confidence measurements. This shift is less pronounced in the layering plot, however, which retains a N-S orientation for the 100-150 mbs and 250-300 mbs depth intervals, whereas the change to an E-W orientation is more consistent in the other three plots at similar depths.

There are several such instances in Hole GT1 where either magmatic fabric or layering measurements that share the same orientation begin to peak in frequency throughout their respective depth bins. Reasons for why the magmatic fabric orientation might change could be an alteration in the direction of magmatic flow, changes to the alignment of deformed crystals in the melt similar to how minerals rotate in response to

stress during porous flow (Paterson et al., 1998), or the forming of a fault on or near axis during obduction that causes the fabrics to be rotated.

The stereonet plots observed in this study indicate that magmatic fabrics in layered gabbros beneath Wadi Tayin most often strike ENE-WSW. This orientation is similar to recent findings from layered gabbros in the southern Samail and Ibra massifs of the Oman ophiolites that describe the common orientation of magmatic fabrics as sub-horizontal with a ENE-WSW trend (Morris et al., 2019). The stereonet plot of poles for all dip azimuth measurements associated with magmatic fabrics in Hole GT1 also exhibit a sub-horizontal orientation. There are also rare cases of steep to nearly vertical dip azimuth orientations but this could simply be the result of later faulting. The stereonet plots for layering differ from the magmatic fabric plots in regard to both pole distribution and the frequency of plane direction for dip azimuth measurements. In contrast to the NE-SW orientation shared by the majority of magmatic fabric measurements, the largest population of dip azimuth measurements for layering is oriented N-S while two equally small populations of E-W and NW-SE oriented measurements are also present (Figure 4.1). The stereonet plot for layering instead has strikes similar to the spreading axis orientation, which has a strike of 009^{o} (Nicolas and Boudier, 2015). Additionally, both the layering and magmatic fabric stereonets exhibit orientation patterns that could be explained by the relationship between the spreading axis and fabrics exposed to shearing within the strain field associated with flow of the mantle. Several studies infer that flow direction of the mantle causes extension in the lower crust due to the estimated mantle flow being faster than the ridge spreading rate (Jousselin et al., 2012), which results in the pulling of the lower crust by the mantle to produce simple shear deformation. If true, then

the lower layered gabbros should have N-S oriented strikes and either E or W oriented dips compared to the spreading axis.

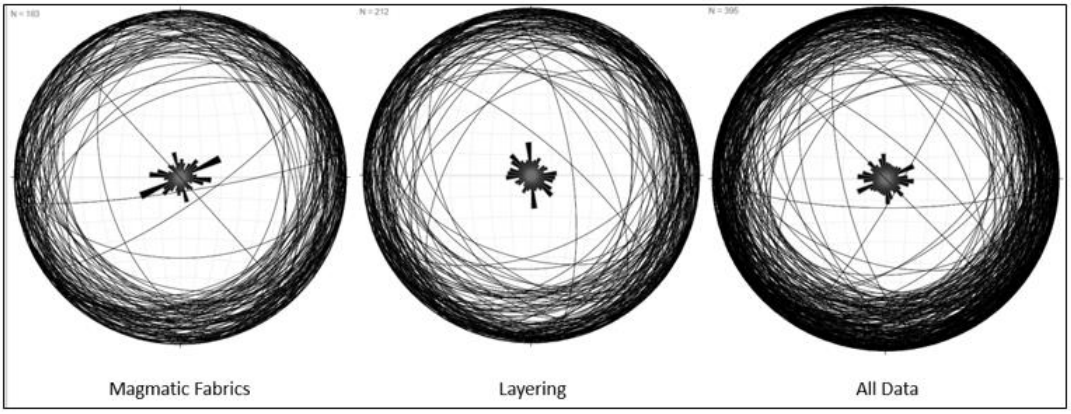

Figure 3.1 *Side by side comparison of stereonets and respective Rose diagrams for magmatic fabrics, layering, and all data.*

The rose diagram is plotting average strikes and dips of 062 and 75 NE-SW for the MF plot, 355 and 75 N-S for the layering plot, and 070 and 80 ENE-WSW for the plot of all data.

When observed in a 2-D model using 2-D extension, the dip direction of magmatic fabrics would presumably be perpendicular relative to the spreading axis and contain shallow dips while the strike would be parallel. The stereonets for magmatic fabrics in this study support that idea by presenting many NE-SW strike measurements that share a sub horizontal orientation with average dip azimuths between 120 and 150 while a significant proportion of layering measurements are consistently vertical and oriented N-S below 150 mbs. Although this is not true for shifts in orientation where fabrics dip more steeply such as the 200-250 mbs depth bin, the influence of extension could explain why many fabric and layering measurements are aligned perpendicular to the spreading axis.

3.3 Formation of Magmatic Fabrics and Layering

Given the general variability in orientation between dip azimuth measurements present in the stereonet and depth plots, the magmatic fabric and layering structures in Hole GT1 likely reflect many different processes varying from large scale regional deformation to internal processes related to flow direction as melt crystallizes within the magma chamber. Assuming that comparisons between orientation of the spreading axis and magmatic fabric measurements are plausible, extension of the lower crust is one example of regional deformation with the potential to shape layered gabbros in Wadi Tayin. Internal processes can form magmatic structures in a variety of ways, however, and often act simultaneously for a given fabric. Processes known to form most types of layering in plutons include fractionation, crystal-melt segregation, deformational strain, and by the intrusion of either new magmas or late, local melts that form internal contacts and mixing zones (Paterson et al, 2018; Mock et al, 2020) while magmatic fabrics can form through additional framework processes such as filter pressing, grain settling, ballooning, and general magmatic flow (Paterson et al, 1988; Nicolas et al, 1988). Filter pressing is a style of deformation that can propel melt through a combination of crystal boundary sliding and either crystal plastic deformation or contact melting depending on whether the strain rate is high or low respectively (Park and Means, 1996; Nicolas and Ildefonse, 1996) and the processes associated with filter pressing can thus apply to the formation of magmatic fabrics assuming that enough melt is present. Other possible avenues by which the orientation of magmatic fabrics can form include the flow of

magma during intrusions, parallel rotation of mineral grains relative to laminar flow (Ben and Allard 1988), crystal alignment during the inflation of sills, and the compression of melt beneath overlying rock formations. Alternatively, the processes responsible for layering could have been more active or widespread for certain areas of the lower crust than the processes that formed magmatic fabrics seeing as how layering measurements are more prevalent throughout Hole GT1 overall.

3.4 Comparisons to Models of Crustal Accretion

Because the sills described by the Sheeted Sills model would have originated from concentrated pools of melt brought up to the layered gabbro section by ridge-parallel dikes (Boudier et al., 1996), the orientation of magmatic fabrics should roughly follow the flow direction as melt traversed the lower crust through fractures and sill intrusions (Korenaga and Kelemen, 1998; Boudier et al., 1996; Amri et al, 1996; Henstock et al, 1993; Jousselin et al 2015). Vertical features such as feeder dikes are unlikely to be mapped by a vertical hole, meaning that viewable magmatic structures related to flow direction will instead be located in the sills themselves. Alternatively, some fabrics observed from Hole GT1 have remarkably steeper dips that could be the result of steepening along faults (Kelemen et al, 2019). The resulting flow direction would be dynamic as fabrics could be spaced far apart or close together due to melt transfer occurring through hydrofractures and in-situ crust emplacement by on-axis sill intrusions (Korenaga and Kelemen, 1998). If expressed on a depth plot, the dip azimuth orientation of magmatic fabrics following the Sheeted Sills model would be varied and produce a scattered distribution of data points while very few dip azimuth measurements could share the same orientation.

The majority of orientation patterns observed from the depth plots in this study share that variability and are generally similar to the orientation of magmatic fabrics predicted by the Sheeted Sills model. This is best exemplified by the distribution of dip azimuth measurements between 150-200 mbs and past 300 mbs. However, several sections of the borehole exhibit a more orderly orientation pattern that contradicts the Sheeted Sills model. The data points between 200 and 250 mbs show a pattern of consistency with relatively little shift in orientation that instead resembles magmatic fabrics expected to form according to the Gabbro Glacier model (VanTongeren et al., 2015; Quick and Denlinger, 1993; MacLeod and Yaouancq, 2000; Morgan and Chen, 1993; Ben and Allard, 1989). Although the data points here are not all perfectly aligned toward a common dip azimuth, they still share a downward succession of dip azimuth values that remain very close to 200^{o}.

3.5 Potential for an Alternative Model

Although the dip azimuth orientations in this study appear to align more closely with the sheeted sills model as opposed to the gabbro glacier, neither hypothesis fully accounts for the non-systematic nature of measurements in Hole GT1 or the discrepancy between magmatic fabric and layering orientation. These measurements could instead represent local processes such as those described in the re-intrusion model from Bergantz (2015), which may provide an alternate explanation. In this model, the formation of magmatic fabrics depends on the rate of intrusion between incoming lower magmas and the crystal mush of an overlying reservoir. In the case of the Oman Ophiolite, sills in the lower crust would act as a reservoir while magmas from the Moho travel upwards within sills to begin intrusion. The ensuing melt interaction then promotes the appearance of a

"mixing bowl" between two newly formed fault surfaces (Bergantz, 2015) that give rise to localized shear bands and fabrics. Under the right conditions for intruding magma input and melt circulation in the mixing bowl, the resident melt and crystals will be propelled upwards and expelled through a central chimney and then begin slumping along the crystal mush-reservoir. Internal folding structures may form and be preserved through this process depending on if the magmatic flow has a low Reynold's number or remains viscous enough for the folds to develop slowly (Bergantz, 2000). These folds are defined by magmatic fabrics, and when drilled, would be seen as magmatic fabrics with variable orientation. Interactions between the melt and crystals in the chimney also create local increases in porosity through which new sources of melt can enter, leading to further re-intrusions provided the melt fraction is greater than 10% (Yoshinobu and Harper, 2004). Should there be enough available heat, the fault surfaces will transform into mylonites that develop crystal fabrics and localized shear zones commonly associated with mid-ocean ridges in slow-spreading crust (Bergantz, 2015), which were not observed here. If a similar process took place in the lower layered gabbros section of the Oman ophiolite, then it could explain some of the contrasts in dip azimuth orientation seen between the magmatic fabric and layering. Furthermore, the model implies that shared geochemical characteristics across melts may not always be the result of in-situ processes and can instead indicate a common site of melt generation since re-intrusion by more evolved magmas inevitably causes stratification or layering (Bergantz, 2000). The sheeted sills model could still apply here, however, because the mixing bowl is presumable located within a sill. This concurs with observations from the Josephine ophiolite in which the lower crust was interpreted to form by the repeating emplacement

of batches of magma characterized by a sill-like geometry and driven by subsidence of the upper and middle crust (Yoshinobu and Harper, 2004). The study also found this process to be enhanced by fast hydrothermal cooling at the ridge axis prior to intrusion. Recent geochemical evidence and models further suggest that the lower oceanic crust is an open system and that melts often traverse through the cumulate pile, requiring re-intrusion of new melts (e.g., Lissenberg and Dick, 2019) and therefore the possibility of generating a mixing bowl.

– CONCLUSIONS

Patterns of dip azimuth orientation observed in Hole GT1 support either the sheeted sills or a hybrid model of successive re-intrusions because of the non-systematic distribution and variability of magmatic fabrics and layering observed with depth, which implies that processes driving the formation and orientation of fabrics is local as opposed to large-scale regional processes. Although the gabbro glacier model does not match with the results of this study, subsidence may have still influenced a small percentage of the melt as evidenced by the downward succession of relatively consistent dip azimuth values between 200 and 250 mbs. Assuming that the right conditions for melt fraction, Reynold's number, and cooling rate were met, melt from the Moho traveled upwards in sills through a mixing bowl process before interacting with a crystal mush zone and produce layering as the melt subsided. Interactions between the melt and crystals promoted increased porosity and allowed for further re-intrusions as magmatic fabrics began to form. This may account for the discontinuous nature of MF and layering features while explaining how local processes likely influenced by the flow direction of melt in the magma chamber. Dip azimuth orientation is generally varied with depth throughout the borehole. However, there are several peaks in the number of MF measurements oriented NE-SW and layering measurments oriented N-S and NW-SE. These peaks in direction do not appear to correspond to any particular depth bin and are instead found throughout several intervals of depth. Further investigation is required to link together orientation of the upper and foliated gabbros to the lower layered gabbro section. The structural data provided in this thesis can therefore be of use to future studies on ophiolites and help further understanding of how lower oceanic crust forms on Earth.

REFERENCES

Amri, I., Benoit, M., and Ceuleneer, G., 1996, Tectonic setting for the genesis of oceanic plagiogranites:evidence from a paleo-spreading structure in the Oman ophiolite: Earth and Planetary Science Letters, v. 139, p. 177–194, doi:10.1016/0012 821X(95)00233-3.

Anonymous, 1972, Penrose field conference on ophiolites, Geotimes, v. 17, p. 24-25

Benn, K., and Allard, B., 1989, Preferred Mineral Orientations Related to Magmatic Flow in Ophiolite Layered Gabbros: Journal of Petrology, v. 30, p. 925–946, doi:10.1093/petrology/30.4.925.

Bergantz, George W., 2000 On the Dynamics of Magma Mixing by Reintrusion: Implications for Pluton Assembly Processes, Journal of Structural Geology 22, no. 9 (September 1, 2000): 1297–1309, https://doi.org/10.1016/S0191 8141(00)000535.

Bergantz, G. W., J. M. Schleicher, and A. Burgisser., Open-System Dynamics and Mixing in Magma Mushes, Nature Geoscience 8, no. 10 (October 1, 2015): 793 96. https://doi.org/10.1038/ngeo2534.

Boudier, F., Bouchez, J.L., Nicolas, A., Cannat, M., Ceuleneer, G., Misseri, M., and Montigny, R., 1985, Kinematics of oceanic thrusting in the Oman ophiolite: model of plate convergence: Earth and Planetary Science Letters, v. 75, p. 215 222, doi:10.1016/0012-821X(85)90103-7.

Boudier, F., and Nicolas, A., 1995, Nature of the Moho Transition Zone in the Oman Ophiolite: v. 36, 777 p., doi:10.1093/petrology/36.3.777.

Boudier, F., Nicolas, A., and Ildefonse, B., 1996, Magma chambers in the Oman ophiolite: fed from the top and the bottom: Earth and Planetary Science Letters, v. 144, p. 239–250, doi:10.1016/0012- 821X(96)00167-7.

Cheadle, M.J., and Gee, J.S., 2017, Quantitative Textural Insights into the Formation of Gabbro in Mafic Intrusions. *Elements* 2017;; 13 (6): 409–414. doi: https://doi.org/10.2138/gselements.13.6.409

Coleman, Robert G., 2014, The ophiolite concept evolves, *Element*, v.10.2, p. 82-84, http://www.elementsmagazine.org/archives/e10_2/e10_2_dep_perspective1.pdf

Cox, J., and Searle, M., 1999, Tectonic setting, origin, and obduction of the Oman ophiolite: GSA Bulletin, v. 111, p. 104–122, doi:10.1130/0016 7606(1999)111<0104:TSOAOO>2.3.CO;2.

Dilek, Y., Moores, E.M., Elthon, D., and Nicolas, A., 2000, Ophiolites and Oceanic Crust: New Insights from Field Studies and Ocean Drilling Program, v. 349, *Geological Society of America*, http://www.geosociety.org/documents/gsa/penconf/reports/98pcrpt4.html

Dilek, Y., and Furnes, H., 2014, Ophiolites and Their Origins: Elements, v. 10, p. 93 100, doi:10.2113/gselements.10.2.93.

Dunn, Robert A., Douglas R. Toomey, and Sean C. Solomon, 2000, Three-Dimensional Seismic Structure and Physical Properties of the Crust and Shallow Mantle beneath the East Pacific Rise at 9°30'N, Journal of Geophysical Research: Solid Earth 105, no. B10 (October 10, 2000): 23537–55. https://doi.org/10.1029/2000JB900210.

France, L., Ildefonse, B., and Koepke, J., 2009, Interactions between magma and

hydrothermal system in Oman ophiolite and in IODP Hole 1256D: Fossilization of a dynamic melt lens at fast spreading ridges: Geochemistry, Geophysics, Geosystems, v. 10, doi:10.1029/2009GC002652.

Fowler, C.M.R., 2012, 2 - The Earth: Core, mantle and crust, *in* Roberts, D.G. and Bally, A.W. eds., Regional Geology and Tectonics: Principles of Geologic Analysis, Amsterdam, Elsevier, p.1810.1023/A:1026772717865–39, doi:10.1016/B978-0444-53042-4.00001-7.

Gray, D.R., and Gregory, R.T., 2000, Implications of the structure of the Wadi Tayin metamorphic sole, the Ibra-Dasir block of the Samail ophiolite, and the Saih Hatat window for late stage extensional ophiolite emplacement, Oman: Marine Geophysical Researches, v. 21, p. 211–227.

Hacker, B.R., 1991, The role of deformation in the formation of metamorphic gradients: Ridge subduction beneath the Oman Ophiolite: Tectonics, v. 10, p. 455–473, doi:10.1029/90TC02779.

Hacker, B.R., Mosenfelder, J.L., and Gnos, E., 1996, Rapid emplacement of the Oman ophiolite: Thermal and geochronologic constraints: Tectonics, v. 15, p. 1230 1247, doi:10.1029/96TC01973.

Haggas, S. L., Brewer, T. S., Harvey, P. K., & Iturrino, G. I. (2001). Relocating and orientating cores by the integration of electrical and optical images: a case study from Ocean Drilling Program Hole 735B. *Journal of the Geological Society*, *158*(4), 615-623.

Haggas, S.L., Brewer, T.S., Harvey, P.K., and Macleod, C.J., 2005, Integration of electrical and optical images for structural analysis: a case study from ODP Hole

1105A: Geological Society, London, Special Publications, v. 240, p. 165, doi:10.1144/GSL.SP.2005.240.01.13.

Henstock, T.J., Woods, A.W., and White, R.S., 1993, The accretion of oceanic crust by episodic sill intrusion: Journal of Geophysical Research: Solid Earth, v. 98, p.4143–4161, doi:10.1029/92JB02661.

Jousselin, D., Morales, L.F.G., Nicolle, M., and Stephant, A., 2012, Gabbro layering induced by simple shear in the Oman ophiolite Moho transition zone: Earth and Planetary Science Letters, v. 331–332, p. 55–66, doi:10.1016/j.epsl.2012.02.022.

Kelemen, P.B., Koga, K., and Shimizu, N., 1997, Geochemistry of gabbro sills in the crust-mantle transition zone of the Oman ophiolite: implications for the origin of the oceanic lower crust: Earth and Planetary Science Letters, v. 146, p. 475 488, doi:10.1016/S0012-821X(96)00235-X.

Kelemen, P.B., Matter, J.M., Teagle, D.A.H., Coggon, J.A., and the Oman Drilling Project Science Team, 2020, Methods and explanatory notes, Proceedings of the Oman Drilling Project: College Station, TX (International Ocean Discovery Program. https:// doi.org/OmanDP.proc.2020.

Kelemen, P.B., Matter, J.M., Teagle, D.A.H., Coggon, J.A., and the Oman Drilling Project Science Team, 2020, Site GT1, Proceedings of the Oman Drilling Project: College Station, TX (International Ocean Discovery Program. https://doi.org/10.14379/OmanDP.proc.2020

Koepke, J., Müller, T., Bähre, L., Garbe-Schönberg, D., and Ildefonse, B., 2015, ICDP Oman Drilling Project: Site Summaries for Drill Sites GT1, GT2, and GT3,

ICDP Oman Drilling Project.

Korenaga, J., and Kelemen, P.B., 1997, Origin of gabbro sills in the Moho transition zone of the Oman ophiolite: Implications for magma transport in the oceanic lower crust: Journal of Geophysical Research: Solid Earth, v. 102, p. 27729–27749, doi:10.1029/97JB02604.

Korenaga, J., and Kelemen, P.B., 1998, Melt migration through the oceanic lower crust: a constraint from melt percolation modeling with finite solid diffusion: Earth and Planetary Science Letters, v. 156, p. 1–11, doi:10.1016/S0012 821X(98)00004-1.

Lissenberg, C. J., Sanfilippo, A., Dick, H. J. B., Marschall, H. R., & Urann, B. 2019, Emplacement and high-temperature evolution of gabbros of the 16.5°N oceanic core complexes (Mid-Atlantic Ridge): Insights into the compositional variability of the lower oceanic crust. Geochemistry, Geophysics, Geosystems, 20, 46– 66. https://doi.org/10.1029/2018GC007512.

MacLeod, C.., and Yaouancq, G., 2000, A fossil melt lens in the Oman ophiolite: Implications for magma chamber processes at fast spreading ridges: Earth and Planetary Science Letters, v. 176, p. 357–373, doi:10.1016/S0012 821X(00)00020-0.

Mock, D., Neave, D. A., Müller, S., Garbe-Schönberg, D., Namur, O., Ildefonse, B., & Koepke, J., 2020, Formation of igneous layering in the lower oceanic crust from the Samail ophiolite, Sultanate of Oman. *Journal of Geophysical Research: Solid Earth*, 126, e2020JB019573. https://doi.org/10.1029/2020JB019573

Morgan, J.P., and Chen, Y.J., 1993, The genesis of oceanic crust: Magma injection,

hydrothermal circulation, and crustal flow: Journal of Geophysical Research: Solid Earth, v. 98, p. 6283–6297, doi:10.1029/92JB02650.

Morris, A., Gee, J.S., Pressling, N., John, B.E., MacLeod, C.J., Grimes, C.B., and Searle, R.C., 2009, Footwall rotation in an oceanic core complex quantified using reoriented Integrated Ocean Drilling Program core samples: Earth and Planetary Science Letters, v. 287, p. 217–228, doi:10.1016/j.epsl.2009.08.007.

Morris, A., Meyer, M., Anderson, M.W., and MacLeod, C.J., 2019, What do variable magnetic fabrics in gabbros of the Oman ophiolite reveal about lower oceanic crustal magmatism at fast spreading ridges? Geology, v. 47, p. 275 278, doi:10.1130/G45442.1.

Mueller, T., 2015, A petrological and geochemical cross section of lower crust at the Wadi Gideah (Samail ophiolite):Implications for the crustal accretion at fast spreading mid-ocean ridges: Université de Montpellier, https://hal.archives ouvertes.fr/tel-01302675.

Nicolas, A., and Ildefonse, B., 1996, Flow mechanism and viscosity in basaltic magma chambers: Geophysical Research Letters, v. 23, p. 2013–2016, doi:10.1029/96GL02073.

Nicolas, A., and Boudier, F., 2015, Inside the magma chamber of a dying ridge segment in the Oman ophiolite: Terra Nova, v. 27, p. 69–76, doi:10.1111/ter.12130.

Nicolas, A., and Boudier, F., 1995, Mapping oceanic ridge segments in Oman ophiolite: v. 100, 6179 p., doi:10.1029/94JB01188.

Nicolas, A., and Boudier, F., 2015, Structural contribution from the Oman ophiolite to processes of crustal accretion at the East Pacific Rise: Terra Nova, v. 27, p. 77

96, doi:10.1111/ter.12137.

Nicolas, A., Boudier, F., Ildefonse, B., and Ball, E., 2000, Accretion of Oman and United Arab Emirates ophiolite – Discussion of a new structural map: v. 21, 147 p., doi:10.1023/A:1026769727917.

Nicolas, A., Boudier, F., and France, L., 2009, Subsidence in magma chamber and the development of magmatic foliation in Oman ophiolite gabbros: v. 284, 76 87 p., doi:10.1016/j.epsl.2009.04.012.

Nicolas, A., Boudier, F., and Ildefonse, B., 1996, Variable crustal thickness in the Oman ophiolite: Implication for oceanic crust: Journal of Geophysical Research: SolidEarth, v. 101, p. 17941– 17950, doi:10.1029/96JB00195.

Nicolas, A., Boudier, F., Ildefonse, B., and Ball, E., 2000, Accretion of Oman and United Arab Emirates ophiolite – Discussion of a new structural map: Marine Geophysical Researches, v. 21, p. 147–180, doi:10.1023/A:1026769727917.

Nicolas, A., Boudier, F., and Mainprice, D., 2015, Paragenesis of magma chamber internal wall discovered in Oman ophiolite gabbros: Terra Nova, v. 28, p. 91 100, doi:10.1111/ter.12194.

Nicolas, A., Reuber, I., and Benn, K., 1988, A new magma chamber model based on structural studies in the Oman ophiolite: The Ophiolites of Man, v. 151, p. 87 105, doi:10.1016/0040-1951(88)90242-9.

Park, Y., and Means, W.D., 1996, Direct observation of deformation processes in crystal mushes: Journal of Structural Geology, v. 18, p. 847–858, doi:10.1016/S0191 8141(96)80017-4

Paterson, S.R., Fowler, T.K., Schmidt, K.L., Yoshinobu, A.S., Yuan, E.S., and Miller,

R.B., 1998, Interpreting magmatic fabric patterns in plutons: Lithos, v. 44, p. 53–82, doi:10.1016/S0024-4937(98)00022-X.

Paterson, S.R., Ardill, K., Vernon, R., and Žák, J., 2019, A review of mesoscopic magmatic structures and their potential for evaluating the hypersolidus evolution of intrusive complexes: Back to the future, v. 125, p. 134–147, doi:10.1016/j.jsg.2018.04.022.

Quick, J., and Denlinger, R., 1993, Ductile deformation and the origin of layered gabbro in ophiolites: v. 981, doi:10.1029/93JB00698.

Rioux, M., Garber, J., Bauer, A., Bowring, S., Searle, M., Kelemen, P., and Hacker, B., 2016, Synchronous formation of the metamorphic sole and igneous crust of the Semail ophiolite: New constraints on the tectonic evolution during ophiolite formation from high-precision U–Pb zircon geochronology: Earth and Planetary Science Letters, v. 451, p. 185–195, doi:10.1016/j.epsl.2016.06.051.

Tominaga, M., 2013, "Imaging" the cross section of oceanic lithosphere: The development and future of electrical microresistivity logging through scientific ocean drilling: Tectonophysics, v. 608, p. 84–96, doi:10.1016/j.tecto.2013.06.018.

VanTongeren, J.A., Hirth, G., and Kelemen, P.B., 2015, Constraints on the accretion of the gabbroic lower oceanic crust from plagioclase lattice preferred orientation in the Samail ophiolite: Earth and Planetary Science Letters, v. 427, p. 249–261, doi:10.1016/j.epsl.2015.07.001.

Yoshinobu, A.S., and Harper, G.D., 2004, Hypersolidus deformation in the lower crust of the Josephine ophiolite: evidence for kinematic decoupling between the upper and

lower oceanic crust, Journal of Structural Geology, v. 26, p. 163–175, doi:10.1016/S0191-8141(03)00078-6.

.